FRONTS AND VARIABILITY IN THE COASTAL OCEAN

by

YUNTAO WANG

(Under the Direction of Renato M. Castelao)

ABSTRACT

The coastal ocean is characterized by strong gradients in water properties, which influences circulation and ocean-atmosphere interactions. Fronts and variability in the coastal ocean are studied using a combination of satellite observations and numerical model simulations. Satellite sea surface temperature (SST) and wind observations are used to describe the seasonal evolution of temperature fronts and their relation to wind forcing in Eastern Boundary Current Systems (EBCS). Front activity is closely related to seasonal variability in wind forcing and to the presence of topographic perturbations such as capes. Investigation of the coupling between SST gradients and wind variables in the global coastal ocean reveals that regions with strong front activity are generally also characterized by strong ocean-atmosphere interaction. Mid-latitude regions, especially in EBCS, are characterized by enhanced ocean-atmosphere coupling during local summer. In several low-latitude regions, however, the coupling is stronger during winter. Although the coupling between SST gradients and wind stress divergence is stronger at seasonal scales, intraseasonal variability associated with mesoscale eddies is stronger for the coupling between SST gradients and wind stress curl. Coastal regions can also present strong salinity gradients, especially near river mouths. The circulation at a complex estuarine system off Georgia is investigated using a numerical model. The estuary includes three major sounds that are connected by a network of channels, creeks and intertidal areas. Spatial and temporal variability in residence time and connectivity between the sounds are influenced primarily by the Altamaha River discharge, by seasonally-varying winds, and by tidal forcing.

INDEX WORDS: Coastal ocean, Front, Ocean-atmosphere interaction, Residence time, Connectivity, Estuary of Georgia

FRONTS AND VARIABILITY IN THE COASTAL OCEAN

by

YUNTAO WANG

Ph. D., The University of Georgia, 2016

A Dissertation Submitted to the Graduate Faculty of

The University of Georgia in Partial Fulfillment of

The Requirements for the Degree

DOCTOR OF PHILOSOPHY

ATHENS, GEORGIA

2016

FRONTS AND VARIABILITY IN THE COASTAL OCEAN

by

YUNTAO WANG

Major Professor: Renato M. Castelao
Committee: Daniela Di Iorio
Adrian Burd
Brock Woodson
Catherine Edwards

Electronic Version Approved:

Suzanne Barbour
Dean of the Graduate School
The University of Georgia
May 2016

ACKNOWLEDGEMENTS

I would like to thank my advisor, Renato Castelao, for his tremendous help and guide throughout my entire PhD study. The dissertation would not be possible without his patient modification and direction. I would like to thank all of other committee members. They are Daniela Di Iorio, Adrian Burd, Brock Woodson and Catherine Edwards. They are very approachable and patient. I really appreciate their help and kindness, which are greatly important for encouraging and guiding me to complete my degree.

I feel great thankful for my family and friends. Especially my parents: Youliang Wang and Zhiping Wang; my grandparents: Songpo Wang and Shuying Li; my friends: Chen Shen, Qian Liu, Ye Wang, Jing Chen, Yuan Zhuang, De Si, Yeping Yuan, Linquan Mu, Jun Meng, Meng Fang, Ye Shen, Leidong Mao, Fang Cao, Qianhui Qin, , Montinel Perez, Ding He; faculty and staffs: Youngchen Wang, Wei-Jun Cai, Guirong Han, James T. Hollibaugh, Patricia Medeiros, Bill Miller, Christof Meile, Mingyi Sun, Chuanlun Zhang, Jennifer Pressey, Jackie Fortson, Catherine Mills, Kyleigh Weaver, Kristin Miller; colleagues: Hai Pan, Guangyu Xu, Jared McKnight, Leanne Powers, David Miklesh, Trevor Richards, Shiyu Wang, Haiwei Luo, Bradley Tolar, Hao Luo, Jonathon Taylor; and my future colleagues: Mark Risse, Jane DiCosimo, Lee Benaka, Mona Behl,

Cheryl Summers, Angela Llewallyn, Jihong Dai among others. They are very supportive and understandable with my graduation and future plan.

I gratefully acknowledge support by NASA (Ocean Vector Winds Science Team grant NNX14AM70G and grant NNX10AE92G). It would not be possible for me to have the opportunity to come to America to pursue my degree.

I also gratefully acknowledge support by the National Science Foundation (OCE-1237140) as part of the Georgia Coastal Ecosystems Long Term Ecological Research project. Institutional Grant (NA100AR4170098) from the Georgia Sea Grant College Program in the National Sea Grant Office, National Oceanic and Atmospheric Administration (NOAA), U.S. Department of Commerce and grant award NA11NOS4190113 from the Georgia Department of Natural Resources (DNR) in the Office of Ocean and Coastal Resource Management (OCRM), NOAA.

TABLE OF CONETENTS

LIST OF FIGURES

LIST OF TABLE

Table Page

CHAPTER 1

INTRODUCTION AND LITERATURE REVIEW

Sea surface temperature (SST) fronts are ubiquitous features in the ocean, separating the distribution of different water masses. Investigations regarding the distribution and variability of SST fronts have been pursued for more than half a century [Cromwell and Reid, 1956]. Fronts play an important role in oceanic circulation, analogous to their counterparts in the atmospheric circulation [Garvine and Monk, 1974].

Fronts are many times associated with vigorous ocean currents, which can alter and influence patterns of biological distributions [Owen, 1981]. Frontal regions are generally characterized by convergence [Bowman and Iverson, 1978], with abundant supply of nutrients [Ryan et al., 1999] and resources for fishery [Uda, 1953]. Indeed, high chlorophyll concentration and enriched inorganic nutrients are often observed in the vicinity of SST fronts [Savidge, 1976]. With time, free floating biota are drawn into frontal zones due to the prevailing convergence flow [Bowman and Iverson, 1978], which can lead to a fully developed food chain as fish at higher trophic levels are likewise attracted to these regions in search of food.

Theoretical analysis, numerical model simulations and satellite observations have been used to advance our understanding of the structure of SST fronts and of frontogenetic processes in the ocean [Collins, 1964; Fedorov, 1983]. The understanding of the distribution of SST fronts was especially advanced with the development of satellite observations [Cayula and Cornillon, 1992; Ullman and Cornillon, 1999; Ullman and Cornillon, 2000], which allows for large scale features and persistent SST fronts to be detected in high resolution at a global scale [Legeckis, 1978; Belkin et al., 2009]. High SST frontal activity has been observed in many oceanic systems, including over continental shelves [e.g., Yoder et al., 2002], around the shelfbreak [e.g., Belkin and O'Reilly, 2009] and in upwelling regions [e.g., Castelao and Wang, 2014].

The main goal of this dissertation is to provide a better understanding of the distribution of fronts in coastal systems. Although the main focus is on the distribution of SST fronts over the shelf, a look into salinity fronts and variability in an estuary characterized by complex geometry is also taken. A combination of observations and numerical modeling results are used in the investigation. A general introduction about SST fronts and their importance are presented in Chapter 2.

In chapter 3, infrared satellite observations of SST and scaterometer observations of winds are used in combination to describe the seasonal evolution of fronts in Eastern Boundary Currents. Eastern Boundary Current Systems are characterized by high biological production and nutrient levels [Chavez and Messié, 2009]. This is at least due to wind driving offshore transport in the surface layer [Ekman, 1905], which induces upwelling of cold, nutrient-rich water from depth to the surface. The presence of cold, upwelled water near the coast and of warm waters offshore often leads to the establishment of SST fronts [Kostianoy and Lutjeharms, 1999]. Monthly frontal probabilities are calculated and then used to describe temporal and spatial patterns of variability in front activity, as well as to relate those patterns to wind forcing and geometric characteristics. Additional analyses are presented in Appendix A.

In addition to strongly influencing ocean processes, fronts can also influence atmospheric processes as well, playing an important role in mescoscale air-sea interactions [e.g., Chelton et al., 2001; 2004; 2007]. Enhanced vertical mixing over the warmer side of the front deepens the marine-atmospheric boundary layer, drawing momentum from the upper boundary layer down to the sea surface and increasing winds aloft. Over the cold side of the front, by contrast, surface wind decreases in association with increased stability of the atmospheric boundary layer [Chelton and Xie, 2010]. As a result of this coupling between oceanic and atmospheric processes, when winds blow along a SST front higher winds over the warm side of the front and weaker winds over the cold side of the front generate wind stress curl. If the winds blow across a SST front, wind stress divergence is generated [Chelton et al., 2001]. Since wind stress curl anomalies drive Ekman pumping [e.g., Pickett and Paduan, 2003], they can be associated with significant upwelling or downwelling, leading to modifications in the SST distribution itself [O’Neill et al., 2003]. As a result, a linear relation has been found between anomalies of the crosswind component of SST gradients and wind stress curl, and between anomalies of the downwind component of SST gradients and wind stress divergence [Chelton et al., 2001].

Mesoscale ocean-atmosphere interaction has been widely observed, both in the open ocean [O'Neill et al., 2003; Chelton et al., 2004; O'Neill et al., 2005; 2010; among others] and in coastal regions [Chelton et al., 2007; Castelao, 2012; Desbiolles et al., 2014]. Despite that, a systematical characterization of the spatial and temporal variability in the strength of the coupling in coastal regions has not been achieved on a global scale. This makes it difficult to compare the strength of the interaction between different regions, since some of the variability observed between the studies is likely a result of slightly different methodologies used. Thus, we use a consistent method and data sets to systematically quantify the strength of the interactions in coastal regions throughout the globe in chapter 4.

Not all fronts in the ocean are due to temperature differences. In estuarine regions, for example, strong gradients in salinity are observed, often strongly influenced by the local geometry. In the Georgia coast, for example, the local topography is very complex. Three major estuaries, the Altamaha River and Doboy and Sapelo Sounds, are connected by a network of channels, creeks and intertidal areas. Although much has been learned over the last decades about estuaries with a single channel and a single connection to the sea (Geyer, 2010; Geyer and MacCready, 2014), comparatively fewer studies have focused on estuaries with multiple inlets. Recent studies have shown that channels connecting adjacent estuaries play a crucial role on the overall connectivity in the system [Zhao et al., 2010; Di Iorio and Castelao, 2013]. Estuaries off Georgia are also strongly influenced by semidiurnal tides [Menzel, 1993], freshwater input from the Altamaha

River [Sheldon and Burd, 2014], and winds with strong seasonal patterns [Blanton et al., 2003]. In chapter 5, a high-resolution coastal ocean model is used to investigate salinity variability and water exchange in the estuaries around Sapelo Island off Georgia. A Lagrangian particle tracking scheme is used to quantify residence time and to identify connectivity and transport pathways in the system.

CHAPTER 2

OCEAN FRONTS AND OCEAN-ATMOSPHERE INTERACTIONS

Water temperature is one of the main parameters controlling ocean circulation. As such, it received a great deal of attention from the oceanography community over the last century. In particular, variations in water temperature at the surface of the ocean, referred to as sea surface temperature (SST), have been shown to dramatically influence oceanographic and atmospheric processes.

Because of variations in solar radiation received from the sun, there is a general tendency for SST to decrease with increasing latitude, from about 30°C near the equator to near 0°C in polar regions. Simply dividing this SST difference by the distance between the equator and the poles results in an average SST gradient in the ocean of 0.003-0.004°C/km. Much strong SST gradients are observed in many regions of the ocean, however. Those regions characterized by strong SST gradients are referred to as fronts by the scientific community. There has been strong interest in investigating regions with strong SST gradients for many decades [*Uda*, 1938], in part because abundant fish and whales are found in those regions [*Uda*, 1953].

SST fronts strongly influence physical, biological, and chemical processes in the ocean. For example, fronts are regions generally characterized by convergent flow at the surface, which can lead to the accumulation of free-floating biota, influencing many biological processes [*Bowman and Iverson*, 1978]. A fully developed food chain can be established afterward, as fish and other higher trophic levels are attracted to these regions in search of food.

Most fronts in the surface layer of the ocean result primarily from differential horizontal and/or vertical temperature advection [*Roden and Paskausky*, 1978]. They can be generated by a variety of processes, including strong currents [e.g., *Kelly and Dong*, 2004], wave-like instabilities [e.g., *Breaker and Mooers*, 1986], convergence [e.g., *Bakun and Nelson*, 1977], riverine inputs [e.g., *Morgan et al.,* 2005] and interactions of the flow with topography [*Holladay and O'Brien,* 1975]. In coastal regions, one of the primary processes driving frontogenesis (i.e., the generation of fronts) is coastal upwelling. Coastal upwelling is a process in which, because of the rotation of the Earth, surface winds blowing along the coast can drive the offshore transport of water in the surface layer of the ocean. This is typical of summer conditions along the eastern boundaries of the ocean (i.e., in Eastern Boundary Current Systems; EBCS). The movement of water in a direction perpendicular to the wind forcing is called Ekman transport [*Ekman*, 1905], and it is fundamentally important to coastal ecosystems in EBCS. This is because surface water transported offshore is replaced by waters from below. The rising water brings bottom water, which is rich in nutrients, to the euphotic zone [*Sverdrup et al.,* 1942], which is reflected in the distribution of phytoplankton [*Sverdrup and Allen,* 1939]. As a result, upwelling regions are generally nutrient-rich, sustaining a highly productive food web [*Walsh et al.,* 1977]. Since the bottom water is also cold, a region of sharp gradients in SST (i.e., a front) between the warm offshore and cold inshore water is often established.

Characterizing SST front distribution and variability using in situ observations is difficult, because these are generally features extending for hundreds of kilometers and that vary on short time scales. As such, their characterization is best done with satellite observations [*Legckis*, 1978]. Different algorithms have been developed to detect SST fronts based on satellite data [*e.g., Canny*, 1986; *Cayula and Cornillon*, 1992], allowing for investigation of their distribution over large spatial and temporal scales [*Ullman and Cornillon*, 1999]. The investigation of SST front variability in EBCS is one of the major focuses of this dissertation (see Chapter 3).

In addition of strongly influencing oceanic processes [*e.g., Polovina et al*., 2000; *Polovina et al.,* 2001; *Chai et al.,* 2003; *Bograd et al.,* 2004], SST fronts can also influence atmospheric processes. It has long been recognized that wind speeds over cold water are generally weaker than over warm water at the Gulf Stream [*Sweet et al.,* 1981]. Following that original study, observations consistently revealed similar patterns around the globe because of processes occurring in the marine-atmosphere boundary layer [*Hsu et al.,* 1985; *Warner et al.,* 1990; *Jury et al.,* 1994; *Kwon et al.,* 1998; *Vihma et al.,* 1998; *Rouault et al.,* 2000]. Surface wind generally increases over warm water in association with decreased stability through enhanced vertical mixing that deepens the atmospheric boundary layer and draws momentum from the upper boundary layer down to the sea surface [*Chelton and Xie*, 2010]. Over cold water, by contrast, surface wind decreases in association with increased stability that decouples the surface winds from the stronger winds aloft. As a result, when winds blow along a SST front, higher winds are found over the warm side of the front and weaker winds are found over the cold side of the front. The crosswind shear in wind stress, or the non-uniform distribution in wind speed in the direction perpendicular to the wind direction itself, is called wind stress curl. When winds blow across a SST front, downwind wind speed will increase as the wind blows from the cold to the warm side of the front, or decrease if the wind blows from the warm to the cold side of the front. The change in wind stress magnitude in the same direction that the wind is blowing is called wind stress divergence.

With the developed of high quality satellite observations of wind, the impact of SST fronts on wind stress could be observed in high resolution at large scales. The seminal work by *Chelton et al.* [2001] showed that wind stress curl and divergence anomalies vary linearly with the crosswind and downwind components of the SST gradient, respectively. This coupling between SST and winds has been widely observed, both in the open ocean [*O'Neill et al.,* 2003; *Chelton et al.,* 2004*; O'Neill et al.,* 2005; 2010; 2012 among others] and in coastal regions [*Chelton et al.,* 2007; *Castelao,* 2012; *Desbiolles et al.,* 2014].

The influence of SST on wind stress is clearer in regions with strong SST gradients [*Haack et al.,* 2008]. The influence is often quantified by a coupling coefficient, which is defined as the slope of the regression between crosswind SST gradients and wind stress curl and between downwind SST gradients and wind stress divergence [*e.g., O'Neill et al.,* 2010]. *O'Neill et al.* [2005] showed that the strength of the wind response is associated with variations in the potential temperature lapse rate. *Spall* [2007] noticed that the response is quadratically dependent on the large scale wind speed, so that stronger winds result is even stronger responses. Seasonal variability in front activity [*e.g., Castelao and Wang,* 2014] can also lead to seasonal variations in the strength of the response [*Chelton et al.,* 2007]. As SST fronts in the ocean influence the winds aloft, they can in turn be influenced by the now-modified winds, establishing a complex nonlinear system in which the ocean and atmosphere systems are fully coupled: variations in water temperature influences the winds, which in turn modify ocean circulation and the distribution of water temperatures, which will further modify the winds, and so on. Quantifying spatial and temporal variability in the intensity of the coupling between SST gradients and winds in the coastal ocean on a global scale was a major focus of this dissertation (see Chapter 4).

In summary, SST fronts are ubiquitous features in the global ocean, strongly influencing not only physical, biological and chemical oceanographic processes, but also atmospheric processes as well. Because of high spatial and temporal variability, satellite observations generally provide the best opportunity to investigate this complex, oceanic-atmospheric coupled system.

CHAPTER 3

SEASONAL VARIABILITY OF ALONGSHORE WINDS AND SEA SURFACE TEMPERATURE FRONTS IN EASTERN BOUNDARY CURRENT SYSTEMS

Wang Y., R. M. Castelao and Y. Yuan. 2015. *J. Geophys. Res. 120*(3), 2385-2400
Reprinted here with permission of the publiser

3.1 Abstract

Seven years of satellite observations (2003 - 2009) are used to describe the variability in sea surface temperature (SST) fronts and in the alongshore component of ocean winds, and to investigate their relations in four Eastern Boundary Current Systems (EBCS). The general patterns of SST frontal activity are remarkably similar in all EBCS, with high frontal probabilities along the coast decreasing with distance from the coastline. Results from empirical orthogonal function decompositions reveal that the seasonal evolution of SST fronts and wind stress are significantly correlated, with intensified upwelling favorable winds associated with an increase in frontal probabilities. An offshore migration of the region of high frontal activity is observed during the period of upwelling favorable alongshore wind stress in EBCS. In all regions, the seasonal variability of frontal activity and wind stress is stronger at mid than at low latitudes. The width of the region of high frontal activity is relatively broader in the California and Benguela Current Systems, and narrower in the Canary and Humboldt Current Systems. The width of the band of high frontal activity may be influenced by multiple factors, including wind forcing, flow topography interactions, and mesoscale dynamics. While seasonal variability in frontal activity in the California Current System acts to reinforce or weaken the average pattern, they are substantially different in the Canary Current System, where there is little overlap in the areas characterized by persistent and seasonally varying front activity.

3.2 Introduction

There have been many studies investigating Eastern Boundary Current Systems (EBCS) in the past few decades [e.g., *Sverdrup et al.,* 1942], covering their physical, geological, biological and chemical characteristics [*Ryther,* 1969*; Barber and Smith,* 1981; among others]. If large enough spatial scales are considered, the coastlines in EBCS are generally aligned in the meridional direction. In that case, prevailing equatorward wind forcing (especially during local summer) results in offshore Ekman transport at the surface [*Ekman,* 1905], inducing upwelling and bringing cold, nutrient-rich water from depth to the surface near the coast. A sea surface temperature (SST) front is often established separating the cold, upwelled water near the coast from warm, offshore waters [e.g., *Kostianoy and Lutjeharms*, 1999]. Upwelling fronts are dynamically important, because a strong alongshore coastal upwelling jet is generally formed in geostrophic balance with the upwelled isopycnals [*Huyer,* 1983]. A poleward undercurrent is often observed beneath the upwelling jet within a few tens of kilometers from the coast [*McCreary*, 1981]. Fronts have also been shown to play an important role on the regional atmospheric circulation in EBCS. Recent studies have revealed strong interactions between SST and wind stress [e.g., *Chelton et al.,* 2004*; Spall,* 2007*; O'Neill et al.,* 2010], resulting in strong variability in the wind stress curl field in EBCS [*Chelton et al.,* 2007]. Wind stress curl can then feedback on the circulation, driving offshore upwelling via Ekman pumping over large areas [*Pickett and Paduan,* 2003]. Fronts are also important for biological processes. Fronts are generally characterized by convergent flow at the surface [*Bowman and Iverson,* 1978], which leads to the accumulation of free floating biota. With time, a fully developed food chain can be established, as higher trophic levels are attracted to these regions in search of food. A recent comparison between the different EBCS is given by *Chavez and Messié* [2009].

The availability of high-resolution satellite observations of SST allows for the detection of ocean fronts over large areas. *Legeckis* [1978] used environmental satellite data to depict SST frontal distribution globally. He also discussed several physical processes driving the formation and maintenance of SST fronts, including flow intensifications, interactions of the circulation with bottom topography, wind- induced upwelling, among others. SST fronts in EBCS have received a great deal of attention over the last few years [e.g., *Meunier et al.,* 2012*; Nieto et al.,* 2012*; Santos et al.,* 2012*; Vazquez-Cuervo et al.,* 2013]. The distribution of SST fronts in the California Current System has been shown to be characterized by large seasonal variability [*Castelao et al.,* 2006], being influenced by upwelling, mesoscale dynamics [*Kahru et al.,* 2012] and interactions of the flow with topography [*Castelao et al.,* 2005]. Mesoscale dynamics and eddy activity also seem to influence the distribution of SST gradients off the Peruvian Coast [*Vazquez-Cuervo et al.,* 2013]. Strong seasonal variability in front distribution is observed in the Canary Current System, with intense fronts being observed near major capes [*Nieto et al.,* 2012]. Fronts have also been shown to play an important role constraining water masses, with high primary productivity being mostly limited to inshore of fronts in the southern Benguela region [*Hutchings et al.,* 2009].

More recently, *Castelao and Wang* [2014] investigated the variability in SST frontal distribution in the California Current System, and quantified its relation to wind forcing. They found that the seasonal development of SST fronts in the northern and southern sectors of the California Current System is remarkably distinct, but that in both regions it is tightly coupled to the seasonal variability in coastal alongshore winds. In particular, anomalies in the intensity of frontal activity are strongly coupled to anomalies in the intensity of upwelling favorable winds. They also showed that the region of high frontal activity near the coast in the California Current System widens from spring to fall, and that how fast the region widens is related to upwelling favorable winds. Here, we expand their analysis and compare the spatial and temporal characteristics of SST front distribution in the four major EBCS, as well as their relation to wind forcing.

3.3 Data and methods

Sea surface temperature (SST) data are obtained by the Moderate Resolution Imaging Spectroradiometer (MODIS). Observations are available since August 2002, and measurements within 5 km from land or from pixels flagged as clouds are discarded to avoid contamination. SST fronts are identified using an edge-detection algorithm [*Canny,* 1986] following *Castelao et al.* [2005, 2006] and *Castelao and Wang* [2014]. Briefly, we first compute the SST gradient vector for each SST map. The thresholding in the edge-detection algorithm is done with hysteresis. The algorithm first looks for pixels with gradient magnitude larger than a threshold T_1. These pixels are flagged as frontal pixels.

The algorithm then tracks along a front crest flagging individual pixels as fronts until the gradient magnitude falls below a smaller threshold T_2. This helps to ensure that noisy edges are not broken up into multiple edge fragments. Thresholds employed are 2.8°C and 1.4°C per 100 km, following *Castelao and Wang* [2014]. Comparison of fronts detected with gradient magnitude maps show that the chosen threshold values allow for capturing most of the main fronts in the different EBCS. Monthly frontal probabilities are computed at each pixel as the ratio between the number of times the pixel qualifies as a front and the number of times that the pixel is cloud free during that month [e.g., *Ullman and Cornillon,* 1999; *Mavor and Bisagni,* 2001].

Wind data from July 1999 to November 2009 were obtained from the SeaWinds Scatterometer onboard NASA's Quick Scatterometer (QuikSCAT) satellite. A detailed description of the measurements is given by *Chelton and Freilich* [*2005*]. The QuikSCAT spatial resolution is approximately 25 km, and measurements within 30 km from the coast are contaminated by radar backscatter from land in the antenna side lobes. The alongshore component of the wind stress was determined as the dot product between wind measurements within 150 km from the coast and a unit vector tangent to the local coastline (obtained by fitting a straight line through a 100 km section of a coastline centered at the coastal point).

For empirical orthogonal function (EOF) decompositions, we focus on the period from 2003 to 2009, when both observations of wind and SST are available simultaneously. Since SST frontal activity generally decreases with distance from shore [e.g., *Castelao et al.,* 2006], only observations within a zonal distance of approximately 600 km from the coast are used in the analyses. Monthly averages of the alongshore component of the wind stress averaged within 150 km from the coast were first computed to facilitate comparisons with the monthly frontal probability data. The temporal mean of monthly SST frontal probability and alongshore wind stress at each location was determined and then removed from the corresponding time series before EOF decompositions. To reduce the possibility of biases in frontal distribution due to cloud contamination, only pixels where observations are available for at least 20% of the time in each month are used in the frontal probability EOF decomposition. In all cases, the amplitude time series of each EOF for each variable is normalized by its respective standard deviation. All EOFs shown here can be statistically distinguished (95% confidence level) from the results of EOF analyses of spatially and temporally uncorrelated random processes [*Overland and Preisendorfer,* 1982]. Although each EOF explains a relatively small fraction of the total variance (Table 3.1), they explain a larger fraction of the local variance [*Chelton and Davis*, 1982] in areas where the respective EOFs are high (~30% for EOF 1, ~10% for EOF 2). As described by *Castelao and Wang* [2014], this difference occurs because SST frontal probabilities are inherently noisy. As such, in the offshore areas where the signal is small and the measurement is dominated by noise, several EOF modes are needed to reconstruct the mostly incoherent field. As a result, the EOFs, although capturing a significant fraction of the local variance in the areas within a few hundred kilometers from the coast, explain a relatively small fraction of the total variance. Repeated EOF decompositions (not shown) using simulated data with similar spatial and temporal characteristics of the SST frontal probabilities shown here, but in which random noise is progressively increased, confirm this interpretation. As the background noise level increases in the simulations, the fraction of the total variance explained by the EOFs decreases. Despite that, the EOF decomposition is still able to capture the dominant patterns of variability in the simulated data, suggesting that the EOFs shown here are statistically reliable.

3.4 Results

3.4.1 Average frontal probability and SST gradient distribution

A 7 year average of satellite observations reveals high frontal probabilities (Figure 3.1a-3.1d) and strong SST gradients (Figure 3.1e-3.1h) in all Eastern Boundary Current Systems (EBCS; we will refer to the regions shown in Figure 3.1 as California, Canary, Humboldt and Benguela Current Systems). The spatial distributions of fronts and SST gradients share similar patterns in the different regions. The dominant pattern is that most fronts are observed along the coast, resulting in high frontal probabilities that generally decrease with distance from the coastline. In the California Current System, relative high mean frontal probabilities are observed extending for about 240 km from shore (Table 3.1). The widest region of high frontal activity is found between Cape Blanco and Point Arena (Figure 3.1). High mean frontal probabilities are also found along the coast in the Benguela Current System extending for about 210 km offshore. In the Humboldt Current

System, high frontal probabilities are observed in a comparatively narrower band, generally less than 165 km wide. The widest area of frontal probability in this region is observed to the north of Punta Lavapie near Concepcion. The distribution of frontal probabilities is similar in the Canary Current System, where a narrow band (115km) with high frontal probabilities is observed throughout the coast, except between 20°N and 25°N where the area of high frontal activity is about 200 km wide. Consistent with the distribution of average frontal probabilities, highest SST gradients are also found near the coast, gradually decreasing offshore (Figure 3.1e-3.1h). The area with strong SST gradients is wider in the California and Benguela Current Systems than in the Canary and Humboldt Current Systems (Table 3.1).

Despite those similar general characteristics, strong meridional variability in front distributions is observed in each system. In the California Current System, for example, a localized increase in frontal probabilities is observed near the Columbia River mouth (Figure 3.1a). High mean frontal probabilities are observed at and inshore of the 200 m isobath between Heceta Bank and Cape Blanco, but high frontal probabilities extend far offshore of the 2000 m isobath to the south of the Cape. This is especially true off Cape Mendocino and off Point Arena, where the width of the band with high frontal probabilities is largest. South of Point Arena, high frontal probabilities and strong SST gradients are only observed near the coast.

The Canary Current System is characterized by very complex topography, with large changes in the orientation of the coastline and the presence of multiple capes and offshore islands. High mean frontal activity is generally limited to inshore of the 2000 m isobath (Figure 3.1b), peaking between Cap-Vert (15°N) and Cape Bojador (25°N), an area of persistent front activity [*Nykjær and Van Camp*, 1994]. Frontal probabilities are especially high around Cape Blanc (21°N), an area characterized by high eddy activity and formation of upwelling filaments [*Meunier et al.*, 2012]. The local enhancements in frontal activity off Cape Bojador and Cape Ghir are possibly associated with strong Ekman transport in those areas due to wind acceleration by orographic effects [*Lathuilière et al.*, 2008]. Between Cape Beddouza and the Strait of Gibraltar, upwelling [*Arístegui et al.,* 2009; *Nieto et al.*, 2012] and average frontal probabilities are relatively reduced. Off the coast of Portugal and Spain at the Iberian Peninsula, high frontal activity and strong SST gradients are generally observed near major capes and submarine ridges (e.g., off Cape Vincent, Cape Roca and Cape Finisterre). These areas are often associated with the formation of upwelling filaments [*Hayneset al.*, 1993].

In the Humboldt Current System, high mean frontal probabilities are generally limited to the region within 165 km from the coast (Figure 3.1c and Table 3.1). The entire coast can be subdivided into three regions in terms of front distribution: a northern sector between Chiclayo and Cape Paracas (from 5°S to 15°S), a central sector between Cape Paracas and Coquimbo (15°S to 30°S), and a southern sector extending to the south of Coquimbo (30°S to 40°S). Average frontal probabilities are high in a narrow band near the coast in the northern sector, decreasing progressively with distance from the coast. This is especially true between Chiclayo and Lima. Slightly higher values are observed near Cape Paracas. The central sector is characterized by a narrow band with relative high frontal probabilities and strong SST gradients along the coast. Values decrease very sharply offshore, especially off Arica. We note that this area is characterized by relatively high cloud coverage leading to a relatively smaller number of available observations, which may introduce a bias in the analysis. Relative high frontal probabilities in the southern sector cover the entire shelf up to 200 km offshore. Frontal activity is enhanced near Coquimbo and Concepcion, downstream of Punta Lavapie.

Three large areas with high frontal probabilities can be identified in the Benguela Current System (Figure 3.1d; around Cape Frio at 18°S, Luderitz at 27°S and Cape Columbine at 33°S), coinciding with major upwelling centers [*Hutchings et al.*, 2009]. The area off Cape Frio, which is located just south of the Angola-Benguela Front Zone [*Veitch et al.,* 2006; *Hutchings et al.*, 2009], is characterized by persistent upwelling [*Chavez and Messié*, 2009]. The Angola-Benguela Frontal Zone, located at the confluence of the Angola and the Benguela Currents [*Rouault et al.,* 2007], has been shown to remain a distinct feature throughout the year for up to a distance of 250 km from the coast, although its vestiges can sometimes be identified as far as 700 km offshore [*Veitch et al.,* 2006]. Off Luderitz, high frontal probabilities are observed in a band extending offshore toward the northwest. High frontal activity is also found near the coast extending southward of Luderitz toward Cape Columbine (33°S) in an area characterized by seasonal upwelling [*Chavez and Messié*, 2009]. Off Orange River, the band with high SST gradients near the coast is particularly narrow, being approximately

100 km wide. The same is true for the area farther north off Walvis Bay.

3.4.2 Dominant modes of variability in frontal activity

The dominant patterns of frontal activity variability, as identified by empirical orthogonal function (EOF) decompositions, are shown in Figure 3.2. The amplitude time series of the respective EOFs are shown in Figure 3.3. A general feature of the first EOF in all EBCS is that higher variability is found near the coast, decreasing offshore. There is substantial variability in the width and in the alongshore extent of the areas of high variability near the coast, however. In all cases, the amplitude time series reveal that the EOFs capture variability at seasonal scales, so that frontal activity is generally enhanced from late spring to early fall and reduced during winter in each hemisphere. *Castelao and Wang* [2014] recently used EOF analysis to describe seasonal variability of frontal activity in the California Current System. They found that the largest seasonal variability occurs between Heceta Bank and Cape Mendocino (Figure 3.2a), where frontal activity extends for hundreds of kilometers from the coast (Table 3.1) peaking in fall (Figure 3.3a and 3.3b). The region to the south of Cape Mendocino is also characterized by enhanced high frontal activity during spring (Figure 3.3e and 3.3f) in a much narrower band close to the coast (EOF2, Figure 3.2e). A detailed description of analysis for the California Current System can be found in *Castelao and Wang* [2014].

The Canary Current System is perhaps the EBCS with the strongest variability, both spatially and temporally at seasonal scales [*Carr and Kearns*, 2003]. The first EOF of frontal probability captures seasonal variability in shelf and near coastal areas (Figure 3.2b). Strong seasonal variability is observed off the Iberian Peninsula and around Cape Ghir and Cape Juby. The region between Cape Juby and just north of Cape Blanc, although presenting strong and persistent upwelling [*Lathuilière et al.*, 2008] and large average frontal probabilities (Figure 3.1b), is characterized by somewhat reduced seasonal variability compared to farther north (Figure 3.2b). In that region, slightly elevated values for EOF 1 are mostly found near the 2000 m isobath. The amplitude time series (Figure 3.3a and 3.3b) reveals that seasonal enhancement of frontal activity from Cape Blanc to the Iberian Peninsula occurs from late spring to fall (i.e., June to October), peaking in July to September. An abrupt phase shift is observed to the south of Cape Blanc, where large negative values for EOF 1 are observed inshore of the 2000 m isobath (Figure 3.2b). In that case, the seasonal enhancement of frontal activity occurs during late fall to early spring (December to April, peaking in February; Figure 3.3a and 3.3b), when frontal probabilities to the north of Cape Blanc are strongly reduced. This phase difference is likely associated with the previously identified differences in wind forcing in each region [*Nykjær and Van Camp*, 1994] and possibly due to the influence of the Mauritania Current [Peña-Izquierdo et al., 2012] south of Cape Blanc during summer, which advects warm water northward reducing the SST gradient between the shelf and offshore areas [*Lathuilière et al.*, 2008]. Analysis of the local fraction of the variance explained by the EOFs (as in *Chelton and Davis* [1982]; not shown) reveals that EOF 2 of frontal probabilities is most important to the southwest of the Canary Islands (16°W, 28°N; Figure 3.2f). The second EOF also captures variability in frontal activity away from the coast offshore of the 2000 m isobath off Cape Ghir, Cape Blanc and Cap-Vert. The response in the south off Cap-Vert is out of phase to the response off the other capes. Careful analysis of the amplitude time series indicates that the offshore enhancement off these three capes captured by EOF 2 occurs approximately 2-3 months after the peak in frontal activity near the coast captured by EOF 1 (Figure 3.3b and 3.3f).

EOF analysis of frontal variability in the Humboldt Current System reveals that the largest seasonal signal is observed near the coast in the southern sector between Punta Lavapie and Valparaiso (40°S to 33°S), extending for up to 220 km offshore (Figure 3.2c and Table 3.1). Strong seasonality in this region is also found for coastal upwelling indices [*Montecino et al.*, 2006], chlorophyll concentrations [*Thomas et al.*, 2009], and wind stress and wind stress curl [*Bakun and Nelson,* 1991; *Aguirre et al.,* 2012]. Farther north, between Valparaiso (33°S) and Cape Paracas (15°S), large values of EOF 1 are restricted to a narrow band near the coast. Observations are missing offshore for a large stretch of this region because of cloud contamination, however. The lowest seasonal signal as captured by EOF 1 is found between Lima (13°S) and Chiclayo (6°S), where year-round upwelling with weak seasonality has been reported [*Chavez and Messié*, 2009]. Consistently with other EBCS, the increase in frontal activity occurs during the austral summer (January-April, Figure 3.3c and 3.3d). The second EOF (Figure 3.2g) is characterized by a band of positive values near the coast and by negative values offshore. As such, it captures the increase in frontal activity near the coast during spring (October-

January, when the amplitude time series for EOF 2 is positive; Figure 3.3g and 3.3h) and the subsequent increase offshore during fall (April and May, when amplitude time series is negative). The band of positive values near the coast is quite narrow, generally of the order of 100 km or less. The increase in frontal activity away from the coast was particularly strong during austral fall 2006. We note that this shift captured by EOF 2 from a coastal enhancement near the coast during spring to higher frontal activity being found away from the coast during fall is similar to the pattern observed in the California Current System (Figures 3.2e and 3.3f; see also *Castelao and Wang* [2014]).

The shelf in the Benguela Current System is generally wider than in the other EBCS [*Smith*, 1981] (Table 3.1). Large seasonal variability of frontal probability is captured by EOF 1 inshore of the 2000 m isobath to the south of Luderiz, and around the 2000 m isobath between Luderitz and Walvis Bay (Figure 3.2d). In those regions, frontal activity is enhanced during summer to early fall (February-April), peaking in March (Figure 3.3c and 3.3d). It seems that the seasonal variability in frontal activity in those regions was smaller in 2003 and 2004 compared to during and after 2005, although the time series is possibly too short to confidently detect interannual variability. It is interesting to note that the region of high mean frontal probabilities at and to the north of Cape Frio (Figure 3.1d) associated with the Angola-Benguela Frontal Zone is characterized by small seasonal variability (Figure 3.2d), indicating that fronts are observed in that region year-round. This is consistent with *Veitch et al.* [2006] analysis of 18-year of satellite observations that showed that enhanced SST gradients are observed in the region throughout the year. The area very near the coast to the north of Orange River and approximately following the 200 m isobath to the north of Luderitz is characterized by negative values for EOF 1, indicating that seasonal evolution of fronts in that region is out of phase compared to the surrounding waters. This seems to be a robust feature of the analysis, and a similar pattern is observed in an EOF decomposition of SST gradient magnitudes (not shown). The reason for that phase difference remains unclear at this point. The second EOF of frontal probabilities in the Benguela Current System (Figure 3.2h) is characterized by positive values near the coast and by negative values offshore to the south of Walvis Bay. In that region, the mode captures the increase in frontal activity near the coast during spring and the increase offshore during fall (Figure 3.3g and 3.3h). To the north of Walvis Bay, negative values extend from the coast to about 450 km offshore (Figure 3.2h). In that region, EOF 2 explains a larger fraction of the local variance than EOF 1 does, capturing the seasonal enhancement in frontal activity during fall and early winter (Figure 3.3h).

3.4.3 Mean and variability in alongshore wind stress

Alongshore winds have been shown to play a dominant role in upwelling circulation [*Smith,* 1968; *Huyer,* 1983; *Allen et al.,* 1995, among many others] and frontal variability [e.g., *Kahru et al.,* 2012; *Castelao and Wang,* 2014] in EBCS. It is useful, therefore, to investigate alongshore wind stress variability in order to better understand its influence on frontal activity. Results from EOF decompositions of alongshore wind stress in the four EBCS are shown in Figures 3.4 and 3.5.

Our analysis of wind variability in the California Current System is consistent with results reported recently by *Castelao and Wang* [2014]. Average equatorward (i.e., negative values in the northern hemisphere) alongshore winds are intensified to the south of Cape Blanco (Figure 3.4a). The intensity of upwelling favorable winds to the north of Point Arena (EOF 1, Figure 3.4e) is stronger during summer and early fall, while upwelling winds to the south of Cape Mendocino (EOF 2) are also intensified during spring (Figure 3.5a and 3.5b, 3.5e and 3.5f).

The mean alongshore wind stress in the Canary Current System reveals that upwelling favorable conditions are observed over most of the region, except in the region around the Strait of Gibraltar where average alongshore winds are weak (Figure 3.4b). Localized intensifications in the strength of average winds are observed around major capes (e.g., Cape Finisterre, Cape Roca, Cape Ghir, Cape Bojador and Cape Blanc). The first EOF mode captures the intensification of upwelling favorable winds during spring/early summer from Cape Blanc to the Iberian Peninsula, especially around the capes mentioned above (Figures 3.4f, 3.5a, and 3.5b). The second EOF mode captures a phase shift in wind intensification between the Iberian Peninsula and the area extending from just south of the Strait of Gibraltar to Cape Blanc. In contrast to the other modes, the monthly average of the amplitude time series for mode 2 (Figure 3.5f) does not show a clear seasonal pattern, other than perhaps a slight increase during the month of July. Analysis of the amplitude time series for the individual years (Figure 3.5e) suggests that the mode is related to a few large events of interannual variability. It is interesting to note that both EOFs 1 and 2 are approximately zero to the south of Cape Blanc (Figure 3.4f), an area that is characterized by large seasonal variability in frontal activity (Figure 3.2b). Wind variability in that region is captured by EOF 3 (Figure 3.4f). Intensification in upwelling favorable winds to the south of Cape Blanc occurs from January to May, while the period from July to September is characterized by weak upwelling or even by downwelling-favorable winds (Figure 3.5f). Variability in wind forcing in this region that is different than farther north is consistent with previous investigations [e.g., *Nykjær and Van Camp,* 1994; *Lathuilière et al.,* 2008; *Arístegui et al.,* 2009; *Cropper et al.,* 2014], and it is also consistent with the increase in frontal activity in the region that occurs from January to April discussed in section 3.2 (Figures 3.2b and 3.3b).

Alongshore winds off in the Humboldt Current System are on average upwelling favorable (Figure 3.4c; positive values in the southern hemisphere). Peaks in average winds are observed near Cape Paracas and Coquimbo. The EOF decomposition of the alongshore wind stress data (Figures 3.4g, 3.5c, and 3.5d) reveals a large seasonal enhancement of upwelling winds to the south of Coquimbo at about 30°S during local spring/summer. This is consistent with *Garreaud and Muñoz* [2005], who found similar seasonality in wind stress variability at the region between Valparaiso and Punta Lavapie. This region is also characterized by strong seasonal variability in frontal probability (Figure 3.2c). The EOF also captures a somewhat weaker increase in seasonal variability in the northern section (e.g. from 17°S to 5°S), but with an opposite phase. In those areas, EOF 1 represents an increase in upwelling favorable winds during the austral winter (May-August). The spatial distribution of EOF 2 is very similar to the average winds, indicating that the upwelling winds are stronger than average over most of the region during local spring, especially in September. This is consistent with *Chavez and Messié* [2009] analysis of the temporal evolution of the vertical transport (Ekman transport plus Ekman pumping) off the coast of Peru between 20°S and the equator.

The strongest averaged alongshore upwelling favorable winds in all EBCS are observed in the Benguela Current System (Figure 3.4d). Peaks in average winds are observed off Luderitz and off Cape Frio. The EOF decomposition of the wind stress observations reveals that upwelling winds to the south of Walvis Bay are enhanced from October to March (EOF 1, Figures 3.4h, 3.5c, and 3.5d), a pattern that is similar to that observed for frontal variability in the region (Figures 3.2d and 3.3d). Between Luderitz and Cape Frio, stronger upwelling winds are found during spring (EOF 2; Figures 3.4h, 3.5g, and 3.5h). To the north of about 15°S, both EOFs are relatively small, indicating that wind variability is reduced. Persistent winds with low variability is consistent with frontal activity in that region, which is similarly characterized by persistent frontal occurrence with little seasonal variations (Figures 3.1d, 3.2d, and 3.2h), Fronts in the region are also associated with the convergence zone of the southward-flowing Angola Current and the northward extent of the Benguela upwelling regime [*Veitch et al.,* 2006].

3.4.4 Coupling between frontal probabilities and alongshore wind stress

The spatial distributions described above for the average fields and for the dominant modes of variability in frontal probabilities and alongshore wind stress present several similarities. This is most clearly seen in Figure 3.4, where the mean and EOFs of frontal probability averaged within 400 km from the coast are also shown as a function of latitude (dashed lines). In most instances, there is a remarkable overlap in the regions of enhanced mean winds and frontal activity (Figures 3.4a–3.4d). The exception is the Humboldt Current System (Figure 3.4c), where even though there is substantial variability in the average magnitude of the alongshore wind stress, average frontal probability within 400 km from shore is characterized by small alongshore variability. It is important to point out that alongshore variations in the intensity and on the width of the region of high frontal activity are observed, however (Figure 3.1c). There is also substantial overlap in the areas of enhanced variability in winds and fronts, as identified by the respective dominant EOFs (Figures 3.4e–3.4h, solid and dashed blue lines). This is true not only for the large-scale patterns (e.g., enhancements between Cape Blanco and Cape Mendocino in the California Current System and to the south of Coquimbo in the Humboldt Current System; Figures 3.4e and 3.4g), but also for smaller-scale variations likely associated with topographic effects (e.g., Figure 3.4f). Careful analysis of the amplitude time series (Figures 3.3 and 3.5) reveals that in several instances the strengthening of upwelling winds is followed by enhancements in frontal activity in all EBCS. Overlap in the areas of enhanced variability in winds and fronts captured by EOF

2 in less evident, being only clearly observed in the California Current System (Figure 3.4e).

Castelao and Wang [2014] compared time series of anomalies (computed by removing the long-term aver- age for each month from the monthly time series) in alongshore wind stress and frontal probabilities in the California Current System. They showed that anomalously weak upwelling or strong downwelling wind stress is generally associated with anomalously low frontal activity, while anomalously strong upwelling or weak downwelling wind stress is generally accompanied by anomalously high frontal activity in the following month. Here, we expand their analysis to the other EBCS. The analysis is focused on regions characterized by high seasonal variability in both frontal activity and wind intensity as identified by the EOF decompositions (i.e., in the area delineated by black lines in Figure 3.2a-3.2d). Only observations within 200 km from the coast are used in each region for consistency. This band approximately encompasses the region with high mean frontal activity in all EBCS (Table 3.1). After spatially averaging the observations, the time series of averaged frontal probability and alongshore wind stress are prewhiten by removing the monthly averages, respectively. For example, to generate the frontal probability anomaly for January 2004, we subtract the average of all January frontal probabilities (2003–2009) from the January 2004 frontal probability. The motivation for prewhitening the time series is that, by removing the long-term monthly averages, the effective number of degrees of freedom increases, improving statistical reliability of the analysis. As discussed in *Chelton* [1982], this procedure does not remove any true physical relationship between the two time series, since the seasonal variation of a quantity is never a pure-tone harmonic. If the seasonal alongshore wind stress is stronger than average or peak earlier than usual during a certain year, for example, then frontal activity should also be stronger than average or peak earlier than usual if a connection between the two variables exist.

Scatterplots and linear regressions (with confidence intervals) between frontal activity and wind stress anomalies for each EBCS are shown in Figure 3.6. The coordinate system used is such that negative (positive) wind anomalies in the northern (southern) hemisphere represent anomalously strong upwelling favorable winds or anomalously weak downwelling favorable winds. Results show that significant correlations (at the 95% confidence level) are observed in all of EBCS. In all cases, upwelling favorable wind anomalies are associated with anomalously strong frontal activity, while periods of anomalously weak upwelling or strong downwelling winds are accompanied by anomalously weak frontal activity. The absolute values of the slope of the regression between winds and frontal activity vary by as much as 50% between the regions, although the differences are within the uncertainty in the estimation of the coefficients.

It is important to emphasize that the significant correlations observed in all EBCS between wind forcing and SST frontal variability (Figure 3.6) do not necessarily imply direct causation. The correlations also do not necessarily mean that the relationship between forcing and front activity is linear. Stronger upwelling favorable winds may lead to enhanced frontal activity due to increased upwelling, but it can also lead to stronger cur- rents which can more easily become unstable. Instabilities have been shown to substantially influence frontogenesis [e.g., *Capet et al.,* 2008]. Stronger winds may also lead to a stronger nonlinear upwelling jet and to stronger interactions with topography, which are also know to influence front activity [e.g., *Holladay and O'Brien*, 1975]. In those scenarios, anomalies in frontal activity may be correlated to anomalies in wind forcing, even though they are generated by other processes. Thus, using a linear regression is a simplification, since the relationship may be nonlinear.

3.5 Discussion

Eastern Boundary Current Systems (EBCS) are highly dynamical regions characterized by persistent or seasonal upwelling and strong frontal activity (Figure 3.1). Variability in alongshore wind stress and frontal probability is dominated by seasonal scales (Figures 3.2-3.5). Variability in frontal activity seems to be strongly tied to variability in alongshore wind stress, both spatially and temporally. There is substantial overlap in the areas where the dominant EOFs of both variables are large (Figure 3.4e-3.4h), and anomaly fields are significantly correlated temporally so that stronger upwelling favorable winds are usually associated by enhanced frontal occurrence (Figure 3.6). This is consistent with the dominant pattern of variability observed in the California Current System [*Castelao and Wang*, 2014], revealing a large degree of similarity in the different EBCS to lowest order.

A common feature among most EBCS is the first appearance of fronts near the coast during spring, which is followed by an enhancement in frontal activity away from the coast during fall. This pattern is captured by EOF 2 in the California, Humboldt and southern Benguela Current Systems, and in the Canary Current System near Cape Ghir, north of Cape Blanc, and off Cap-Vert (Figures 3.2 and 3.3). Front activity offshore in the Canary Current System is strongly influenced by the Canary Islands (~28°N).

Comparison between EOFs of winds and fronts suggests that geographic extent plays an important role controlling variability in frontal activity and the relation between frontal probability and wind stress. High seasonal variability in frontal activity peaking during summer/early fall is observed in mid-latitudes in all regions (Figure 3.2a-3.2d), possibly because seasonal variability in alongshore wind stress is also enhanced in those areas (Figure 3.4). At high latitudes (beyond the limits shown in Figure 3.2), the seasonal intensification in frontal probabilities is reduced (not shown), as winds become predominantly downwelling favorable [*Strub et al.*, 2013]. Seasonal variability in frontal activity is also reduced at low latitudes (north of ~15°S) in the Humboldt and Benguela Current Systems (Figure 3.2c and 3.2d), even though average frontal probabilities are relatively high (especially in the Benguela Current System and off Cape Paracas and north of Chiclayo in the Humboldt Current System, Figure 3.1c and 3.1d). In those areas, winds tend to be upwelling favorable year round with a reduced seasonal signal (Fig 3.4c, 3.4d, 3.4g, and 3.4h, see also Figure 14.7 in *Strub et al.* [2013]), a pattern also observed for low latitudes in the California Current System [*Strub et al.*, 1987]. To the south of

Cape Blanc in the Canary Current System, however, seasonal variability in frontal activity is high (Figure 3.2b). The seasonal evolution of frontal probabilities is out of phase compared to mid-latitude regions, though, peaking during winter (Figure 3.3a and 3.3b). Upwelling favorable winds in the southern Canary Current System are stronger during winter (see EOF 3 of alongshore winds, Figures 3.4f, 3.5e and 3.5f) when the Intertropical Convergence Zone (ITCZ) is displaced southward [*Strub et al.*, 2013]. During summer, the ITCZ moves northward resulting in relatively weaker winds to the south of Cape Blanc. Additionally, poleward horizontal advection of warm waters by the Mauritania Current in summer [*Mittelstaedt,* 1991; *Stramma et al.,* 2005] likely contributes to reduced SST gradients in the region [*Lathuilière et al.,* 2008].

The influence of coastline and bottom topography perturbations on frontal activity also seems to be ubiquitous of EBCS, with increased frontal probabilities being observed near major capes. Those areas are often characterized by enhanced upwelling [e.g., *Samelson et al.,* 2002; *Huyer et al.,* 2005; *Veitch et al.,* 2009] associated with strong wind forcing [*Perlin et al.,* 2004; *Chelton et al.,* 2007], variations in bottom bathymetry [*Peffley and O'Brien*, 1976] and coastline orientation [*Gan and Allen*, 2002], and variations in vorticity resulting from curvature of the trajectory as the flow passes the capes [*Arthur*, 1965].

One important difference among EBCS is the relation between the spatial patterns of the average and the dominant mode of variability in frontal activity (Figures 3.1a-3.1d, 3.2a-3.2d and 3.4, dashed lines). While in the California Current System they are similar to each other (dashed green and blue lines in Figure 3.4a and 3.4e), that are not always true in other areas. In the Canary Current System, for example, the largest average probabilities are observed within a few hundred kilometers from Cape Blanc (Figure 3.4b, dashed green), while large seasonal variability is observed farther north, off Cape Ghir and off the Iberian Peninsula (Figure 3.4f, dashed blue). Seasonal variability in frontal probability off Cape Blanc is actually reduced (Figure 3.4f, dashed blue). The same is observed in the northern Benguela Current System, where frontal probabilities are high of Cape Frio (Figure 3.1d), but seasonal variability is small (Figure 3.2d). Significant differences in the width of the region with high variability in frontal probabilities are also observed in the different EBCS. The region is relatively broad in the California and Benguela Current Systems (300-350km; Table 3.1), and narrower in the Canary and Humboldt Current Systems (200-220 km). There are many processes that can influence the width of the band with high frontal activity near the coast, including shelf width, the intensity of alongshore winds [*Jiang et al.,* 2011*; Castelao and Wang*, 2014], variations in Ekman transport [*Breaker and Mooers*, 1986], variations in the offshore extent of upwelling favorable wind stress curl [*Bakun and Nelson,* 1991; *Albert et al.,* 2010], flow topography interactions [*Barth et al.*, 2000; *Castelao et al.*, 2005], and offshore propagation of mesoscale dynamics [*Chaigneau et al.,* 2009; *Gruber et al.*, 2011]. Altimetry observations show that variability at intraseasonal (eddy) scales is indeed larger at mid-latitudes in the California and Benguela Current Systems than off Peru and Northwest Africa [*Chavez and Messié*, 2009]. Modeling simulations comparing eddy activity off NW Africa and California reveal that higher mesoscale variability off California is at least partially related to its stronger background stratification [*Marchesiello and Estrade*, 2009]. In the Benguela Current System, stream functions of the flow in the top 1000 m reveal a convergence zone off Luderitz. The convergence is due to equatorward flow in the southern Benguela [*Hutchings et al.*, 2009] and poleward flow in the northern Benguela likely associated with the wind stress curl distribution via the Svertrup relation [*Veitch et al.*, 2009]. The convergence zone is associated with offshore flow and the formation of cyclonic eddies of Luderitz [*Hutchings et al.*, 2009], which could potentially contribute to widening the region of high frontal activity in the Benguela Current System.

Several recent studies have suggested that the strength of the alongshore wind stress in Eastern Boundary Current Systems may have been increasing over the last decades due to greenhouse-associated intensification of thermal low-pressure cells over the coastal landmass of upwelling regions [*Bakun et al.*, 2010]. Analysis of sediment cores off Cape Ghir at Northwest Africa suggests a rapid increase in coastal upwelling in the region during the 20th century, which coincides with the rise in atmospheric CO2 [*McGregor et al.*, 2007]. Wind observations and reanalysis products also reveal an increase in the intensity of upwelling favorable winds to the north of Cape Blanc [*Cropper et al.*, 2014]. Long-term observations in the Benguela Current System show decreasing SST near the coast and increasing SST offshore due to strengthening of coastal upwelling [*Santos et al.*, 2012]. This will presumably lead to an increase in SST gradients in the region. No clear pattern of increase in frontal probability is observed in the four EBCS analyzed here (Figure 3.3), however, possibly because the time series are too short to detect long term trends. Using a longer time series extending for about 30 years, *Kahru et al.* [2012] reported decadal-scale increasing trends in the frequency of both SST and chlorophyll fronts in the California Current System. It would be interesting to repeat those analyses to the other EBCS to investigate if similar trends are observed.

Last, this study has revealed that, although several similarities are observed among the different EBCS, multiple important differences do occur. These similarities and differences in the systems (temporal and/or spatial) can be used to set up “natural experiments” in which forcing and frontal variability are compared among the systems. This approach may prove helpful to disentangle the mechanisms controlling frontal variability in EBCS.

In summary, seven years of satellite observations are used to describe the dominant modes of variability in SST frontal activity and alongshore wind stress in the California, Canary, Humboldt and Benguela Current Systems. The general characteristics of the different EBCS are similar, with strong seasonality of both variables especially at mid-latitudes. In all regions, frontal activity is generally enhanced in the vicinity of the major capes. The seasonal evolution of fronts and alongshore winds are strongly correlated, with intensified upwelling favorable winds associated with higher frontal probabilities. An offshore migration of the region of high frontal activity is generally observed, with fronts first appearing close to the coast during spring moving offshore during summer and fall. Perhaps the most striking difference in frontal distribution among the different EBCS is the width of the region of enhanced seasonal variability. The area is broader in the Benguela and California Current Systems and narrower in the Canary and Benguela Current Systems, possibly because of differences in shelf width, wind forcing and mesoscale variability. Analyses of longer times series of SST frontal probabilities spanning the four EBCS should allow for interannual variability, including long term trends, to be confidently detected.

3.6 Acknowledgements

We thank three anonymous reviewers for their thoughtful comments and suggestions, which led to a greatly improved manuscript. We gratefully acknowledge support by NASA (Ocean Vector Winds Science Team grant NNX14AM70G and grant NNX10AE92G). All observations used here are available at http://podaac.jpl.nasa.gov.

References

Aguirre, C., Ó. Pizarro, P. T. Strub, R. Garreaud, and J. A. Barth (2012), Seasonal dynamics of the near-surface alongshore flow off central Chile, *J. Geophys. Res.*, *117*, C01006, doi:10.1029/2011JC007379.

Albert, A., V. Echevin, M. Lévy, and O. Aumont (2010), Impact of nearshore wind stress curl on coastal circulation and primary productivity in the Peru upwelling system, *J. Geophys. Res.*, *115*, C12033, doi:10.1029/2010JC006569.

Allen, J. S., P. A. Newberger, and J. Federiuk (1995), Upwelling circulation on the Oregon continental shelf. Part I: Response to idealized forcing, *J. Phys. Oceanogr.*, *25*, 1843–1866, doi: http://dx.doi.org/10.1175/1520-0485(1995)025<1843:UCOTOC>2.0.CO;2

Arístegui, J., E. D. Barton, X. A. Álvarez-Salgado, A. M. P. Santos, F. G. Figueiras, S. Kifani, S. Hernández-León, E. Mason, E. Machú, and H. Demarcq (2009), Sub-regional ecosystem variability in the Canary Current upwelling, *Prog. Oceanogr.*, *83*, 33-48, doi:10.1016/ j.pocean.2009.07.031.

Arthur, R. S. (1965), On the calculation of vertical motion in eastern boundary currents from determinations of horizontal motion, *J. Geophys. Res.*, *70*(12), 2799–2803, doi:10.1029/JZ070i012p02799.

Bakun, A., and C. S. Nelson (1991), The seasonal cycle of wind-stress curl in subtropical eastern boundary current regions, *J. Phys. Oceanogr.*, *21*, 1815–1834, doi: http://dx.doi.org/10.1175/1520-0485(1991)021<1815:TSCOWS>2.0.CO;2

Bakun, A., D. B. Field, A. N. A. Redondo-Rodriguez, and S. J. Weeks (2010), Greenhouse gas, upwelling-favorable winds, and the future of coastal ocean upwelling ecosystems, *Glob. Change Biol.*, *16*, 1213–1228. doi: 10.1111/j.1365-2486.2009.02094.x

Barber, R. T. and W. O. Smith (1981), The role of circulation, sinking, and vertical migration in physical sorting of phytoplankton in the upwelling center at 15°S, in *Coastal Upwelling*, edited by F. A. Richards, pp. 366-371, AGU, Washington, D. C.

Barth, J. A., S. D. Pierce, and R. L. Smith (2000), A separating coastal upwelling jet at Cape Blanco, Oregon and its connection to the California Current System, *Deep Sea Res. Part II.*, *47*(5–6), 783-810, doi: http://dx.doi.org/10.1016/S0967-0645(99)00127-7.

Bowman, M. J., and R. L. Iverson (1978), Estuarine and plume fronts, in *Oceanic fronts in coastal processes*, edited by M. J. Bowman and W. E. Esaias, pp. 87-104, Springer Berlin Heidelberg

Breaker, L. C., and C. N. K. Mooers (1986), Oceanic variability off the Central California coast, *Prog. Oceanogr.*, *17*(1), 61-135, doi: http://dx.doi.org/10.1016/0079-6611(86)90025-X.

Canny, J. (1986), A computational approach to edge detection, *IEEE Trans. Pattern Anal. Mach. Intell.*, *6*, 679–698. doi:10.1109/TPAMI.1986.4767851.

Capet, X., J. C. McWilliams, M. J. Molemaker, and A. F. Shchepetkin (2008), Mesoscale to submesoscale transition in the California Current System. Part II: Frontal processes, *J. Phys. Oceanogr., 38,* 44–64.

Carr, M.-E., and E. J. Kearns (2003), Production regimes in four eastern boundary current systems, *Deep Sea Res. Part II*, *50*(22-26), 3199-3221, doi: http://dx.doi.org/10.1016/j.dsr2.2003.07.015.

Castelao, R. M., and Y. Wang (2014), Wind-driven variability in sea surface temperature front distribution in the California Current System, *J. Geophys. Res.: Oceans*, *119*(3), 1861–1875, doi:10.1002/2013JC009531.

Castelao, R. M., J. A. Barth, and T. P. Mavor (2005), Flow-topography interactions in the northern California Current System observed from geostationary satellite data, *Geophys. Res. Lett.*, *32*, L24612, doi:10.1029/2005GL024401.

Castelao, R. M., T. P. Mavor, J. A. Barth, and L. C. Breaker (2006), Sea surface temperature fronts in the California Current System from geostationary satellite observations, *J. Geophys. Res.*, *111*, C09026, doi:10.1029/2006JC003541.

Chaigneau, A., G. Eldin, and B. Dewitte (2009), Eddy activity in the four major upwelling systems from satellite altimetry (1992–2007), *Prog. Oceanogr.*, *83*(1-4), 117-123, doi: http://dx.doi.org/10.1016/j.pocean.2009.07.012.

Chavez, F. P., and M. Messié (2009), A comparison of eastern boundary upwelling ecosystems, *Prog. Oceanogr.*, *83*(1-4), 80-96, doi: http://dx.doi.org/10.1016/j.pocean.2009.07.032.

Chelton, D. B. (1982), Large-scale response of the California Current to forcing by the wind stress curl, *CalCOFI Rep., 23,* 130-148.

Chelton, D. B., and R. E. Davis (1982), Monthly mean sea-level variability along the west coast of North America, *J. Phys. Oceanogr.*, *12*(8), 757–784, doi: http://dx.doi.org/10.1175/1520-0485(1982)012<0757:MMSLVA>2.0.CO;2

Chelton, D. B., and M. H. Freilich (2005), Scatterometer-based assessment of 10-m wind analyses from the operational ECMWF and NCEP numerical weather prediction models, *Mon. Wea. Rev.*, *133*(2), 409–429, doi: http://dx.doi.org/10.1175/MWR-2861.1

Chelton, D. B., M. G. Schlax, M. H. Freilich, and R. F. Milliff (2004), Satellite measurements reveal persistent small-scale features in ocean winds, *Science*, *303*(5660), 978-983. doi:10.1126/science.1091901

Chelton, D. B., M. G. Schlax, and R. M. Samelson (2007), Summertime coupling between sea surface temperature and wind stress in the California Current System, *J. Phys. Oceanogr.*, *37*(3), 495–517, doi: http://dx.doi.org/10.1175/JPO3025.1

Cropper, T. E., E. Hanna, and G. R. Bigg (2014), Spatial and temporal seasonal trends in coastal upwelling off Northwest Africa, 1981–2012, *Deep Sea Res. Part I*, *86*, 94-111, doi: http://dx.doi.org/10.1016/j.dsr.2014.01.007.

Ekman, V. W. (1905), On the influence of the Earth's rotation on ocean currents, *Arch. Math. Astron. Phys.*, *2*, 1-52.

Gan, J., and J. S. Allen (2002), A modeling study of shelf circulation off northern California in the region of the Coastal Ocean Dynamics Experiment: Response to relaxation of upwelling winds, *J. Geophys. Res.*, *107*(C9), 3123, doi:10.1029/2000JC000768.

Garreaud, R., and R. C. Muñoz (2005), The Low-Level Jet off the West Coast of Subtropical South America: Structure and Variability, *Mon. Weather Rev., 133*(8), 2246-2261, doi:10.1175/MWR2972.1.

Gruber, N., Z. Lachkar, H. Frenzel, P. Marchesiello, M. Münnich, J. C. McWilliams, T. Nagai, and G.-K. Plattner (2011), Eddy-induced reduction of biological production in eastern boundary upwelling systems, *Nature Geosci*, *4*(11), 787-792, doi: http://dx.doi.org/10.1038/ngeo1273

Haynes, R., E. D. Barton, and I. Pilling (1993), Development, persistence, and variability of upwelling filaments off the Atlantic coast of the Iberian Peninsula, *J. Geophys. Res.*, *98*(C12), 22681–22692, doi:10.1029/93JC02016.

Holladay, C. G., and J. J. O'Brien (1975), Mesoscale variability of sea surface temperature, *J. Phys. Oceanogr., 5,* 761–772.

Hutchings, L., et al. (2009), The Benguela Current: An ecosystem of four components, *Prog. Oceanogr.*, *83*(1-4), 15-32, doi: http://dx.doi.org/10.1016/j.pocean.2009.07.046.

Huyer, A. (1983), Coastal upwelling in the California Current system, *Prog. Oceanogr.*, *12*(3), 259-284, doi: http://dx.doi.org/10.1016/0079-6611(83)90010-1.

Huyer, A., J. H. Fleischbein, J. Keister, P. M. Kosro, N. Perlin, R. L. Smith, and P. A. Wheeler (2005), Two coastal upwelling domains in the northern California Current system, *J. Mar. Res.*, *63*(5), 901-929, doi: http://dx.doi.org/10.1357/002224005774464238.

Jiang, L., X.-H. Yan, Y.-H. Tseng, and L. C. Breaker (2011), A numerical study on the role of wind forcing, bottom topography, and nonhydrostacy in coastal upwelling, *Est. Coast. Shelf Sci., 95*(1), 99-109, doi:http://dx.doi.org/10.1016/j.ecss.2011.08.019.

Kahru, M., E. Di Lorenzo, M. Manzano-Sarabia, and B. G. Mitchell (2012), Spatial and temporal statistics of sea surface temperature and chlorophyll fronts in the California Current, *J. Plankton Res.*, *34*(9), 749-760, doi:10.1093/plankt/fbs010.

Kostianoy, A. G., and J. R. E. Lutjeharms (1999), Atmospheric effects in the Angola-Benguela frontal zone, *J. Geophys. Res.*, *104*(C9), 20963–20970, doi:10.1029/1999JC900017.

Lathuilière, C., V. Echevin, and M. Lévy (2008), Seasonal and intraseasonal surface chlorophyll-a variability along the northwest African coast, *J. Geophys. Res.*, *113*, C05007, doi:10.1029/2007JC004433.

Legeckis, R. (1978), A survey of worldwide sea surface temperature fronts detected by environmental satellites, *J. Geophys. Res.*, *83*(C9), 4501–4522, doi:10.1029/JC083iC09p04501.

Marchesiello, P., and P. Estrade (2009), Eddy activity and mixing in upwelling systems: a comparative study of Northwest Africa and California regions, *Int. J. Earth Sci.*, *98*(2), 299-308, doi: http://dx.doi.org/10.1007/s00531-007-0235-6.

Mavor, T. P., and J. J. Bisagni (2001), Seasonal variability of sea-surface temperature fronts on Georges Bank, *Deep Sea Research Part II*, *48*(1), 215-243, doi: http://dx.doi.org/10.1016/S0967-0645(00)00120-X.

McCreary, J.P. (1981), A linear stratified ocean model of the Coastal Undercurrent*, Phil. Trans. Roy. Soc. Lond., 302A*, 385-413.

McGregor, H. V., M. Dima, H. W. Fischer, and S. Mulitza (2007), Rapid 20th-century increase in coastal upwelling off northwest Africa, *Science*, *315*(5812), 637-639, doi:10.1126/science.1134839.

Meunier, T., E. D. Barton, B. Barreiro, and R. Torres (2012), Upwelling filaments off Cap Blanc: Interaction of the NW African upwelling current and the Cape Verde frontal zone eddy field?, *J. Geophys. Res*., *117*, C08031, doi:10.1029/2012JC007905.

Mittelstaedt, E. (1991), The ocean boundary along the northwest African coast: Circulation and oceanographic properties at the sea surface, *Prog. Oceanogr.*, *26*(4), 307-355, doi: http://dx.doi.org/10.1016/0079-6611(91)90011-A.

Montecino, V., T. Strub, F. Chavez, A. Thomas, J. Tarazona, and T. Baumgartner (2006), Bio-physical interactions off western South America, in *The Sea*, *14*, edited by A. R. Robinson and K. H. Brink, chap. 10, pp. 329–390, Harvard Univ. Press, Cambridge, Mass.

Nieto, K., H. Demarcq, and S. McClatchie (2012), Mesoscale frontal structures in the Canary Upwelling System: New front and filament detection algorithms applied to spatial and temporal patterns, *Remote Sens. Environ.*, *123*, 339-346, doi: http://dx.doi.org/10.1016/j.rse.2012.03.028.

Nykjær, L., and L. Van Camp (1994), Seasonal and interannual variability of coastal upwelling along northwest Africa and Portugal from 1981 to 1991, *J. Geophys. Res.*, *99*(C7), 14197–14207, doi:10.1029/94JC00814.

O'Neill, L. W., D. B. Chelton, and S. K. Esbensen (2010), The effects of SST-induced surface wind speed and direction gradients on midlatitude surface vorticity and divergence, *J. Climate.*, *23*, 255–281, doi: http://dx.doi.org/10.1175/2009JCLI2613.1

Overland, J. E., and R. W. Preisendorfer (1982), A significance test for principal components applied to a cyclone climatology, *Mon. Wea. Rev.*, *110*(1), 1–4, doi: http://dx.doi.org/10.1175/1520-0493(1982)110<0001:ASTFPC>2.0.CO;2

Peffley, M. B., and J. J. O'Brien (1976), A three-dimensional simulation of coastal upwelling off Oregon, *J. Phys. Oceanogr.*, *6*(2), 164–180, doi: http://dx.doi.org/10.1175/1520-0485(1976)006<0164:ATDSOC>2.0.CO;2

Peña-Izquierdo, J., J. Pelegrí, M. Pastor, P. Castellanos, M. Emelianov, M. Gasser, J. Salvador, and E. Vázquez-Domınguez (2012), The continental slope current system between Cape Verde and the Canary Islands, Sci. Mar., 76, 65–78, doi:10.3989/scimar.03607.18C.

Perlin, N., R. M. Samelson, and D. B. Chelton (2004), Scatterometer and model wind and wind stress in the Oregon–Northern California coastal zone, *Mon. Weather Rev.*, *132*(8), 2110–2129, doi: http://dx.doi.org/10.1175/1520-0493(2004)132<2110:SAMWAW>2.0.CO;2

Pickett, M. H., and J. D. Paduan (2003), Ekman transport and pumping in the California Current based on the U.S. Navy's high-resolution atmospheric model (COAMPS), *J. Geophys. Res.*, *108*, 3327, doi:10.1029/2003JC001902, C10.

Rouault, M., S. Illig, C. Bartholomae, C.J.C. Reason, and A. Bentamy (2007), Propagation and origin of warm anomalies in the Angola Benguela upwelling system in 2001. *J. Mar. Syst. 68*, 473–488, doi: http://dx.doi.org/10.1016/j.jmarsys.2006.11.010.

Ryther, J. H. (1969), Photosynthesis and fish production in the sea, *Science*, *166*(3901), 72-76, doi: 10.1126/science.166.3901.72

Samelson, R., P. Barbour, J. Barth, S. Bielli, T. Boyd, D. Chelton, P. Kosro, M. Levine, E. Skyllingstad, and J. Wilczak (2002), Wind stress forcing of the Oregon coastal ocean during the 1999 upwelling season, *J. Geophys. Res.*, *107*(C5), doi:10.1029/2001JC000900.

Santos, F., M. Gomez-Gesteira, M. deCastro, and I. Alvarez (2012), Differences in coastal and oceanic SST trends due to the strengthening of coastal upwelling along the Benguela current system, *Cont. Shelf Res.*, *34*, 79-86, doi: http://dx.doi.org/10.1016/j.csr.2011.12.004.

Smith, R. L. (1968), Upwelling*, Oceanogr. Mar. Biol. Annu. Rev.*, *6*, 11–46.

Smith, R. L. (1981), A Comparison of the Structure and Variability of the Flow Field in three Coastal Upwelling Regions: Oregon, Northwest Africa, and Peru, in *Coastal Upwelling*, edited by F. A. Richards, AGU, Washington, D. C.. doi: 10.1029/CO001p0107

Spall, M. A. (2007), Midlatitude Wind Stress–Sea Surface Temperature Coupling in the Vicinity of Oceanic Fronts, *J. Climate*, *20*(15), 3785–3801, doi:

http://dx.doi.org/10.1175/JCLI4234.1

Stramma, L., S. Hüttl, and J. Schafstall (2005), Water masses and currents in the upper tropical northeast Atlantic off northwest Africa, *J. Geophys. Res.*, *110*, C12006, doi:10.1029/2005JC002939.

Strub, P. T., J. S. Allen, A. Huyer, R. L. Smith, and R. C. Beardsley (1987), Seasonal cycles of currents, temperatures, winds, and sea level over the northeast Pacific continental shelf: 35°N to 48°N, *J. Geophys. Res.*, *92*(C2), 1507–1526, doi:10.1029/JC092iC02p01507.

Strub, P. T., V. Combes, F. A. Shillington, and O. Pizarro (2013), Chapter 14 - Currents and Processes along the Eastern Boundaries, in *Ocean Circulation and Climate A 21st Century Perspective*, *103*, 339-384, Elsevier Science.

Sverdrup, H. U., M. W. Johnson, and R. H. Fleming (1942), *The Oceans: Their physics, chemistry, and general biology*, pp. 1087, Prentice Hall, Upper Saddle River, N. J.

Thomas, A. C., P. Brickley, and R. Weatherbee (2009), Interannual variability in chlorophyll concentrations in the Humboldt and California Current Systems, *Prog. Oceanogr.*, *83*(1), 386-392, doi: http://dx.doi.org/10.1016/j.pocean.2009.07.020.

Ullman, D. S., and P. C. Cornillon (1999), Satellite-derived sea surface temperature fronts on the continental shelf off the northeast U.S. coast, *J. Geophys. Res.*, *104*(C10), 23459–23478, doi:10.1029/1999JC900133.

Vazquez-Cuervo, J., B. Dewitte, T. M. Chin, E. M. Armstrong, S. Purca, and E. Alburqueque (2013), An analysis of SST gradients off the Peruvian Coast: The impact of going to higher resolution, *Remote Sens. Environ.*, *131*, 76-84, doi: http://dx.doi.org/10.1016/j.rse.2012.12.010.

Veitch, J. A., P. Florenchie, and F. A. Shillington (2006), Seasonal and interannual fluctuations of the Angola–Benguela Frontal Zone (ABFZ) using 4.5 km resolution satellite imagery from 1982 to 1999, *Int. J. Remote Sens., 27*(5), 987-998, doi:10.1080/01431160500127914.

Veitch, J., P. Penven, and F. Shillington (2009), The Benguela: A laboratory for comparative modeling studies, *Prog. Oceanogr.*, *83*(1), 296-302, doi: http://dx.doi.org/10.1016/j.pocean.2009.07.008.

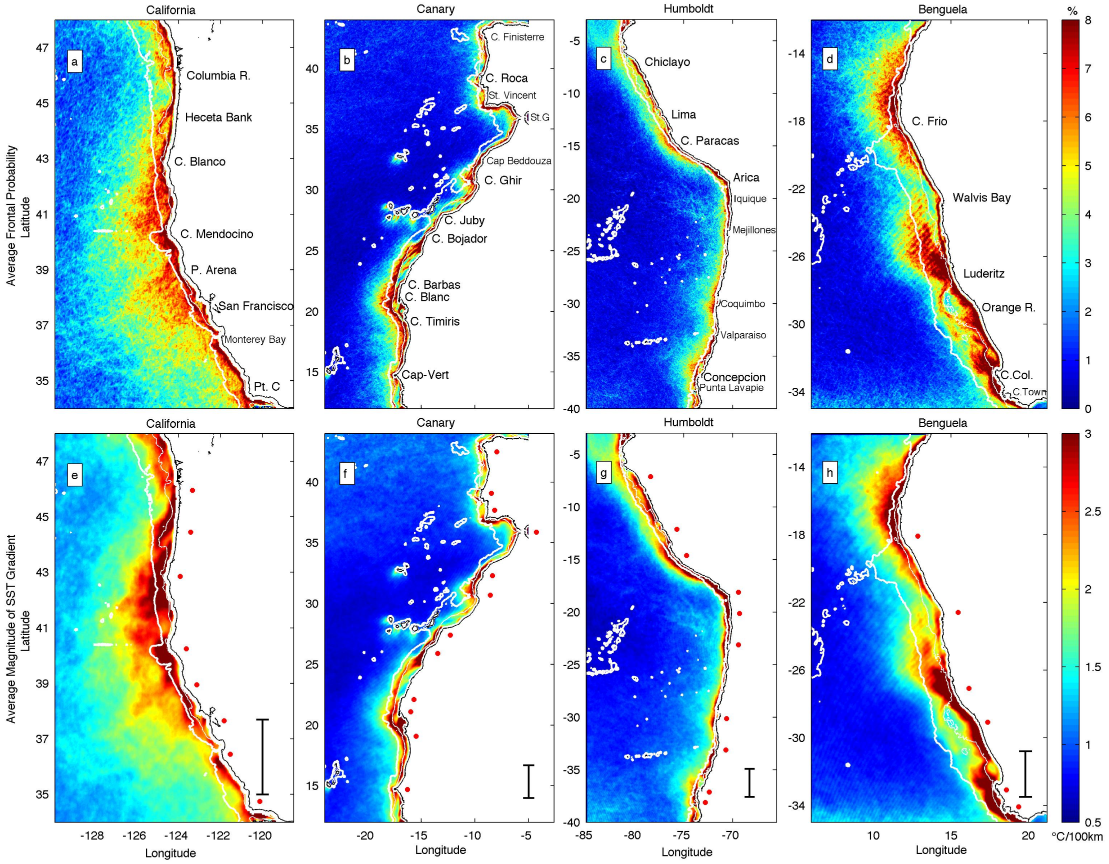

Figure 3.1 - Average frontal probability (%; a-d) and SST gradient magnitude (°C per 100 km; e-h) from 2003 to 2009 in the California (a, e), Canary (b, f), Humboldt (c, g) and Benguela (d, h) Current Systems. Major cities and capes are labeled in the top panels, while their locations are marked by red dots in the bottom panels. Thin and thick white contours show the 200 and 2000 m isobaths, respectively. The black bars in the bottom panels show a meridional distance of 300 km.

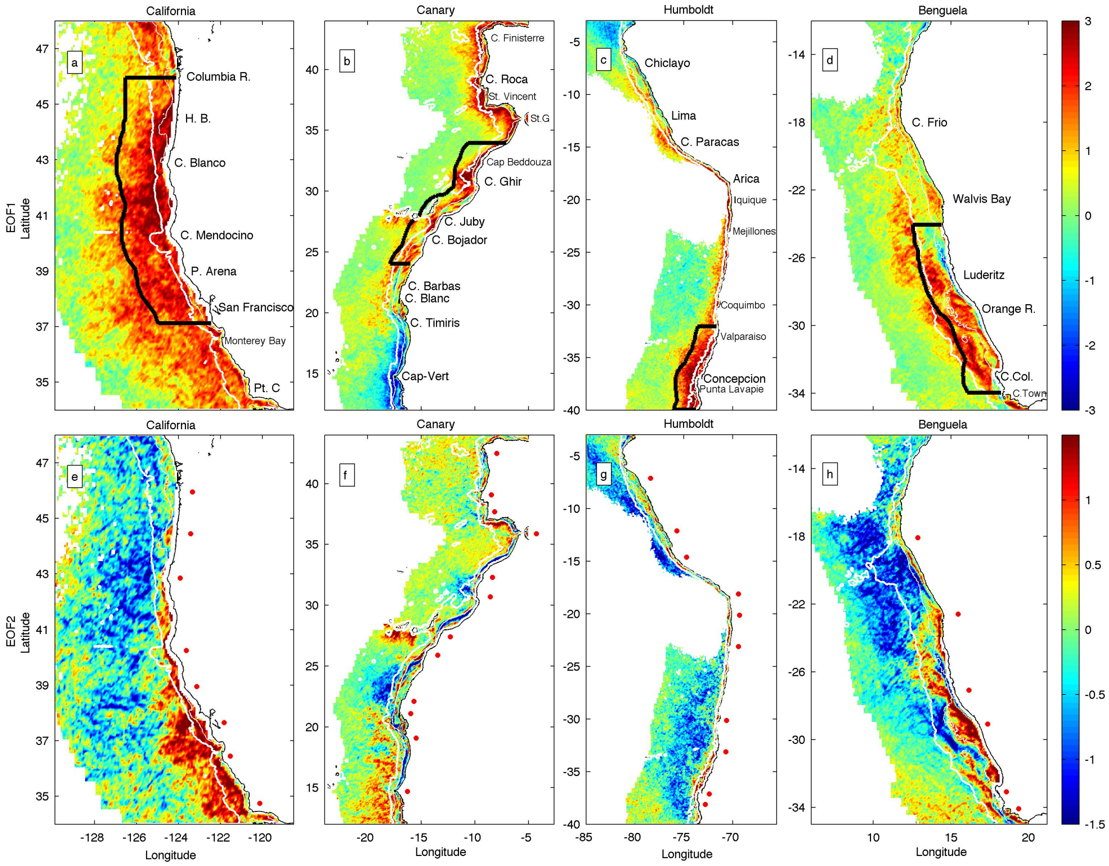

Figure 3.2 - First (a-d) and second (e-h) EOF modes of SST frontal probability. The thick black lines in the top panels indicate the regions used in Figure 3.6.

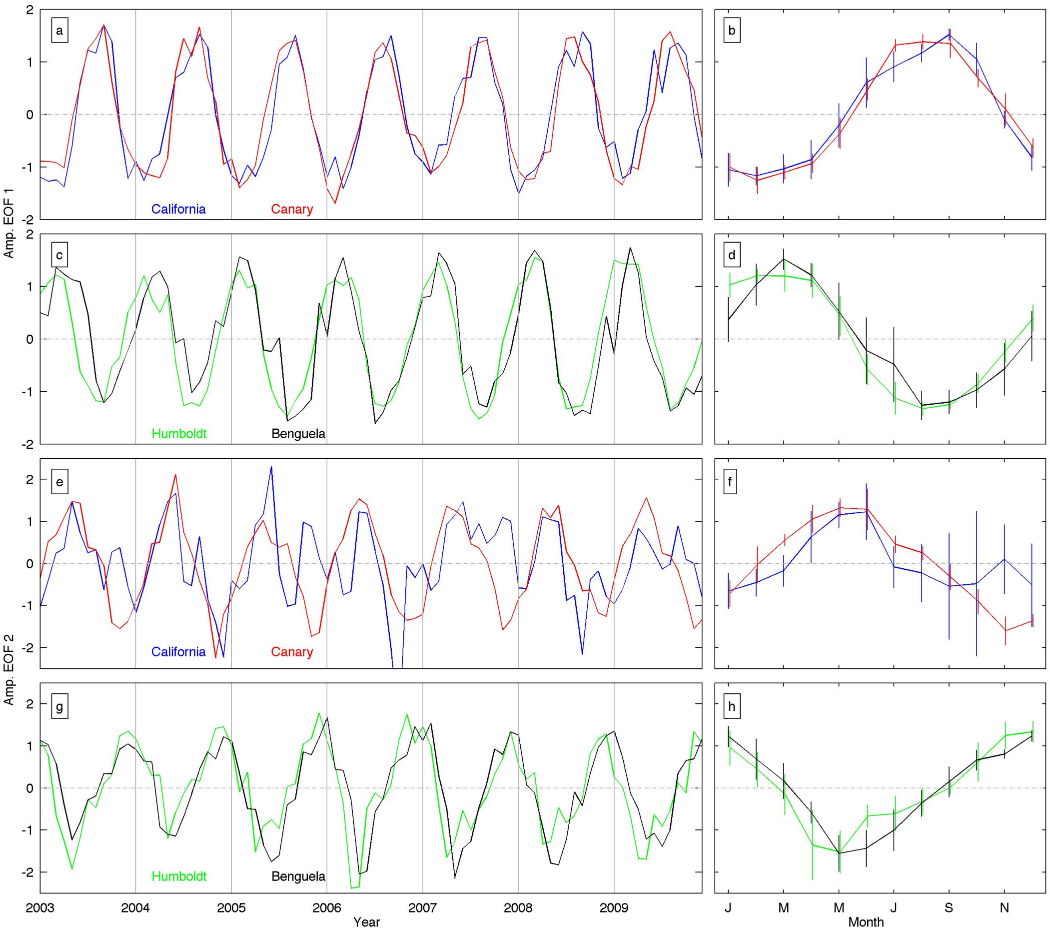

Figure 3.3 - Amplitude time series for EOFs 1 (a-d) and 2 (e-h) of frontal probabilities, color coded for the different EBCS. Values for each month are shown on the left panels, while right panels show the monthly averages ± 1 standard deviation.

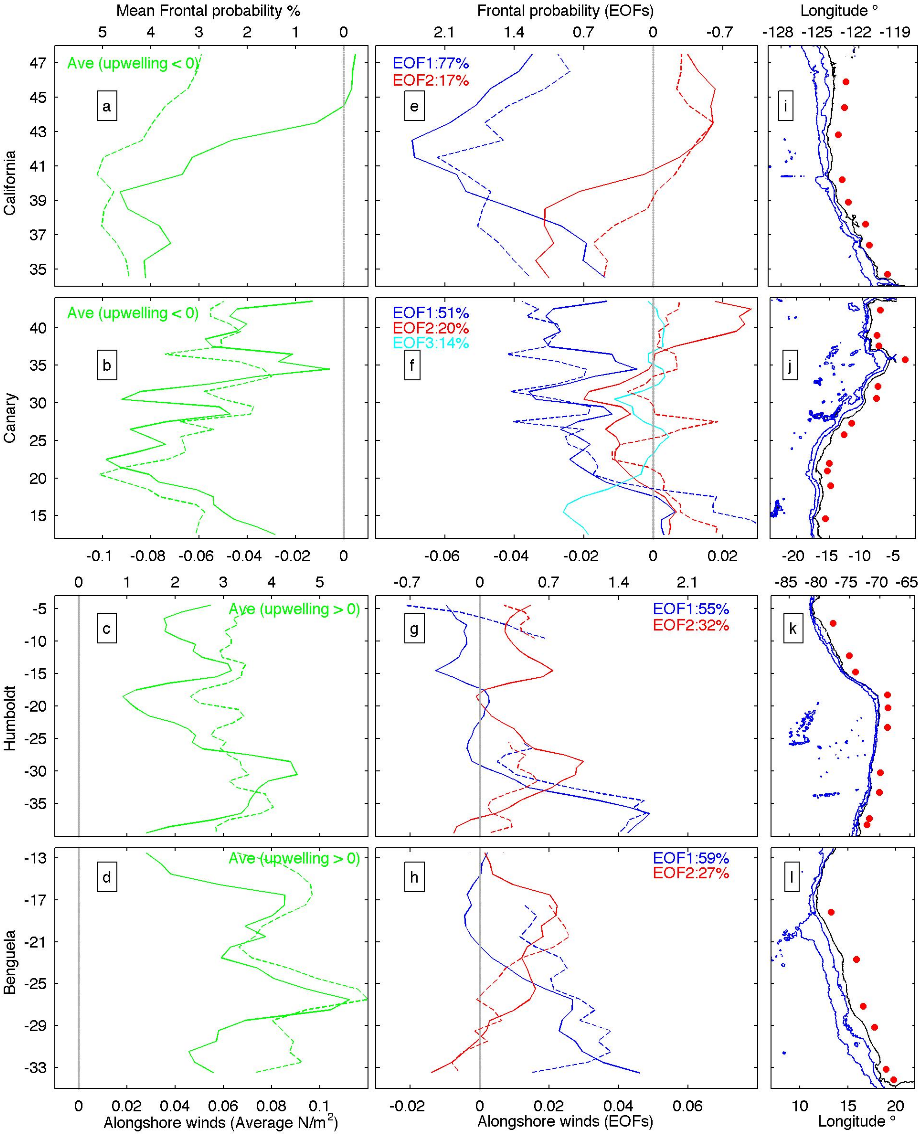

Figure 3.4 - Average and EOFs of coastal alongshore wind stress (solid lines) in the (a, e) California, (b, f) Canary, (c, g) Humboldt, and (d, h) Benguela Current Systems. Average and EOFs are shown using different colors according to the label in each panel. The percentages of total variance explained by each mode are also shown, color coded. The spatial averages of the mean and EOFs of frontal probability (dash lines) within 400km from the coast are shown as a function of latitude. Coastline for each region and location of major cities or capes are shown on right plots.

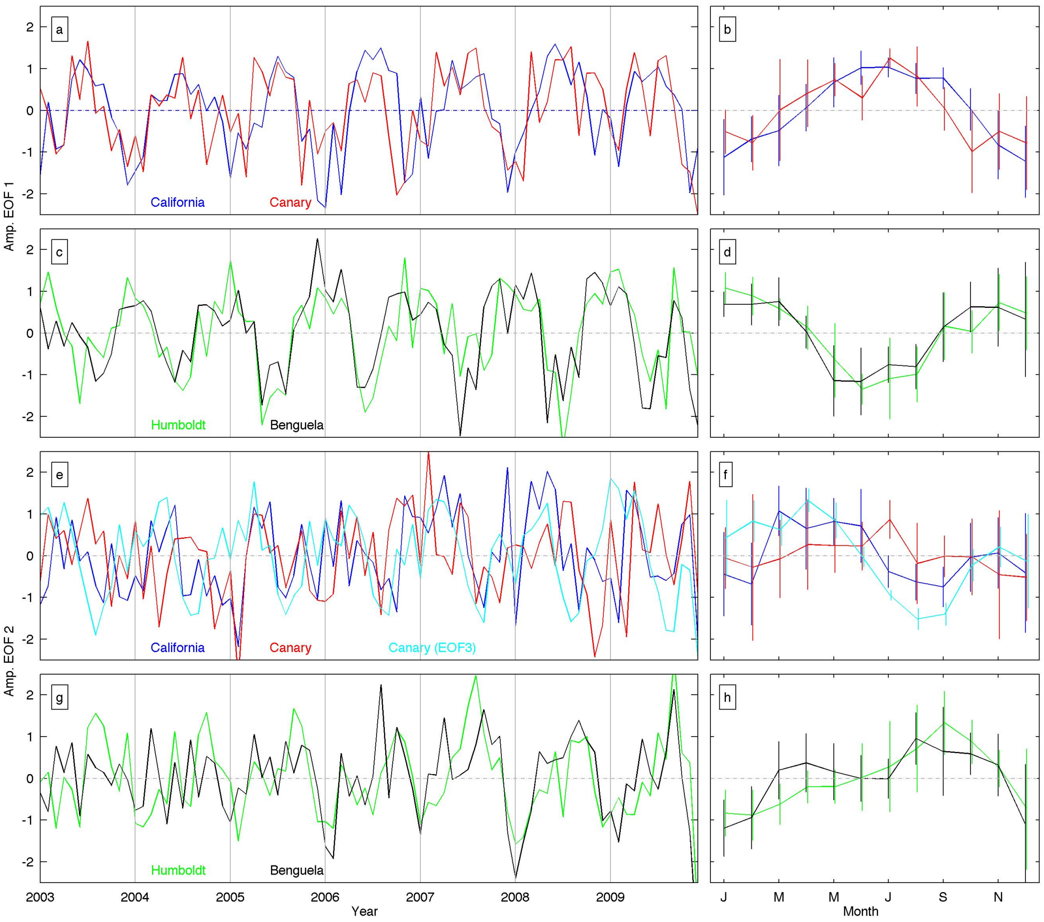

Figure 3.5 - Amplitude time series for EOFs 1 (a-d) and 2 (e-h) of coastal alongshore wind stress, color coded for the different EBCS. Values for each month are shown on the left plots, while right plots show the monthly averages ± standard deviation. Amplitude time series for EOF 3 of coastal alongshore wind stress for the Canary Current System is shown by cyan lines (e,f).

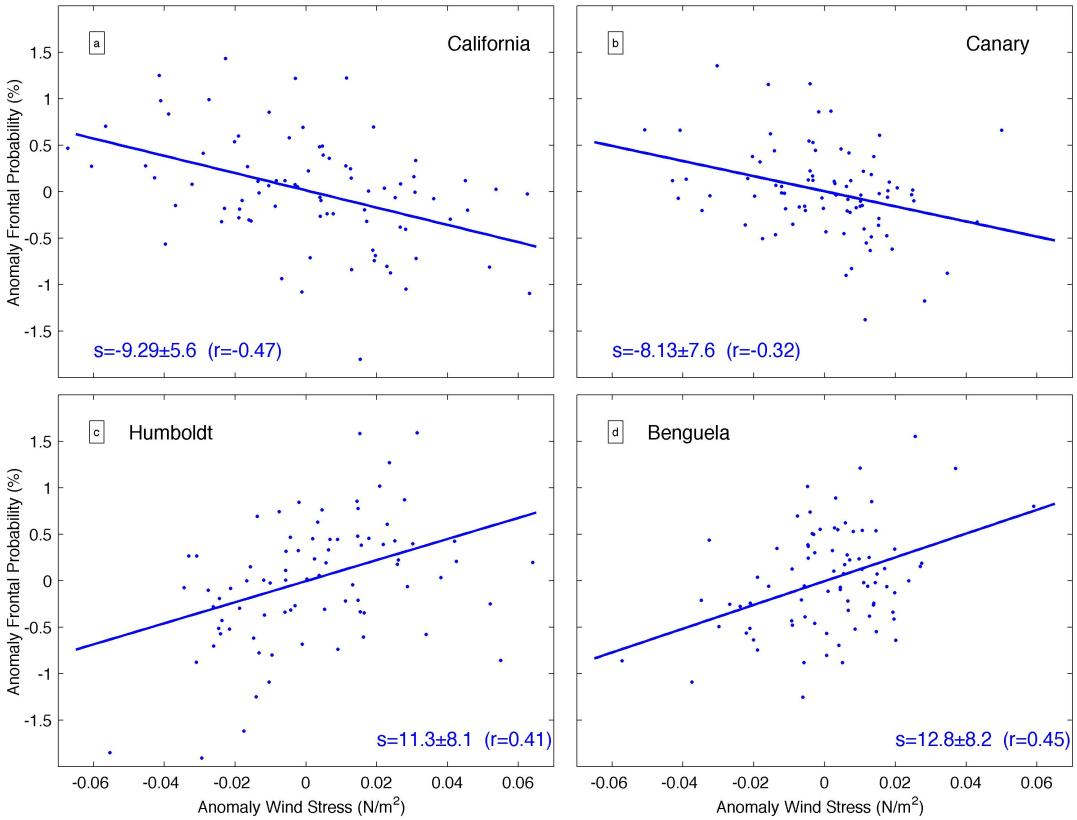

Figure 3.6 - Scatterplots of anomalies in the alongshore component of the wind stress and in frontal probabilities for the different EBCS. See text for definition of anomalies. Blue lines are linear fit to observations. The slope s of the regression and the correlation coefficient (r) are shown in each plot.

Table 3.1 - Summary of Major Characteristics in the Different EBCS

	California	Canary	Humboldt	Benguela
Meridional extent of region with high frontal probability variability (see Figure 2)	37~46°N	24~34°N	32~40°S	24~34S°
Shelf width [a]	26±13km	52±27km	22±14km	84±42km
Width of region with high mean frontal probability [a]	239±67km	115±34km	165±41km	211±56km
Width of region with high mean SST gradients [a]	211±50km	112±30km	137±32km	179±46km
Width of region with high frontal probability variability (based on EOF 1) [a]	304±77km	194±55km	223±46km	354±79km
Variance explained by EOFs (first/second)	11.9/2.8%	12.5/3.4%	9.3/3.3%	5.9/4.0%

[a] Values are calculated for each 1° latitude bin and then average ± standard deviation are computed over the area characterized by high frontal probability variability (given in the first row). Width of region with high frontal probability (or gradients) for each latitudinal bin is defined as the distance from the coast to the location where the smoothed probability decreases to 37% of the maximum values at the particular latitude, following *Castelao and Wang* [2014].

CHAPTER 4

VARIABILITY IN THE COUPLING BETWEEN SEA SURFACE TEMPERATURE AND WIND STRESS IN THE GLOBAL COASTAL OCEAN

Wang Y. and R. M. Castelao. Submitted to *Continental Shelf Research*, 12/15/15

4.1 Abstract

Mesoscale ocean-atmosphere interaction between sea surface temperature (SST) and wind stress throughout the global coastal ocean was investigated using 7 years of satellite observations. Coupling coefficients between crosswind SST gradients and wind stress curl and between downwind SST gradients and wind stress divergence were used to quantify spatial and temporal variability in the strength of the interaction. The use of a consistent data set and standardized methods allow for direct comparisons between coupling coefficients in the different coastal regions. The analysis reveals that strong coupling is observed in many mid-latitude regions throughout the world, especially in regions with strong fronts like Eastern and Western Boundary Currents. While most upwelling regions are characterized by strong seasonal variability in the strength of the coupling, intraseasonal variability is especially important in regions of strong eddy activity (e.g., Western Boundary Currents). Intraseasonal variability is particularly important for the coupling between crosswind SST gradients and wind stress curl. Results from the analysis can be used to guide modeling studies, since it allows for the *a priori* identification of regions in which regional models need to properly represent the ocean-atmosphere interaction to accurately represent local variability.

4.2 Introduction

Satellite observations have revealed that sea surface temperature (SST) can have a profound influence on wind stress variability throughout the world ocean wherever there are strong SST fronts (Chelton et al., 2004; Xie, 2004). As summarized by Chelton and Xie (2010), surface wind increases over warm water in association with decreased stability through enhanced vertical mixing that deepens the atmospheric boundary layer and draws momentum from the upper boundary layer down to the sea surface. Over cold water, by contrast, surface wind decreases in association with increased stability that decouples the surface winds from the stronger winds aloft. When winds blow along a SST front, higher winds over the warm side of the front and weaker winds over the cold side of the front generate wind stress curl. If the winds blow across a SST front, wind stress divergence is generated. The wind stress curl and divergence anomalies vary linearly with the crosswind and downwind components of the SST gradient, respectively (Chelton et al., 2001). This coupling between SST and winds has been widely observed, both in the open ocean (O’Neill et al., 2003; Chelton et al., 2004; O’Neill et al., 2005; 2010; among others) and in coastal regions (Chelton et al., 2007; Castelao, 2012; Desbiolles et al., 2014). Since wind stress curl anomalies drive Ekman pumping (e.g., Pickett and Paduan, 2003), they can be associated with significant upwelling or downwelling, with important implications for the marine ecosystem. They can also lead to modifications in the SST distribution itself (O’Neill et al., 2003).

The influence of SST on wind stress is clearer in regions with strong SST gradients (Haack et al., 2008). The interaction between SST and wind stress is often quantified by coupling coefficients, defined as the slope of the regression between crosswind SST gradients and wind stress curl and between downwind SST gradients and wind stress divergence (e.g., O'Neill et al., 2010). Spall (2007) noted that the coupling coefficient between wind stress and SST gradients has a significant quadratic dependence on the large-scale geostrophic wind speed. Large seasonal variability in front activity (e.g., Castelao and Wang, 2014) can lead to seasonal variations in the strength of the ocean-atmosphere interaction (Chelton et al., 2007). There is a general tendency for larger regression coefficients between downwind SST gradients and wind stress divergence compared to the coefficients between crosswind SST gradients and wind stress curl (Chelton et al., 2001; O'Neill et al., 2003; Seo et al., 2007). This is likely due to SST-induced wind direction gradient perturbations that enhance the divergence and reduce the curl response (O'Neill et al., 2010).

Despite the large number of studies investigating the coupling between SST and winds in the ocean, a systematic characterization of spatial and temporal variability in the strength of the coupling in coastal regions has not yet been done on a global scale. Studies have revealed large differences in the intensity of the coupling between different coastal regions (Chelton et al., 2007; Haack et al., 2008; Castelao, 2012; Desbiolles et al., 2014). However, it is not clear how much of these differences are due to actual variability in the strength of the coupling, and how much is due to methodological differences between the studies. Using multiple SST products, for example, with different resolutions and varying degrees of smoothing will result in different coupling coefficients (Castelao, 2012). Here, we use consistent satellite observations spanning seven years and standardized methods to investigate the ocean-atmosphere interaction in the coastal ocean on a global scale (Figure 4.1). Coefficients are computed on a monthly basis, and subsequently used to quantify spatial and temporal variability in the strength of the coupling.

4.3 Methods

Wind data were collected by the SeaWinds scatterometer on board the Quick Scatterometer (QuikSCAT) satellite. A detailed description of the measurements is given by Chelton and Freilich (2005). The QuikSCAT spatial resolution is roughly 25 km, and measurements within 30 km from the coast are contaminated by radar backscatter from land in the antenna side lobes. Observations are available from July 1999 to Nov 2009. Regions farther than 800 km from the coast are discarded in this study. Sea surface temperature (SST) data were obtained by the Moderate-resolution Imaging Spectroradiometer (MODIS). Daily observations are available at 5-km resolution since August 2002. Measurements within 5 km from land or from pixels flagged as clouds were discarded to avoid contamination.

Here, we focus on the period from Nov 5, 2002 to Nov 4, 2009, when both observations of wind and SST are available simultaneously. All observations were time-averaged as in Chelton et al. (2007). Specifically, SST measurements were first averaged in overlapping 3-day periods at daily intervals. The crosswind and downwind components of the SST gradient was computed within each QuikSCAT measurement from the instantaneous wind stress field and the 3-day-averaged SST field centered on the date of the QuikSCAT observations. Crosswind SST gradients are defined as the cross product $\nabla SST \times \hat{\tau}$, where $\nabla = i\partial/\partial x + j\partial/\partial y$ is the two-dimensional gradient operator in Cartesian coordinates with unit vectors i and j in the zonal and meridional directions, respectively and $\hat{\tau}$ is a unit vector in the direction of the wind stress. SST, crosswind and downwind SST gradients, wind stress, wind stress curl and divergence were then averaged in 29-day periods at 7-day intervals. Anomalies for each variable were calculated as the deviation of each 29-day average from the respective seasonal average. All observations were averaged onto a 0.25° latitude by 0.25° longitude grid.

Coastal regions along the entire globe were divided into 192 regions, with each region spanning approximately 500 km along the coastline. Regions to the north of 65°N and to the south of 65°S were not considered. For each region, the 29-day averages at 7-day intervals were used to compute the coupling coefficients for each calendar month. The coupling coefficients are the slopes of the linear regressions between crosswind SST gradient (CWSG) and wind stress curl (WSC) and between the downwind SST gradient (DWSG) and wind stress divergence (WSG) (Figure 4.2). These resulted in time series of coupling coefficients for each region spanning 84 months (7 years). Those time series were then used to calculate the corresponding mean and seasonal cycles. In order to quantify interannual, seasonal and intraseasonal variability, the monthly time series were first low-pass filtered using a 12-month filter to separate interannual variability (Figure 4.3), following Legaard and Thomas (2006). The differences between the original and the low-pass filtered time series correspond to variability at seasonal or higher frequencies. We further applied a 6-month low-pass filter to the difference time series to isolate the seasonal signal. The residual time series after the removal of interannual and seasonal signals capture intraseasonal variability (Figure 4.3). For each region, the total variance of the time series of the coupling coefficients was approximated as the sum of the variance of the time series of interannual, seasonal and intraseasonal variability (Legaard and Thomas, 2007). The error due to the assumption is generally less than 14%.

4.4 Results

4.4.1 Correlations between SST gradients and wind variables

Correlation coefficients between crosswind SST gradients (CWSG) and wind stress curl (WSC) and between downwind SST gradients (DWSG) and wind stress divergence (WSD) during local summer (January to March in southern hemisphere, July to September in northern hemisphere) are shown in Figure 4.1, revealing the regions in the coastal ocean where variability in SST gradients and wind variables are tightly coupled. The correlations between CWSG and WSC and between DWSG and WSD have a similar spatial distribution, although correlation coefficients between DWSG and WSD are substantially larger. Strongest correlations are generally associated with regions known to be characterized by strong fronts (e.g., Western Boundary Currents - WBC).

In all Eastern Boundary Currents Systems (EBCS), which are regions characterized by strong upwelling, correlations are generally strongest near the coast, decreasing offshore. The area with intensified correlations often extends for a few hundred kilometers from the coast. The strongest correlation between CWSG and WSC is observed in the California Current System, while the northern sector of the Humboldt Current System presents the largest correlation between DWSG and WSD of all EBCS. It is interesting to note that there are two separated bands with strong correlations in the Humboldt Current System, one off Peru and one off central Chile. Correlations for both curl and divergence fields are significantly stronger off Peru than off Chile. The offshore extent of the region with strong correlations is considerably narrower in the Canary Current System than in the other EBCS. This is consistent with the Canary being characterized by a relatively narrower band of high frontal activity (Wang et al., 2015).

In WBCs (e.g., Gulf Stream, Brazil-Malvinas Confluence), strong correlations extend much farther offshore, often all the way to (and presumably beyond) the boundary of our study region (O'Neill et al., 2012). Correlations are also high at the Arabian Peninsula and off Western Australia.

4.4.2 Average and seasonal cycles of coupling coefficients

The response of wind variables to SST gradient perturbations was quantified by the slope of the linear regression between CWSG and WSC and between DWSG and WSD (Figure 4.2; Chelton et al., 2007; O'Neill et al., 2010). The regressions were computed for all coastal regions for each month, yielding 192 time series of coupling coefficients (one for each region) spanning 7 years (see top panel of Figure 4.3 for an example). The time series were then used to compute the overall mean and the amplitude and phase of the seasonal cycle for each region (Figure 4.4).

Strong mean coupling coefficients for both curl and divergence fields are observed in all EBCS, the Brazil-Malvinas Confluence, the Agulhas Current, off Australia (expect for its northern coast) and the Arabian Peninsula (Figure 4.4a,d). High latitude regions are generally characterized by weak coupling coefficients. For most regions, the average coupling coefficient is larger for the divergence field compared to the curl field. In general, there is a good agreement between the regions with high correlation coefficients (Figure 4.1) and the regions with large mean coupling coefficients (Figure 4.4a,d).

The amplitudes of the seasonal cycle of the coupling coefficients reveal that regions with large means (Figure 4.4a,d) are usually associated with strong seasonal cycles (Figure 4.4b,e). EBCS, in particular, are characterized by large amplitudes of the seasonal cycle for both curl and divergence fields. Although the largest mean coupling coefficients in EBCS are observed in the Benguela Current System, the strongest seasonal cycles are observed in the Canary and northern Humboldt Current System off Peru. Indeed, the largest amplitude of the seasonal cycle in the Humboldt Current System is observed off Peru, even though the average coupling coefficients are larger farther south, off Chile. The largest overall amplitudes are observed in the Arabian Peninsula for both curl and divergence fields, however, exceeding other regions by at least 60% for curl field. Consistently with the pattern observed for the mean field, there is a general tendency for the amplitude of the seasonal cycle of the coupling coefficients for the divergence field to be larger compared to the curl field. This is especially true in the Eastern Tropic Pacific and off Peru, where the amplitude of the seasonal cycle for the divergence field is substantially larger than the amplitude for the curl. An exception for that pattern is the Mozambique Channel (see discussion below).

The phases of the seasonal cycle reveal that the seasonal enhancement of coupling coefficients at mid-latitudes peaks during summer (July in northern hemisphere and January in southern hemisphere; Figure 4.4c,f). Interestingly, the phase in the northern hemisphere at low latitudes in EBCS is remarkably different, indicating that the seasonal enhancement peaks in local winter or spring. That transition occurs at approximately 30°N in the California Current System and at 20°N at the Canary Current System. An abrupt phase shift in the evolution of frontal activity has been previously observed in the Canary Current System, with front activity peaking during summer to the north of Cape Blanc (20°N), and from late fall to early spring to the south of the Cape (Wang et al., 2015). The phase shift in frontal activity is likely associated with differences in wind forcing (Nykjær and Van Camp, 1994) and possibly due to the influence of the Mauritania Current (Peña-Izquierdo et al., 2012). Abrupt latitudinal shifts in phase are not observed in the EBCS in the southern hemisphere. In those areas, the peak in the seasonal cycle occurs in summer to early fall. Off the Arabian Peninsula, the seasonal cycles peak in early summer when the southwest monsoon is more prominent (Schott and McCreary, 2001). Similarly to EBCS, WBCs are also characterized by large average coefficients, although the amplitudes of the seasonal cycles are comparatively smaller.

4.4.3 Variability in coupling coefficients at multiple frequency bands

Some of the regions characterized by small amplitudes of the seasonal cycle of coupling coefficients are dominated by variability at other frequency bands. To quantify that, monthly time series of coupling coefficients were sequentially filtered to isolate interannual (>12 months), seasonal (between 6 and 12 months) and intraseasonal (< 6 months) variability (Figure 4.3). The fraction of the total variance explained by each frequency band is shown in Figure 4.5. Note that different color scales are used for different frequency bands to reveal as much as possible of the spatial structure.

Seasonal variability is the dominant signal in most regions, constituting up to 70-80% of the variance of the total signal (Figure 4.5b,e). Seasonal variability is important even for regions where seasonal signals are comparatively smaller, representing at least 30% of the total variance. As expected, regions with strong seasonal variability are consistent with the regions previously identified as characterized by large amplitudes of the seasonal cycle. Variability on seasonal scales is more important for the coupling between DWSG and WSD than for the coupling between CWSG and WSC.

Variability at intraseasonal scales is another important component of the total variability (Figure 4.5c,f). This is especially true at high latitudes in the northern hemisphere and southeastern Asia, which are regions characterized by weak seasonal variability and by weak seasonal cycles (see Figure 4.4). Relatively large intraseasonal variability is also observed in the Canary Current System and off Chile. At the Brazil-Malvinas Confluence, the Gulf Stream, the Kuroshio Current, the Agulhas Current and the East Australian Current, intraseasonal variability is comparable to variability at seasonal scales, especially for the curl field. The southern Benguela Current System and the Agulhas Current region have been shown to be characterized by enhanced intraseasonal variability in sea surface height due to the impact of eddy activity (Chavez and Messié, 2009). High eddy activity has also been detected in the other WBCs, including the Gulf Stream (e.g., Kang and Curchitser, 2013), the Kuroshio Current (Yang et al., 2013); the Brazil-Malvinas Confluence (e.g., Goni et al., 1996) and the East Australian Current (e.g., Bowen et al., 2005). Since eddies are known to play an important frontogenetic role (Fedorov, 1986), it is possible that they influence the strength of the coupling at intraseasonal scales at those regions characterized by high eddy activity. Unlike seasonal variability, which was more important for the divergence field, there is a clear pattern of intraseasonal variability being more important for the curl field.

After seasonal and intraseasonal signals are removed, the remaining variability occurs on an interannual scale (Figure 4.5a,d). The variance explained by interannual variability is generally small, always less than 35%. Values around 30% for the coupling between CWSG and WSG are only observed in the Brazil Malvinas Confluence, South Atlantic Bight, off western British Isles and off western Canada. Strong interannual variability in the coupling between DWSG and WSD is found in the Brazil Malvinas Confluence, the Benguela and northern Canary Current Systems, the Agulhas Current, off Australia and in the Kuroshio Current.

4.5 Discussion

Analyses of mesoscale ocean-atmosphere interactions around the global coastal ocean revealed substantial spatial and temporal variability in the strength to the coupling between the anomalies of crosswind SST gradients (CWSD) and wind stress curl (WSC) and between downwind SST gradients (DWSG) and wind stress divergence (WSD) (Figures 4.1 and 4.4). A clear pattern of stronger coupling at mid-latitudes emerges, with the largest mean coupling coefficients for both curl and divergence fields centered at about 35°N and 35°S (Figure 4.6). Mean coefficients are progressively reduced toward low or high latitudes, creating an M-shape in the meridional distribution of coupling coefficients (Figure 4.6). The ocean-atmosphere interaction investigated here is more prominent in regions characterized by large SST gradients (Haack et al., 2008) and with strong (Spall, 2007; O'Neill et al., 2010) wind stress. As such, strong coupling being observed in mid-latitudes (Figure 4.6) is consistent with those areas being characterized by strong SST gradients and wind stress (O'Neill et al., 2012; Wang et al., 2015), especially along Eastern and Western Boundary Currents (O'Neill et al., 2003; Maloney and Chelton, 2006; Chelton et al., 2007; Spall, 2007; Haack et al., 2008; among others). SST gradients are generally reduced at high latitudes and around the tropics (O'Neill et al., 2010; O'Neill et al., 2012), which presumably leads to weaker coupling. Coupling coefficients at mid-latitudes in the coastal ocean are slightly larger in the southern hemisphere than in the northern hemisphere (Figure 4.6), indicating that the strength of the ocean-atmosphere is larger in the southern hemisphere (O'Neill et al., 2012). Coupling coefficients are also consistently larger for the divergence field compared to the curl field (Figure 4.6; Chelton et al., 2001; O'Neill et al., 2003; Seo et al., 2007; Haack et al., 2008; Chelton and Xie, 2010; O'Neil et al., 2012), since SST-induced wind direction gradient perturbations enhance the divergence and reduce the curl response (O'Neill et al., 2010).

Regions known to be characterized by high mesoscale activity were found to be also characterized by strong ocean-atmosphere interactions. In Eastern Boundary Current Systems (EBCS), for example, upwelling favorable winds and the presence of a strong upwelling jet (Huyer, 1983; Kosro and Huyer, 1986; Hickey, 1989) that often becomes unstable (Barth, 1989a,b; Haidvogel et al., 1991) and interacts with complex topography (Arthur, 1965; Narimousa and Maxworthy, 1989; Swenson et al., 1992; Batteen, 1997; Barth et al., 2000; Haney et al., 2001) are favorable for the development of strong fronts

(Castelao et al., 2005, 2006; Kahru et al., 2012; Nieto et al., 2012; Castelao and Wang, 2014; Wang et al., 2015) and high mesoscale activity (Strub and James, 2000). Strong wind stress curl (Bakun and Nelson, 1991; Pickett and Paduan, 2003) also creates favorable conditions for formation of fronts (Bakun and Nelson, 1977). Regions in EBCS where strong coupling has been identified (Figures 4.1 and 4.4) are consistent with regions previously identified as having strong and persistent front activity (Wang et al., 2015). The Benguela Current System, for example, has the strongest average coupling coefficients of all EBCS (Figure 4.4) and also the highest average frontal activity (Wang et al., 2015). There is also a phase shift in wind pattern in EBCS, with stronger upwelling favorable winds being observed during summer at mid-latitudes (*Strub et al., 2013; Wang et al., 2015*) and during winter at low latitudes (*Nykjær and Camp*, 1994; *Lathuiliere et al.,* 2008; *Risien and Chelton, 2008; Hutchings et al.,* 2009; *Strub et al., 2013; Wang et al., 2015*). Consistently, a shift in the phase of the seasonal cycle of coupling coefficients is also observed between mid and low latitudes (Figure 4.4), especially in the northern hemisphere, revealing stronger coupling during summer at mid latitudes and during winter/early spring at low latitudes. Although upwelling favorable winds at the low latitude northern Humboldt Current System are stronger during winter (Echevin et al., 2008), higher SST frontal activity (Wang et al., 2015) and stronger coupling coefficients are actually observed in summer (Figure 4.4c, f). The paradox is also observed for chlorophyll concentrations (Chavez and Messié, 2009), which are low when seasonal upwelling winds are strong, and high when seasonal upwelling winds are weak. The reasons for these responses are currently not understood.

Similarly to EBCS, WBCs are also characterized by high mean coupling coefficients. The amplitude of the seasonal cycle is comparatively smaller, however (Figure 4.4). Strong seasonal variability in coupling coefficients in WBCs has been previously observed (O'Neill et al., 2012). Coupling between wind stress and SST gradients has been shown to be enhanced during winter in the Kuroshio Current (Maloney and Chelton, 2006), for example. This inconsistency may be at least partially due to the different regions analyzed in the studies. While here the focus was in the area near the coast, those previous studies focused on a much larger region, fully capturing the area of high mesoscale activity extending for thousands of kilometers from shore after the boundary current separates from the coast. Other sources of differences may be related to the SST fields used (e.g., different spatial resolution, which may allow for capturing the wind response to SST perturbations at different scales; O'Neill et al., 2012).

Strong mean and seasonally-varying coupling is also observed off the Arabian Peninsula (Figure 4.4). The region is dominated by the southwest monsoon during summer and by the northeast monsoon in winter (Izumo et al., 2008). The strongest ocean-atmosphere interaction (i.e., the largest coupling coefficients) in that area occurs during summer, when northeastward, upwelling favorable winds are strong (Bruce et al., 1994). During that time, SST gradients can exceed 2.5°C per 100 km (Vecchi et al., 2004), allowing for strong coupling between SST gradients and wind variables. During the winter monsoon, downwelling favorable winds dominate (Hastenrath and Greischar, 1991), leading to weak coupling (Figure 4.4).

Although variability in coupling coefficients at seasonal scales is clearly dominant, intraseasonal variability also plays an important role in multiple locations (Figure 4.5). Several of those regions are characterized by high eddy activity. Eddies can have strong influence on ocean-atmosphere interactions (e.g., Frenger et. al., 2013; Chelton, 2013) because of substantial differences in water characteristics in their interior (Joyce, 1984). Eddy activity off the coast of Chile is considerably larger than off the coast of Peru (Chaigneau et al., 2009), for example. Consistently, strong intraseasonal variability in the strength of the ocean-atmosphere interaction is observed off Chile, together with comparatively weaker seasonal cycle. Strong intraseasonal variability is also observed in the Benguela Current System (especially for curl field), a region also characterized by high intraseasonal variability in sea surface height because of the influence of eddies from the Agulhas Current (Chavez and Messié, 2009). WBCs in general also present strong intraseasonal variability in coupling coefficients, often as large as variability at seasonal scales (Figure 4.5). At the Brazil-Malvinas Confluence, and the Agulhas and Kuroshio Currents, interannual variability in the strength of the coupling is also enhanced compared to other regions. It is important to emphasize that because of data availability constraints, only 7 years of observations were used in the analyses. As longer time series become available, additional insights into interannual variability in the strength of the coupling can be obtained.

An interesting aspect of the analysis is the identification of a few regions of negative mean coupling coefficients for CWSG and WSC (Figure 4.6), for example the eastern tropical Pacific (Figure 4.4a). In that region, strong wind jets through mountain gaps in Central America are frequent (Chelton et al., 2000), resulting in positive wind stress curl to the left and in negative wind stress curl to the right of the wind center throughout the year (Chelton et al., 2004). As summarized by Liang et al. (2009), the region is characterized by a shallow surface mixed layer, so that wind-driven mixing conveys subsurface cooler water to the surface. During strong wind events, this cooling process presumably becomes dominant, masking out the signature of the ocean-atmosphere interaction (Liang et al., 2009). This is consistent with O'Neill et al. (2012), who found that the ocean-atmosphere coupling is not significant in that region because of topographic effects. Negative coupling coefficients are also observed to the northwest of Madagascar Island (Figure 4.4a). In that region, wind stress curl variability is strongly modulated by topographic effects, since the northernmost tip of Madagascar Island acts as a barrier (Schott and McCreary, 2001) to the persistent southeasterly trade winds (Chen et al., 2014), leading to the generation of positive wind stress curl (Chelton et al., 2004). Wind stress curl is more predominant during local winter, when the southeasterly trade wind moves northward (Schott and McCreary, 2001). At that time, water at the lee of the Island is often warmer, possibly associated with anticyclonic motion of the Northeast Madagascar Current (Chen et al., 2014). Together, these result in weaker winds blowing over warm water, and stronger winds blowing over cold water, leading to negative coupling coefficients for the curl field.

4.6 Summary and conclusions

High-resolution satellite observations of SST and wind stress spanning a 7-year period were used to investigate spatial and temporal variability in the strength of ocean-atmosphere interactions in the global coastal ocean. The strength of the interaction was quantified by coupling coefficients, defined as the slope of the linear regression between anomalies in the crosswind SST gradients and wind stress curl and between downwind SST gradients and wind stress divergence. Strong coupling was identified in several regions, especially along Eastern Boundary Current Systems, in Western Boundary Currents, off the Arabian Peninsula and off Western Australia. There is a general tendency for strong coupling to be observed in regions previously characterized by strong wind forcing and strong front activity, especially at mid-latitudes. Although seasonal variability is dominant, especially in upwelling regions and off the Arabian Peninsula, intraseasonal variability in the strength of the coupling is also important in regions of strong eddy activity. This is especially apparent in Western Boundary Currents, where intraseasonal variability seems to be as important as variability at seasonal scales. Intraseasonal variability is particularly important for the coupling between crosswind SST gradients and wind stress curl.

Although many previous studies have investigated the ocean-atmosphere interaction in the coastal ocean, comparing the strength and variability in the coupling between different regions is difficult. This is because the methods used in those studies are not standardized. As such, variability in coupling coefficients could be related to actual variability in the strength of the coupling, but also to the use of different SST products with different resolution, different study periods, etc. Here, those differences have been eliminated by the use of a consistent data set, providing an atlas of temporal and spatial variability in the strength of the ocean-atmosphere interaction in coastal regions on a global scale. This atlas can be particularly useful to guide modeling studies, as it allows for the *a priori* identification of locations and time periods (e.g., seasons) in which regional models need to properly represent the ocean-atmosphere interaction, either as a parameterization or via the use of a fully coupled ocean-atmosphere model.

4.7 Acknowledgments

We gratefully acknowledge support by NASA's Ocean Vector Wind Science Team (grant NNX14AM70G).

Reference

Aguirre, C., Pizarro Ó., Strub P. T., Garreaud R., and Barth J. A., 2012. Seasonal dynamics of the near-surface alongshore flow off central Chile, J. Geophys. Res., 117, C01006, doi:10.1029/2011JC007379.

Arthur, R.S., 1965. On the calculation of vertical motion in Eastern boundary currents from determination of horizontal motion. J. Geophys. Res., 70, 2799-2803.

Bakun, A., and Nelson C. S., 1977. Climatology of upwelling related processes off Baja California, Calif. Coop. Fish. Invest., Rep. XIX, 107 – 127.

Bakun, A., and Nelson C. S., 1991. The seasonal cycle of wind-stress curl in subtropical eastern boundary current regions, J. Phys. Oceanogr., 21, 1815–1834, doi: http://dx.doi.org/10.1175/1520-0485(1991)021<1815:TSCOWS>2.0.CO;2

Barth, J. A., 1989a. Stability of a coastal upwelling front: 1. Model development and a stability theorem, J. Geophys. Res., 94(C8), 10844–10856, doi:10.1029/JC094iC08p10844.

Barth, J. A., 1989b. Stability of a coastal upwelling front: 2. Model results and comparison with observations, J. Geophys. Res., 94(C8), 10857–10883, doi:10.1029/JC094iC08p10857.

Barth, J. A., Pierce S. D., and Smith R. L., 2000. A separating coastal upwelling jet at Cape Blanco, Oregon and its connection to the California Current System, Deep Sea Res., Part II, 47(5–6), 783–810, doi:10.1016/S0967-0645(99)00127-7.

Batteen, M. L., 1997. Wind-forced modeling studies of currents, meanders, and eddies in the California Current System, J. Geophys. Res., 102(C1), 985 – 1010.

Bowen, M. M., Wilkin J. L. and Emery W. J., 2005. Variability and forcing of the East Australian Current, J. Geophys. Res., 110, C03019, doi:10.1029/2004JC002533.

Bruce, J. G., Johnson D. R., and Kindle J. C., 1994. Evidence for eddy formation in the eastern Arabian Sea during the northeast monsoon, J. Geophys. Res., 99(C4), 7651–7664, doi:10.1029/94JC00035.

Castelao, R. M., 2012. Sea surface temperature and wind stress curl variability near a cape, J. Phys. Oceanogr., 42(11), 2073-2087.

Castelao, R. M., Barth J. A., and Mavor T. P., 2005. Flow-topography interactions in the northern California Current System observed from geostationary satellite data, Geophys. Res. Lett., 32, L24612, doi:10.1029/2005GL024401.

Castelao, R. M., Mavor T. P., Barth J. A., and Breaker L. C., 2006. Sea surface temperature fronts in the California Current System from geostationary satellite observations, J. Geophys. Res., 111, C09026, doi:10.1029/2006JC003541.

Castelao, R. M., and Wang Y., 2014. Wind-driven variability in sea surface temperature front distribution in the California Current System, J. Geophys. Res. Oceans, 119, 1861–1875, doi:10.1002/2013JC009531.

Chaigneau, A., Eldin G., and Dewitte B., 2009. Eddy activity in the four major upwelling systems from satellite altimetry (1992–2007), Prog. Oceanogr., 83(1-4), 117-123, doi: http://dx.doi.org/10.1016/j.pocean.2009.07.012.

Chavez, F. P., and Messié M., 2009. A comparison of eastern boundary upwelling ecosystems, Prog. Oceanogr., 83(1-4), 80-96, doi: http://dx.doi.org/10.1016/j.pocean.2009.07.032.

Chelton, D. B., 2013. Ocean-atmosphere coupling: Mesoscale eddy effects, Nat. Geosci., 6(8), 594–595, doi:10.1038/ngeo1906.

Chelton, D. B., and Freilich M. H., 2005. Scatterometer-based assessment of 10-m wind analyses from the operational ECMWF and NCEP numerical weather prediction models, Mon. Wea. Rev., 133(2), 409–429, doi: http://dx.doi.org/10.1175/MWR-2861.1

Chelton, D.B., and Xie S.-P., 2010. Coupled ocean-atmosphere interaction at oceanic mesoscales. Oceanography 23(4):52–69, doi:10.5670/oceanog.2010.05.

Chelton, D.B., Freilich M. H., and Esbensen S. K., 2000. Satellite observations of the wind jets off the Pacific coast of Central America. Part II: Regional relationships and Dynamical Considerations, Mon. Wea. Rev. 128, 2019-2043.

Chelton, D. B., Schlax M. G., and Samelson R. M., 2007. Summertime coupling between sea surface temperature and wind stress in the California Current System, J. Phys. Oceanogr., 37(3), 495-517.

Chelton, D. B., Schlax M. G., Freilich M. H., and Milliff R. F., 2004. Satellite measurements reveal persistent small-scale features in ocean winds, Science, 303(5660), 978-983.

Chelton, D. B., Esbensen S. K., Schlax M. G., Thum N., Freilich M. H., Wentz F. J., Gentemann C. L., McPhaden M. J., and Schopf P. S., 2001. Observations of coupling between surface wind stress and sea surface temperature in the eastern tropical Pacific, J. Climate, 14(7), 1479-1498.

Chen, Z., Wu L., Qiu B., Sun S., and Jia F., 2014. Seasonal variation of the south equatorial current bifurcation off Madagascar, J. Phys. Oceanogr., 44, 618–631.

Desbiolles, F., Blanke B., Bentamy A., and Grima N., 2014. Origin of fine-scale wind stress curl structures in the Benguela and Canary upwelling systems, J. Geophys. Res. Oceans, 119,7931–7948, doi:10.1002/2014JC010015.

Echevin, V., Aumont O., Ledesma J., and Flores G., 2008. The seasonal cycle of surface chlorophyll in the Peruvian upwelling system: A modeling study, Prog. Oceanogr., 79,167–176.

Fedorov K.N., 1986. The Physical Nature and Structure of Oceanic Fronts. Springer-Verlag, Berlin etc., viii+333 pp.

Frenger, I., Gruber N., Knutti R., and Münnich M., 2013. Imprint of Southern Ocean eddies on winds, clouds and rainfall, Nat. Geosci., 6(8), 608–612, doi:10.1038/ngeo1863.

Goni, G. J., S. Kamholtz, S. Garzoli, and D. B. Olson, 1996: Dynamics of the Brazil–Malvinas confluence based upon inverted echo sounders and altimetry. J. Geophys. Res., 101 (7), 16 273– 16 289.

Haack, T., Chelton D., Pullen J., Doyle J. D., and Schlax M., 2008. Summertime Influence of SST on Surface Wind Stress off the US West Coast from the US Navy COAMPS Model, J. Phys. Oceanogr., 38(11), 2414-2437.

Haidvogel, D. B., Beckman A., and Hedstrom K., 1991. Dynamical simulation of filament formation and evolution in the coastal transition zone, J. Geophys. Res., 96, 15,017 – 15,040.

Haney, R. L., Hale R. A., and Dietrich D. E., 2001. Offshore propatation of eddy kinetic energy in the California Current, J. Geophys. Res., 106(C6), 11,709 – 11,717.

Hastenrath, S., and Greischar L., 1991. The monsoonal current regimes of the tropical Indian Ocean: Observed surface flow fields and their geostrophic and wind-driven components, J. Geophys. Res., 96(C7), 12619–12633, doi:10.1029/91JC00997.

Hickey, B. M., 1989. Patterns and processes of circulation over the shelf and slope, in Coastal Oceanography of Washington and Oregon, edited by M. R. Landry and B. M. Hickey, pp. 41 – 109, Elsevier, New York.

Hutchings, L., et al., 2009. The Benguela Current: An ecosystem of four components, Prog. Oceanogr., 83(1-4), 15-32, doi: http://dx.doi.org/10.1016/j.pocean.2009.07.046

Huyer, A., 1983. Coastal upwelling in the California current system, Prog Oceanogr, 12 (3), 259-284.

Izumo T., Montégut C. B., Luo J.-J., Behera S. K., Masson S., and Yamagata T., 2008. The Role of the Western Arabian Sea Upwelling in Indian Monsoon Rainfall Variability. J. Climate, 21, 5603–5623. doi: http://dx.doi.org/10.1175/2008JCLI2158.1

Joyce, T. M., 1984. Velocity and hydrographic structure of a Gulf Stream warm core ring, J. Phys. Oceanogr., 14, 936–947, doi:10.1175/1520-

0485(1984)014<0936:VAHSOA>2.0.CO;2.

Kahru, M., Di Lorenzo, E., Manzano-Sarabia, M., and Mitchell, B., 2012. Spatial and temporal statistics of sea surface temperature and chlorophyll fronts in the California Current, J. Plankton Res., 34, 749–760.

Kang, D., and Curchitser E. N., 2013. Gulf Stream eddy characteristics in a high-resolution ocean model, J. Geophys. Res. Oceans, 118,4474–4487, doi:10.1002/jgrc.20318.

Kosro, P. M., and Huyer A., 1986. CTD and velocity surveys of seaward jets off northern California, July 1981 and 1982, J. Geophys. Res., 91, 7680 – 7690.

Lathuilière, C., Echevin V., and Lévy M., 2008. Seasonal and intraseasonal surface chlorophyll-a variability along the northwest African coast, J. Geophys. Res., 113, C05007, doi:10.1029/2007JC004433.

Legaard, K. L., and Thomas A. C., 2006. Spatial patterns in seasonal and interannual variability of chlorophyll and sea surface temperature in the California Current, J. Geophys. Res., 111, C06032, doi:10.1029/ 2005JC003282.

Legaard, K. R., and Thomas A. C., 2007. Spatial patterns of intraseasonal variability of chlorophyll and sea surface temperature in the California Current, J. Geophys. Res., 112, C09006, doi:10.1029/2007JC004097.

Liang, J.-H., McWilliams J. C., and Gruber N., 2009. High-frequency response of the ocean to mountain gap winds in the northeastern tropical Pacific, J. Geophys. Res., 114, C12005, doi:10.1029/2009JC005370.

Maloney, E. D. and Chelton D. B., 2006. An Assessment of the Sea Surface Temperature Influence on Surface Wind Stress in Numerical Weather Prediction and Climate Models. J. Climate, 19, 2743–2762. doi: http://dx.doi.org/10.1175/JCLI3728.1.

Mizuno K. and White W. B., 1983. Annual and Interannual Variability in the Kuroshio Current System. J. Phys. Oceanogr., 13, 1847–1867. doi: http://dx.doi.org/10.1175/1520-0485(1983)013<1847:AAIVIT>2.0.CO;2

Narimousa, S., and Maxworthy T., 1989. Application of a laboratory model to the interpretation of satellite and field observations of coastal upwelling, Dyn. Atmos. Oceans, 13, 1 – 46.

Nieto, K., Demarcq H., and McClatchie S., 2012. Mesoscale frontal structures in the Canary Upwelling System: New front and filament detection algorithms applied to spatial and temporal patterns, Remote Sens. Environ., 123, 339-346, doi: http://dx.doi.org/10.1016/j.rse.2012.03.028.

Nykjær, L., and Van Camp L., 1994. Seasonal and interannual variability of coastal upwelling along northwest Africa and Portugal from 1981 to 1991, J. Geophys. Res., 99(C7), 14197–14207, doi:10.1029/94JC00814.

O’Neill, L. W., Chelton D. B. and Esbensen S. K., 2003. Observations of SST-Induced Perturbations of the Wind Stress Field over the Southern Ocean on Seasonal Timescales. J. Climate, 16, 2340–2354. doi: http://dx.doi.org/10.1175/2780.1

O’Neill, L. W., Chelton D. B. and Esbensen S. K., 2010. The Effects of SST-Induced Surface Wind Speed and Direction Gradients on Midlatitude Surface Vorticity and

Divergence. J. Climate, 23, 255–281. doi: http://dx.doi.org/10.1175/2009JCLI2613.1

O'Neill, L. W., Chelton D. B., Esbensen S. K. and Wentz F. J., 2005. High-Resolution Satellite Measurements of the Atmospheric Boundary Layer Response to SST Variations along the Agulhas Return Current. J. Climate, 18, 2706–2723. doi: http://dx.doi.org/10.1175/JCLI3415.1

O'Neill, L. W., Chelton D. B. and Esbensen S. K., 2012. Covariability of Surface Wind and Stress Responses to Sea Surface Temperature Fronts. J. Climate, 25, 5916–5942.

Peña-Izquierdo, J., Pelegrí J., Pastor M., Castellanos P., Emelianov M., Gasser M., Salvador J., and Vázquez-Domínguez E., 2012. The continental slope current system between Cape Verde and the Canary Islands, Sci. Mar., 76, 65–78, doi:10.3989/scimar.03607.18C.

Pickett, M. H., and Paduan J. D., 2003. Ekman transport and pumping in the California Current based on the U.S. Navy's high-resolution atmospheric model (COAMPS), J. Geophys. Res., 108, 3327, doi:10.1029/2003JC001902, C10.

Risien, C. M., and Chelton D. B., 2008. A global climatology of wind and wind stress fields from eight years of QuikSCAT scatterometer data, J. Phys. Oceanogr., 38,2379–2413, doi:10.1175/2008JPO3881.1.

Samelson, R. M., Skyllingstad E. D., Chelton D. B., Esbensen S. K., O'Neill L. W., and Thum N., 2006. On the coupling of wind stress and sea surface temperature, J. Climate, 19, 1557-1566.

Schott, F. A., and McCreary J. P., 2001. The monsoon circulation of the Indian

Ocean, Prog. Oceanogr., 51, 1–123.

Seo, H., Miller A. J., and Roads J. O., 2007. The Scripps Coupled Ocean–Atmosphere Regional (SCOAR) Model, with Applications in the Eastern Pacific Sector, J. Climate, 20(3), 381-402.

Song, Q., Cornillon P., and Hara T., 2006. Surface wind response to oceanic fronts, J. Geophys. Res., 111(C12), C12006.

Spall, M. A., 2007. Midlatitude Wind Stress–Sea Surface Temperature Coupling in the Vicinity of Oceanic Fronts, J. Climate, 20(15), 3785–3801, doi: http://dx.doi.org/10.1175/JCLI4234.1

Strub, P. T., and James C., 2000. Altimeter-derived variability of surface velocities in the California Current System: 2. Seasonal circulation and eddy statistics, Deep Sea Res., Part II, 47, 831 – 870.

Strub, P. T., Combes V., Shillington F. A., and Pizarro O., 2013. Chapter 14 - Currents and Processes along the Eastern Boundaries, in Ocean Circulation and Climate A 21st Century Perspective, 103, 339-384, Elsevier Science.

Swenson, M. S., Niller P. P., Brink K. H., and Abbott M. R., 1992. Drifter observations of a cold filament off Point Arena, California, in July 1988, J. Geophys. Res., 97(C3), 3593 – 3610.

Ullman, D. S., and Cornillon P. C., 1999. Satellite-derived sea surface temperature fronts on the continental shelf of the northeast U.S. coast, J. Geophys. Res., 104,23,459–23,478.

Venegas, R. M., Strub P. T., Beier E., Letelier R., Thomas A. C., Cowles T., James C., Soto-Mardones L., and Cabrera C., 2008. Satellite-derived variability in chlorophyll, wind stress, sea surface height, and temperature in the northern California Current system, J. Geophys. Res., 113, C03015, doi:10.1029/2007JC004481.

Vecchi, G. A., Xie S.-P., and Fischer A. S., 2004. Ocean-atmosphere co-variability in the western Arabian Sea, J. Clim., 17, 1213–1224.

Xie, S.-P., 2004. The shape of continents, air-sea interaction, and the rising branch of the Hadley circulation, in The Hadley Circulation: Past, Present and Future, edited by H. F. Diaz and R. S. Bradley, pp. 121 – 152, Kluwer Acad., Dordrecht, Netherlands

Yang, G., Wang F., Li Y., and Lin P., 2013. Mesoscale eddies in the northwestern subtropical Pacific Ocean: Statistical characteristics and three-dimensional structures, J. Geophys. Res. Oceans, 118, 1906–1925, doi:10.1002/jgrc.20164.

Wang, Y., Castelao R. M., and Yuan Y., 2015. Seasonal variability of alongshore winds and sea surface temperature fronts in Eastern Boundary Current Systems, J. Geophys. Res. Oceans, 120, 2385–2400, doi:10.1002/2014JC010379.

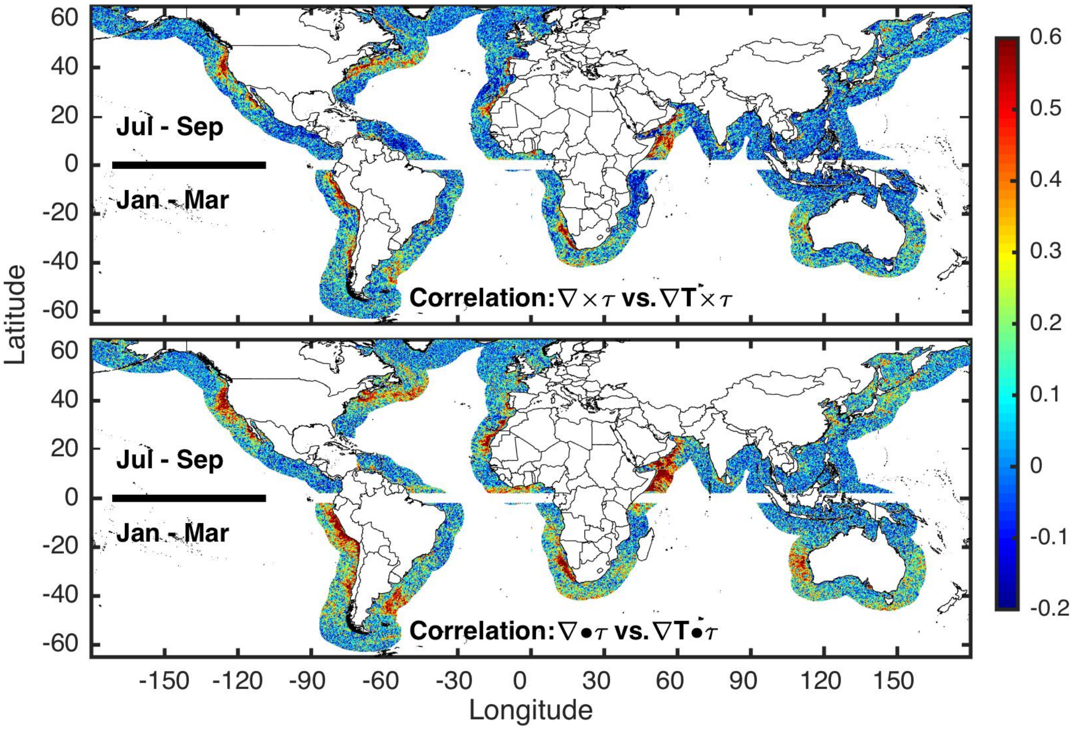

Figure 4.1 - Global maps of correlation between (top) crosswind SST gradient and wind stress curl and between (bottom) downwind SST gradient and wind stress divergence. Only observations during summer (January to March in northern hemisphere, July to September in the southern hemisphere) were used for computing the correlations.

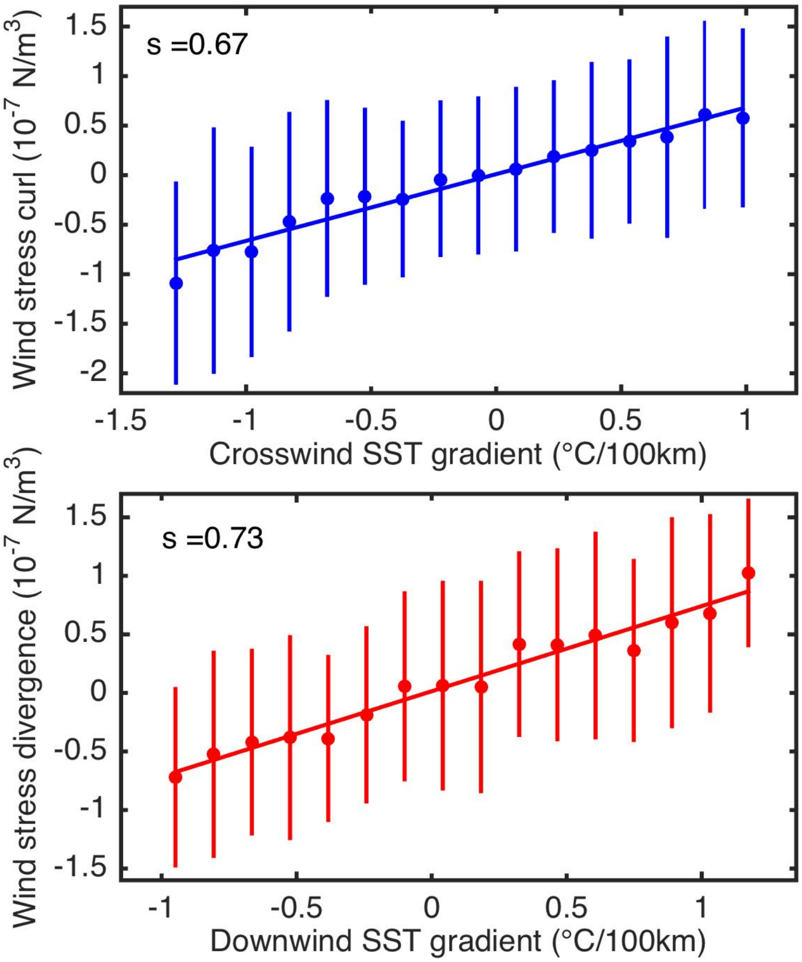

Figure 4.2 - Linear regression between (top) crosswind SST gradient and wind stress curl and between (bottom) downwind SST gradient and wind stress divergence for May 2004 in one region off Peru. The respective coupling coefficients are label in each panel.

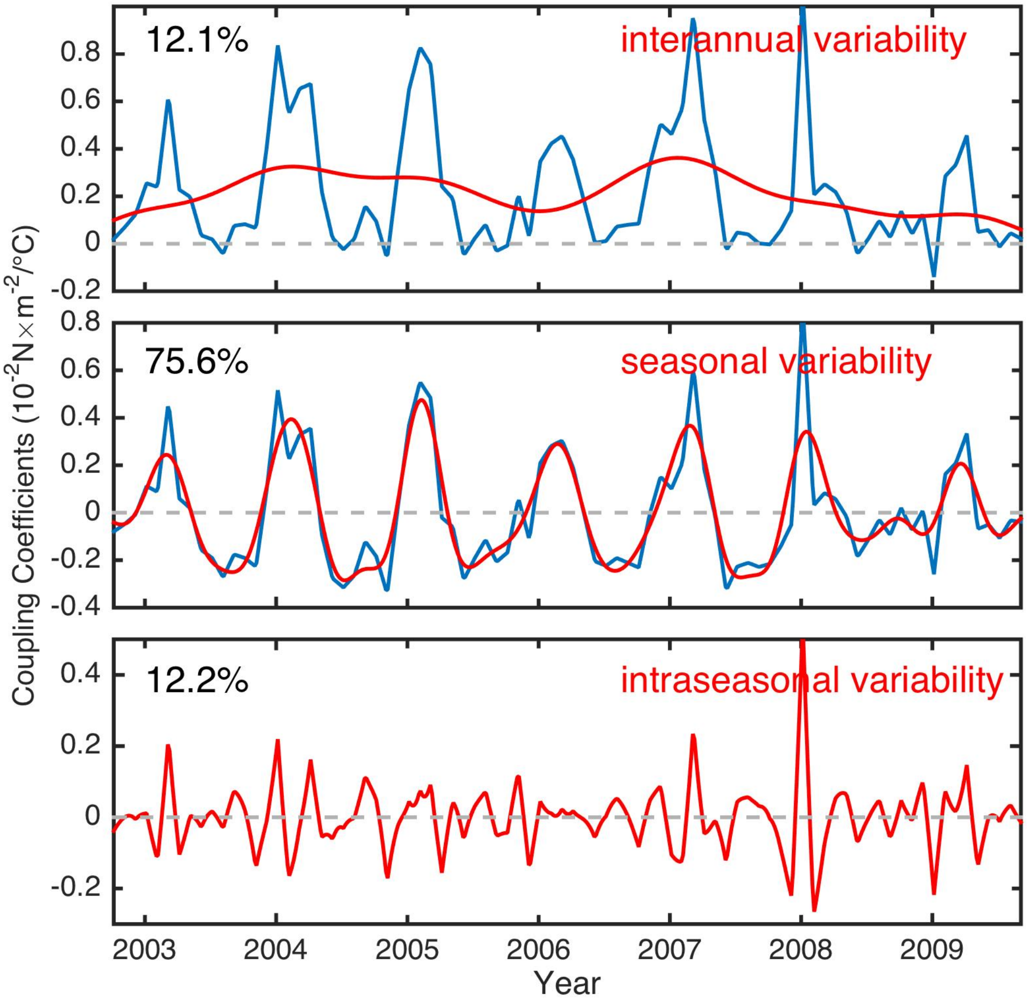

Figure 4.3 - (top) Monthly time series of coupling coefficients between crosswind SST gradients and wind stress curl in one region off Peru (blue). The time series was successfully low-pass filtered, so as to isolate (top) interannual, (middle) seasonal, and (bottom) intraseasonal variability (shown in red). See text for details.

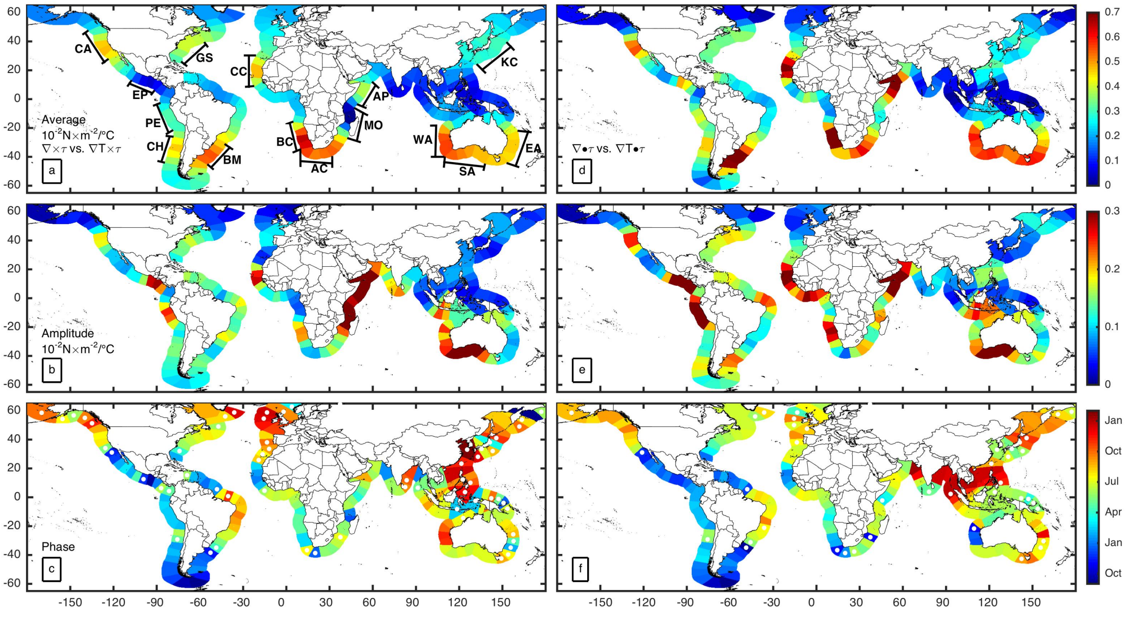

Figure 4.4 - Overall average (a, d) and amplitude (b,e) and phase (c, f) of the seasonal cycle calculated from monthly time series of coupling coefficients (10^{-2}N×m^{-2}/°C). The color scale of the phase map (c, f) is repeated from October to January in order to avoid discontinuities in the figure. CA: California Current System; EP: Eastern Tropical Pacific; PE: Humboldt Current off Peru; CH: Humboldt Current off Chile; BM: Brazil-Malvinas Confluence Zone; GS: Gulf Stream; CC: Canary Current; BC: Benguela Current; AC: Agulhas Current; MO: Mozambique Channel; AP: Arabian Peninsula; WA/SA/EA: Western /Southern/Eastern Australia; KC: Kuroshio Current.

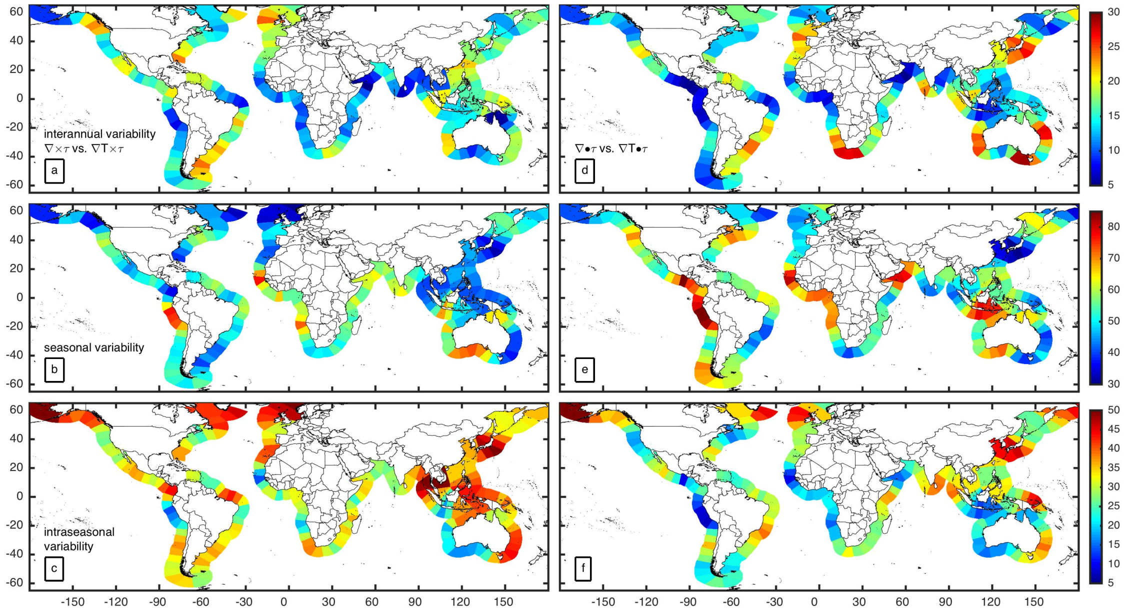

Figure 4.5 - Fraction (%) of total variance explained by interannual (>12 months; a,d), seasonal (between 6 and 12 months; b, e) and intraseasonal (< 6 months, c, f) variability. Note that different colorbars are used for different frequency bands to reveal as much as possible of the spatial patterns.

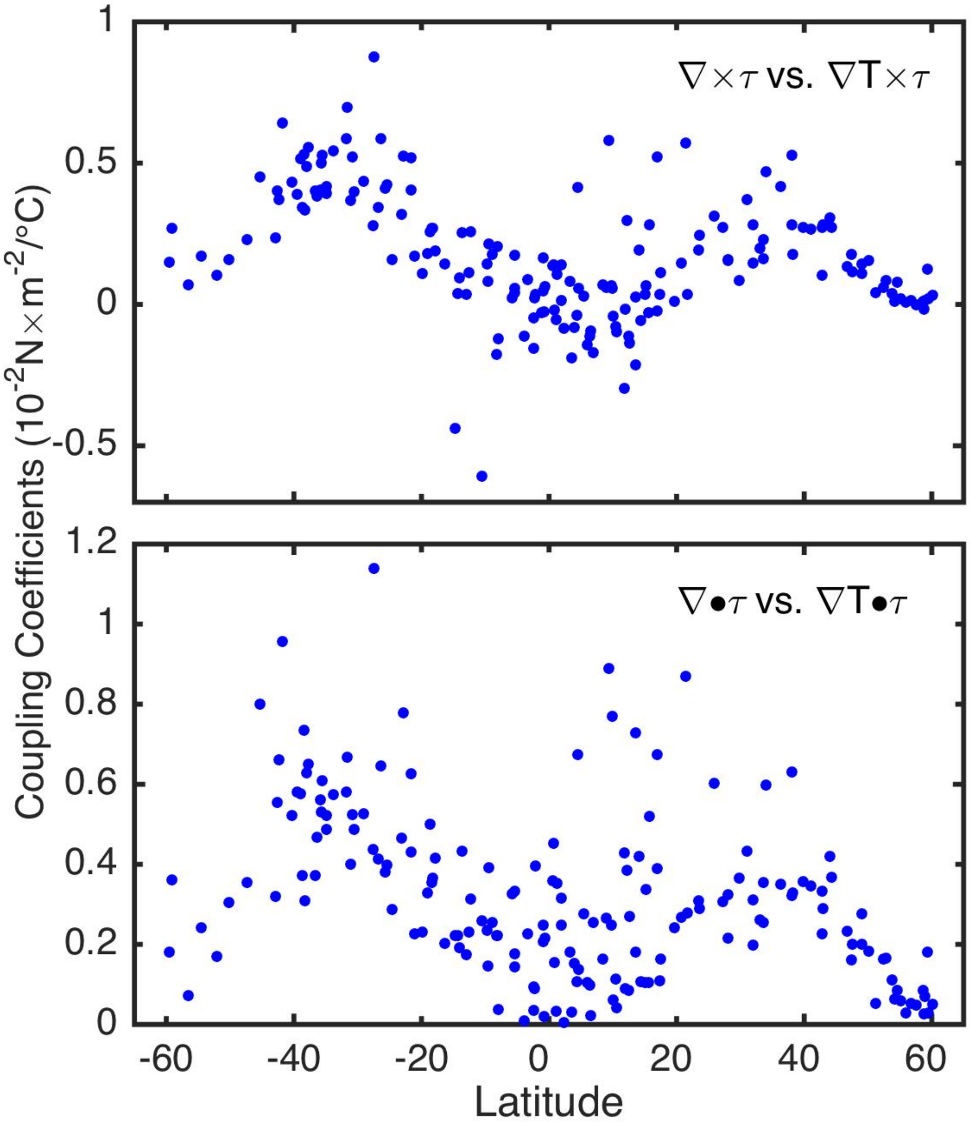

Figure 4.6 - Meridional distribution of mean coupling coefficients in the global coastal ocean. Coupling coefficients between crosswind SST gradients and wind stress curl are shown on top panel, while the coefficients between downwind SST gradients and wind stress divergence are shown on bottom panel.

CHAPTER 5

SALINITY VARIABILITY AND WATER EXCHANGE IN INTERCONNECTED ESTUARIES

Wang, Y., R. M. Castelao and D. Di Iorio, to be submitted to *Estuaries and Coasts*

5.1 Abstract

A high resolution coastal ocean model is used to investigate salinity variability and water exchange in a complex coastal system off the southern U.S. characterized by three adjacent sounds that are interconnected by a network of channels, creeks and intertidal areas. With a few exceptions, model results are highly correlated with observations from the Georgia Coastal Ecosystem Long Term Ecological Research (GCE-LTER) program, revealing a high degree of salinity variability at the Altamaha River and Doboy Sound, decreasing sharply toward Sapelo Sound. A Lagrangian particle tracking method is used to investigate residence time and connectivity in the system. Residence time is highly variable, increasing with distance from the Altamaha River and decreasing with river flow, demonstrating that discharge plays a dominant role in transport processes and estuary-shelf exchange. Connectivity between the Altamaha River and Doboy Sound is high in all seasons, with exchange occurring both via the oceanic and the marsh pathways. While particles released in the Altamaha and Doboy rarely reach Sapelo Sound, particles released at Sapelo Sound and the creeks surrounding the main channel can influence the entire estuarine system.

5.2 Introduction

The Georgia coast is a complex estuarine system, with sounds connected by a network of channels, creeks and intertidal areas (*Di Iorio and Castelao*, 2013). Located along the central coast of Georgia around Sapelo Island, the Altamaha River and Doboy and Sapelo Sounds (Figure 5.1) are additionally connected by the Intracoastal Waterway. The dominant source of freshwater to the system is the Altamaha River, which is one of the largest rivers in the southeastern U.S. (*Sheldon and Burd*, 2014). Maximum river runoff occurs during spring (*Menzel*, 1993), although a secondary peak in river discharge can also be observed in some years during fall (*Blanton and Atkinson*, 1983). The frequency of occurrence of anomalously low-discharge conditions in the Altamaha River seems to have increased over the last decades (*Medeiros et al.*, 2015). This long-term decrease in freshwater delivery to the estuary has been at least partially linked to freshwater withdrawal within the watershed (*Fanning*, 2003).

River discharge is the dominant factor controlling salinity variability in the Altamaha-Doboy-Sapelo estuarine complex (*Di Iorio and Castelao*, 2013). In addition to density-driven circulation, tides and wind forcing are also recognized as important drivers of horizontal exchange between estuaries and the coastal ocean (*Geyer and Signell*, 1992). The South Atlantic Bight off the coast of Georgia is characterized by large semidiurnal tides, ranging from 1.8 m during neap to 2.4 m during spring tides (*Di Iorio and Castelao*, 2013). Semidiurnal tides can account for roughly 80% of the kinetic energy over the inner- and mid-shelf (*Pietrafesa et al.,* 1985). The tidal band can also account for 80-90% of the cross-shelf and 20-40% of the alongshelf current variance (*Tebeau and Lee,* 1979; *Lee and Brooks,* 1979). As such, tides can contribute substantially to estuary-shelf exchange in the South Atlantic Bight.

Wind forcing in the region is characterized by strong seasonal variability. Winds are predominantly northeastward during summer and southwestward during fall (*Weber and Blanton*, 1980; *Blanton et al*., 2003). Winds are less persistent during spring and winter, although an offshore component is clearly recognizable in winter (*Menzel*, 1993). Southwestward winds are generally associated with relative increases in salinity at the mouth of the Altamaha River, and with decreases in salinity at Doboy and Sapelo Sounds (*Di Iorio and Castelao*, 2013).

Estuarine circulation and estuary-shelf exchange have a major impact on the ecology, chemistry, water quality and sedimentary processes in estuarine and coastal environments (*Geyer and Signel*, 1992). In particular, the residence time, the average time a water particle spends within the estuary, or in some portion thereof (*Geyer and Signell*, 1992), is one of the most important factors influencing water contamination and nutrient levels, distributions of organics, and their spatio-temporal variations in bays and estuaries (*Aikman and Lanerolle*, 2004). Previous studies have shown that river discharge is an important factor determining flushing time in the Altamaha River. Short flushing times are generally associated with large river discharge while comparatively longer flushing times are usually observed during periods of low flow, although the dependence is not always linear (*Alber and Sheldon*, 1999a). Using box models, *Sheldon and Alber*

(2002) showed that the flushing time (which is defined as the local residence time at the head of the estuary) in the Altamaha River generally ranges between 1 to 6 days depending on river flow. However, these studies assumed a simplified geometry, not considering possible connections between the Altamaha River and Doboy and Sapelo Sounds farther north. In fact, most previous estuarine studies have focused on a single estuary and its connection with the coastal ocean. The comparatively few existing studies addressing multi-inlet estuaries (e.g., *Traynum and Styles*, 2008; *Zhao et al.,* 2010) have shown that the flow in those cases can be driven by mutual forcing between the adjacent inlets. Idealized numerical model simulations have suggested that the network of creeks and channels connecting the Altamaha River and Doboy Sound are also likely to strongly increase connectivity in the system (*Di Iorio and Castelao*, 2013).

In this paper, we use a high-resolution coastal ocean model to investigate salinity variability and water exchange in interconnected estuaries characterized by complex geometry of the Georgia coast. The model implementation is described in section 2, followed by model evaluation and identification of salinity variability in section 3. We quantify residence time in the system, and how it varies seasonally, in section 4. Preferred transport pathways in the system are identified in section 5, providing insight into connectivity among the different estuaries. Results are summarized and conclusions are presented in section 6.

5.3 Methods

The numerical modeling effort was based on the Finite Volume Coastal Oceanic Model (FVCOM; *Chen et al.,* 2006a, 2006b, 2007, 2008). We chose FVCOM because for the use of unstructured grids and wetting and drying capability, which are important features to model circulation in estuaries characterized by complex geometry and bathymetry. FVCOM has been successfully used to model the Satilla River Estuary off the Georgia coast (*Chen et al.,* 2008), which presents complex geometry similar to the study region. FVCOM has also been recently used in a wide variety of estuarine studies (*Ralston et al.,* 2010; *Zhao et al.,* 2010; *Lemagie and Lerczak,* 2014).

The spatial domain covers the estuarine complex, from the Altamaha River in the south to Sapelo Sound in the north (Figure 5.1). Bottom topography was obtained from the National Oceanic and Atmospheric Administration (NOAA) National Geophysical Data Center, Coastal Relief Model. The horizontal resolution of the model is 50-70 m in tidal creeks and over salt marshes, and 100-200 m in the main water channels. The grid scale increases slowly over the shelf to about 1.2 km near the open boundary. The horizontal resolution used here is comparable to the resolution used in other estuarine studies using FVCOM [*Chen et al.,* 2008; *Ralston et al.,* 2010; *Zhao et al.,* 2010]. The total number of triangular elements and nodes are 351,731 and 177,796, respectively. In the vertical dimension, six layers are specified in the generalized terrain-followed σ-coordinate system, similarly to *Zhao et al.* (2010). The Coriolis parameter is constant, matching the value near the center of the domain.

At the open boundaries, the model was forced by 8 tidal constituents that were extracted from the Oregon State University tidal model (*Egbert and Erofeeva*, 2002). Time variations in offshore stratification along the boundaries were excluded. Winds were measured at the NOAA National Data Buoy Center (NDBC) buoy 41008 located at 31.40°N, 80.87°W (Figure 5.1). Because of the lack of spatially resolving observations and considering the relative small extent of the model domain, winds were considered spatially uniform in the model simulations. Freshwater discharge input at the head of the Altamaha River was obtained from the United States Geological Survey gauge at Doctortown. Measurements are available at hourly intervals since 1931. The ungauged area within the Altamaha River watershed constitutes less than 3% of the river discharge [*Alber and Sheldon*, 1999a]. Moore [1996] has suggested that freshwater input from groundwater discharge can be important in coastal regions along the South Atlantic Bight. Unfortunately, no quantitative assessment of the magnitude of freshwater input is available. As such, groundwater input was not considered in the model implementation. Possibly as a result of neglecting groundwater inputs, preliminary tests indicated that modeled salinity at Sapelo Sound in the northern sector of the domain was larger than observations. To address this disparity, a small freshwater discharge was introduced at the head of Sapelo Sound, using the same temporal variability observed at the Altamaha River. Multiple sensitivity experiments were pursued, and it was determined that imposing a freshwater input equivalent to 5% of the discharge at the Altamaha River minimized the bias between modeled and observed salinity at Sapelo Sound. Although somewhat arbitrary, the input of freshwater at Sapelo River at the head of Sapelo Sound acted as a crude attempt to capture the known input of an unknown quantity of freshwater by groundwater inflow and surface runoff associated with local precipitation. The model was run for 2008, a year when the seasonal evolution of river discharge was similar to the long-term average, and for 2012-2014, capturing the transition of a severe drought to high discharge conditions (*Medeiros et al.,* 2015). Results from the 3-year-long simulation representing 2012-2014 will be reported in another manuscript. An initial oceanic salinity of 35 was applied to the entire domain, and riverine water with salinity of zero was input at the rivers. The model was run for a spin-up period of approximately 100 M2 tidal cycles at the beginning of the year 2008. Comparisons of the salinity standard deviation over the entire simulation period with the salinity standard deviation considering a spin-up time 50% shorter produced nearly identical results, suggesting that the spin-up period was enough to minimize the influence of the initial conditions. Results reported here are from times after the spin-up period. Observations collected as part of the Georgia Coastal Ecosystem Long Term Ecological Research (GCE-LTER) project (*Di Iorio and Castelao*, 2013) were used for model evaluation. Precipitation data was also collected as part of the GCE-LTER project.

In order to investigate water movement within the estuary and between the estuary and the coastal ocean, three-dimensional particle tracking was pursued. A total of 5,643 particles were initially distributed over the main channels, tidal creaks and salt marsh areas. No particles were released over the shelf (see Figure 5.3a for delineation of the area where particles were released). Particles were released near the bottom and tracked for 60 days in early March, early June, mid-August and mid-November (green lines on Figure 5.2) to capture the influence of seasonal variations in river discharge and wind forcing. The early-March release captured the peak in river discharge. Early June and mid-August represented periods of low river discharge at the beginning and near the end of the period of dominant upwelling favorable winds, respectively. At mid-November, river discharge was low and winds were predominantly downwelling favorable. In each case, particles were released 6 times throughout a tidal cycle. During the simulations, some of the particles became artificially trapped in the salt marsh and stopped moving. Those particles were discarded from all subsequent analyses.

The Lagrangian particle tracking scheme was used to quantify timescales, connectivity and transport pathways in the system. The local residence time (*Dronkers and Zimmerman,* 1982) at each node was determined by the average time it took for the 100 particles that were released closest to that particular node to exit the estuary, weighted by the inverse of the distance between the node and the initial position of the particle. That computation is repeated 6 times for each node, once for each particle release throughout a tidal cycle. The final local residence time was computed as the average of these 6 estimates. The standard deviation of these 6 estimates was also computed to obtain a measure of variability in local residence time as a function of the phase of the tide during the particle release. We note that particles are often transported back into the estuary by tidal currents after leaving the estuary for the first time. Here, the local residence time was computed once the particle left the estuary for the first time.

Particle trajectories were also used to identify connectivity between the different channels, tidal creeks and intertidal areas. For that, the entire estuary was once again divided into three subdomains representing the Altamaha River and Doboy and Sapelo Sounds. The trajectory of each particle was then used to determine which subdomains (Figure 5.3c) were visited by the respective particle. In the example shown in Figure 5.3a, a particle was released near the head of Sapelo Sound. The particle was first transported offshore into the coastal ocean, and subsequently into Doboy Sound and then into the Altamaha River. In the example shown in Figure 5.3b, another particle released at Sapelo Sound was also transported into Doboy Sound and the Altamaha River. In that case, however, the particle was transported through the network of creeks and channels connecting the different subdomains. In both those cases, the particles were considered to have visited all three subdomains. Connectivity was defined for each node as the subdomains visited by the particle closest to the respective node. We note that a given node was considered connected to a given estuary even if a particle reached that estuary in only one of the six simulations where particles were released at different phases of the tidal cycle. In other words, if a particle closest to a given node reached a subdomain at any of the 6 releases, then that node was considered connected to that subdomain. That calculation was repeated for the particle release experiments during the four seasons, allowing for identification of how connectivity in the estuary varied as a function of river discharge and wind forcing.

Lastly, we also identified the pathways by which the node was connected to a given subdomain. In the example shown in Figure 5.3a, the particle was first transported out into the coastal ocean, and then back into Doboy Sound and the Altamaha River. We refer to this as the oceanic pathway. In other instances, however, as shown in Figure 5.3b, particles move between the subdomains via the Intracoastal Waterway or tidal creeks, in which case the node was considered connected to the subdomains via the marsh pathway. Since there were six particle releases for each season (i.e., at different phases of the tidal cycle), each node can be connected to a given subdomain by both the oceanic and the marsh pathways.

5.4 Model evaluation and salinity variability in the system

Model results were compared with time series of daily-averaged salinity from 8 moorings deployed as part of the GCE-LTER program (*Di Iorio and Castelao*, 2013). For consistency, modeled salinity was also averaged at daily intervals before comparison. In order to estimate the effective number of degrees of freedom, we first computed the autocorrelation for each time series and determined the time scale in which the autocorrelation decrease to 0.37. We then divided the total record length by that time scale to identify the number of independent, uncorrelated time periods in the total record. Correlation coefficients between modeled and observed salinity are shown in Figure 5.4. Correlations varied between 0.7 and 0.85 at most stations, and were statistically significant at the 95% confidence level. Correlations were considerably weaker (although still significant) at GCE-1 and GCE-3. The decrease in correlation coefficients between the Altamaha River and Sapelo Sound was expected, since salinity variability at Altamaha is strongly forced by river discharge (*Alber and Sheldon*, 1999b), which is considered in the model. Salinity variability at the head of Sapelo Sound at GCE-1, on the other hand, is strongly influenced by local runoff and/or groundwater inputs recharged by precipitation (Figure 5.5), which were not directly considered in this study. The correlation coefficient is also reduced near the mouth of Sapelo Sound at station GCE-3. At GCE-7, correlation was also very small and not statistically significant. That station is located substantially upstream along the Altamaha River and it is characterized by near zero salinity most of the time. As such, salinity variability is often dominated by noise or by weak events that were not well represented in the model.

Additional model evaluation was pursued by comparing the correlation and lags between river discharge and salinity in the model domain. Using in situ observations from the GCE-LTER moorings (see Figure 5.4 for location), *Di Iorio and Castelao* (2013) showed that correlations between discharge and salinity show average time lags ranging from 4 days in the Altamaha estuary to 12 days in Sapelo Sound. Model results were consistent with the observations, with maximum correlation between river discharge and salinity occurring for lags of 4-6 days at the Altamaha River and between 12-16 days at Sapelo Sound (Figure 5.6). This suggests that the model was able to capture not only salinity variability in the system, but also the dynamic response to changes in river discharge. It is interesting to note that at the upstream sector of the Altamaha River, salinity was not significantly correlated to river discharge. At those locations, salinity was always near zero, except for a few sporadic events. Another area of low correlation is near the mouth of Sapelo Sound. Analysis of mooring observations reveal that the region is characterized by significant correlation between river discharge and salinity (*Di Iorio and Castelao*, 2013), indicating that the model was not able to properly capture the dependence of salinity variability to river discharge in that part of the domain. This is consistent with the low correlations between modeled and observed salinity reported earlier for GCE-3 (Figure 5.4).

Maps of mean salinity and standard deviation in the estuary are shown in Figure 5.7. River inflow in the South Atlantic Bight is a major driver of salinity variability on the inner shelf (*Blanton and Atkinson*, 1983). As expected, average salinity was low in the Altamaha River, increasing offshore and to the north toward Doboy and Sapelo Sounds. Small creeks and channels connecting the Altamaha River and Doboy Sound were also characterized by low average salinities, suggesting that some of the freshwater from the Altamaha River leaked into Doboy Sound via those channels. Low average salinity was also observed near the head of Sapelo Sound, a result also observed based on in situ data (*Di Iorio and Castelao*, 2013). It is important to point out, however, that the correlation between observation and model results was comparatively low in that area (Figure 5.4). More interestingly, the map of standard deviation of salinity in the estuary revealed the areas that were characterized by high variability. The most obvious feature is the high values observed near the mouth of the Altamaha River extending into the coastal ocean, where strong mixing between river and shelf water occurs (*Di Iorio and Kang*, 2007). High variability was also observed in the creeks connecting the Altamaha River and Doboy Sound, once again supporting the interpretation that those channels played an important role connecting the different subdomains. An empirical orthogonal function (EOF) decomposition of the surface salinity field (not shown) revealed a spatial pattern for the dominant mode that was very similar to the standard deviation map shown in Figure 5.7b. The amplitude time series of the dominant mode, which explains 84.4 % of the total variance, was highly correlated with river discharge (r = 0.84), revealing that most of the salinity variability described above (Figure 5.7b) was related to variability in river inflow.

Although Doboy and Sapelo Sounds were both characterized by high average salinity, there was a remarkable difference in salinity standard deviation between the two subdomains. Doboy Sound was characterized by high variability, revealing a large degree of influence from low salinity water from the Altamaha River. Analysis of individual maps of salinity revealed that, in addition to low salinity water leaking into Doboy Sound via small channels and creeks, as described above, low salinity water also enters Doboy Sound via the mouth during flooding tides. Salinity variability decreases substantially between Doboy and Sapelo Sound, so that salinity standard deviation in the northern sector of the domain, farther from the river, was substantially smaller. The sharp decrease along the channels between Doboy and Sapelo Sound may be related to nodal points that are often observed in interconnected estuaries, produced by simultaneous tidal forcing from both ends of the channel (*Traynum and Styles*, 2008).

5.5 Residence time

The timescale in which water remains in an estuary is crucially important for a number of ecological processes [*Church*, 1986; *Alpine and Cloern*, 1992; *Rasmussen and Josefson,* 2002; *Duarte and Vieira*, 2009]. Maps of local residence time for each season are shown in Figure 5.8. There is a general tendency, regardless of the season, for residence times to increase with increasing distance from the ocean. Near the mouth of each Sound, the residence times approach zero, since particles are easily transported offshore onto the shelf during a tidal cycle. Analyses of individual particle trajectories indicate that the excursion length of the tides near the mouth of the estuaries is of the order of 6-8 km. The largest residence times are observed in small creeks bordering uplands near the head of the Sounds. Since those areas are more likely to be developed, any input of contaminants or nutrients due to anthropogenic activities is likely to have a relatively large impact on estuarine water quality, given the comparatively large residence time observed in those areas. The increase in residence times as a function of distance from the mouth is more easily observed when the residence times are averaged along the main channels of each Sound (i.e., along the lighter shaded regions delineated in Figure 5.3c). In all cases, residence times increase from nearly zero close to the mouth to several days upstream (Figure 5.9).

Comparison among the different subdomains revealed substantial differences in residence time in the system (Figure 5.8). Values are smallest in the Altamaha River during spring, when strong river discharge (Figure 5.2) contributes to the rapid transport of the particles toward the shelf, which is consistent with *Alber and Sheldon* (1999a) results. The local residence time approximately doubles in the Altamaha River in the other seasons when river discharge is reduced (Figure 5.9). For a given distance from the mouth, the residence time at Doboy Sound is generally larger than at the Altamaha River (Figure 5.9), likely because of reduced influence of direct river discharge at Doboy Sound. The increase in residence time compared to the Altamaha River is especially true for the complex network of channels and creeks near the uplands to the southwest of the main channel at Doboy Sound (around 81.35°-81.4°W, 31.37°-31.44°N), when the local residence time during late fall can be in excess of 5 days. At Sapelo Sound, on the other hand, the local residence time is significantly larger, especially from the mid estuary to its head (Figure 5.8). At those locations, the residence time is large regardless of the season (Figure 5.9). A small reduction in residence time is observed during mid-August after the region is exposed to strong and persistent upwelling favorable winds. For any given distance from the estuary mouth, residence time at Sapelo Sound exceeds the residence time at the Altamaha River and Doboy Sound for all seasons (Figure 5.9).

It is interesting to note that in some seasons a local minimum in residence time is observed around 24 km in the Altamaha River (Figure 5.9). Detailed analysis of individual particle trajectories reveal that in some cases particles released in one or more of the multiple channels in that area may become trapped, while particles released upstream may continue its trajectory to the ocean via another channel. That is particularly clear in the spatial distribution of local residence time during high discharge conditions (Figure 5.8a), for example, when the local residence time is larger in the southern channel of the river (around –81.5°W, 31.35°N) compared to the northern channels.

Analysis of maps of the standard deviation of the local residence time among the six particle release experiments in each season scaled by the respective average residence time (Figure 5.10) reveals that variability as a function of the phase of the tidal cycle is small, except near the mouths of the estuary. At those regions near the ocean, while a particle released at ebb tides can be quickly exported, a particle released at low tides will be first transported into the estuary by flood currents and only subsequently exported. Since the local residence time is small in that area, the relative measure of variability shown in Figure 5.10 is large, reaching 80% in some locations. Away from the mouth of each sound, however, the standard deviation is small compared to the average of the six simulations, indicating that the patterns described before (Figure 5.8) are robust and not dependent on the phase of the tidal cycle in which particles were released.

Bulk estimates of residence time, or of other variables related to residence time, are often calculated for estuaries. The transit time, defined as the total amount of time it takes for freshwater to transit through an estuary, has been previously estimated for the Altamaha River to vary between 1.6 and 9 days for river flow exceeding 100 $m^3 s^{-1}$ (*Sheldon and Alber*, 2005). That is comparable to our estimates of residence time at the head of the Altamaha River, which range from about 2 days during high river discharge conditions to about 7 days for low river flow (Figure 5.9). This suggests that bulk estimates of transit time can provide useful information even in systems characterized by such complex geometry. The analysis also reveals, however, that much information is lost when a bulk measure is used. The local residence time at the main channel of Doboy Sound is quite different than in the network of small channels and creeks just to the southwest, for example (Figure 5.8). Although that is true for the particle releases pursued here for each of the four seasons, the differences are particularly large in mid-November (Figure 5.8d and Figure 5.9a). This local increase, which by definition cannot be captured by bulk estimates, can have important ecosystem implications. Any pollutant release or nutrient input to that area can presumably have a larger influence (all other factors being equal) in the estuary during mid-November than during the other time periods investigated here, for example.

5.6 Connectivity and transport pathways

Results shown in the previous section have revealed large spatial and temporal variations in residence time in the estuarine system. River discharge [*Alber and Sheldon*, 1999b; *Lemagie and Lerczak*, 2014], winds [*Geyer,* 1997] and tidal forcing [*Lemagie and Lerczak,* 2014] have all been shown to influence residence time. Using a simple idealized numerical model set up, *Di Iorio and Castelao* [2013] noticed that the channels connecting the Altamaha River and Doboy sound could play a large role in water exchange between the subdomains, since the channels offer an alternative pathway for exchange. As such, the connectivity and transport pathways between the subdomains are investigated here to identify how particles move within the system.

We track the trajectory of each particle released in the model and identify which parts of the estuary the particle was transported to (Figure 5.11). The release location of a particle that was found at the Altamaha River and at Doboy Sound at some point in its trajectory, but not at Sapelo Sound, is marked in green, for example. Connectivity between the Altamaha River and Doboy Sound is high regardless of the season, with particles released at the river reaching Doboy Sound by both pathways most of the time (Figure 5.12). The only exception is during the peak in river discharge, when careful examination reveals that particles released in the southern part of the Altamaha River near the mouth only reach Doboy Sound via the oceanic pathway. Particles released in several of the creeks between the Altamaha River and Doboy Sound only reach both subdomains via the marsh pathway, with the exception of high river discharge conditions during spring, when both pathways are available. The differences are generally small, however, and the analysis reveals a high degree of connectivity between the Altamaha River and Doboy Sound. It is interesting to note that there is a divide in connectivity approximately along the center of the main channel in Doboy Sound. While particles released in the southern part of the channel are restricted to Doboy Sound and the Altamaha River, particles released in the northern part of the channel generally also reach Sapelo Sound, especially during summer (Figure 5.11). In that case, connectivity occurs both via the oceanic and the marsh pathways (Figure 5.12).

The fact that most particles released in the Altamaha River and in (at least the southern half of) Doboy Sound are not transported into Sapelo Sound can help explain the large difference in salinity standard deviation between those subdomains (Figure 5.7b). The large connectivity between Doboy Sound and the Altamaha River indicates that low-salinity water from the river is easily transported into Doboy Sound, either via the network of creeks connecting the system or via the coastal ocean (Figure 5.12). This is consistent with the numerical simulations of *Di Iorio and Castelao* (2013), who revealed that a large amount of freshwater introduced in the Altamaha River could be transported into their idealized representation of Doboy Sound. Once at Doboy Sound, however, the low-salinity water is not easily transported into Sapelo Sound (Figure 5.12). This reduced connectivity would result in reduced salinity variability and increased mean values in the northern part of the domain, consistent with the model results (Figure 5.7)

Creeks and channels between Doboy and Sapelo Sounds are remarkable in the sense that they are regions characterized by high connectivity year-round. Specifically, particles released in that region are able to reach all subdomains in all seasons (yellow in Figure 5.11). While the transport pathway over the marsh is available in all seasons, a few gaps in connectivity via the oceanic pathway exist (Figure 5.12). Connectivity along the main channel of Sapelo Sound is also generally high, especially on the downstream sector near the mouth, when connectivity is high year-round. Therefore, although most particles released at the Altamaha River or Doboy Sound are not transported into Sapelo Sound, a large fraction of the particles released at the downstream half of Sapelo Sound are transported into Doboy Sound and into the Altamaha River (Figure 5.11; the exception is the early June release, when most particles do not reach the Altamaha River). Upstream near the head of Sapelo Sound, however, connectivity is very low in mid-August and mid-November. During that time, many particles are either constrained to Sapelo Sound itself, or they may reach Doboy Sound in a few cases, but not the Altamaha River (Figure 5.11).

The analysis presented here provides an unprecedented view of connectivity and transport pathways in the estuarine system, revealing substantial spatial and temporal variability. This variability can have large implications for the ecosystem. For example, while nutrient inputs (or the input of any other material) at the Altamaha River are likely to have a large influence on the river itself and on Doboy Sound, the influence on Sapelo Sound is likely to be substantially smaller. Constituents introduced into the system with groundwater input at the network of creeks connecting Doboy and Sapelo Sound, on the other hand, are likely to influence all three subdomains. The same is true for anthropogenic inputs. Depending on the location of the input, a contaminant may be restricted to a few areas, or it may be spread to all subdomains. The large spatial variability in local residence time also indicates that, depending on the location of the input of a contaminant, it may be rapidly exported to the coastal ocean, or it may remain much longer within the estuary.

5.7 Conclusions

A high resolution coastal ocean model was used to investigate circulation and variability in adjacent estuaries off the southeastern U.S. The region is characterized by complex topography where adjacent estuaries are interconnected by a network of channels, tidal creeks and intertidal marshes. Comparisons with observations reveal that the model is able to capture salinity variability over most of the domain, especially along the Altamaha River and Doboy Sound, where salinity is highly correlated with river discharge with relatively short time lags. The model-data comparisons worsen near the head of Sapelo Sound, where seasonal variability in salinity is also strongly influenced by local precipitation.

Model results reveal for the first time the region characterized by high salinity variability in the system in high resolution, which extends from the downstream half of the Altamaha River to Doboy sound. The network of creeks and channels connecting the River and the Sound play a large role in the spread of the low-salinity water in the system. Salinity variability at Sapelo Sound is substantially smaller. This is consistent with the identified preferred transport pathways in the system, which indicates that particles released at the Altamaha River or Doboy Sound rarely make it into Sapelo Sound farther north. Connectivity between the River and Doboy Sound is very high during all seasons, with exchange occurring both via the oceanic and the marsh pathways. The local residence time is strongly variable spatially, being significantly larger at Sapelo Sound than farther south. At the Altamaha River and Doboy Sound, the residence time is smaller during high discharge conditions, demonstrating the large influence of the river on transport processes and estuary-shelf exchange.

5.8 Acknowledgement

We gratefully acknowledge support by the National Science Foundation (OCE-1237140) as part of the Georgia Coastal Ecosystems Long Term Ecological Research project. Additional support was provided by an Institutional Grant (NA100AR4170098) to the Georgia Sea Grant College Program from the National Sea Grant Office, National Oceanic and Atmospheric Administration (NOAA), U.S. Department of Commerce and by grant award NA11NOS4190113 to the Georgia Department of Natural Resources (DNR) from the Office of Ocean and Coastal Resource Management (OCRM), NOAA. All views, opinions, statements, findings, conclusions, and recommendations are those of the authors and do not necessarily reflect the opinions of NSF, the Georgia Sea Grant college Program, DNR, OCRM or NOAA.

Reference

Aikman, F.A. and L. W. J. Lanerolle (2004), Report on the National Ocean Service Workshop on Residence/Flushing Times in Bays and Estuaries. NOAA Office of Coast Survey, Silver Spring, MD (http://www.nauticalcharts.noaa.gov/csdl/ residencetime.html).

Alber, M., and J. E. Sheldon (1999a), Use of a data-specific method to examine variability in the flushing times of Georgia estuaries, Estuarine Coastal Shelf Sci., 49, 469–482.

Alber, M., and J. E. Sheldon (1999b). Trends in salinities and flushing times of Georgia estuaries. Pages 528–531 in K. J. Hatcher, editor. Proceedings of the 1999 Georgia Water Resources Conference. University of Georgia, Athens.

Alpine A. E. and J. E. Cloern (1992), Trophic interactions and direct physical effects control phytoplankton biomass and production in an estuary, Limnology and Oceanography, 37, doi: 10.4319/lo.1992.37.5.0946.

Blanton, B. O., A. Aretxabaleta, F. E. Werner and H. E. Seim (2003). Monthly climatology of the continental shelf waters of the South Atlantic Bight. J. Geophys. Res., Oceans (1978–2012), 108(C8).

Blanton, J. O., and L. P. Atkinson (1983), Transport and fate of river discharge on the continental shelf of the southeastern United States, J. Geophys. Res., 88, 4730-4738.

Castelao, R., S. Glenn, O. Schofield, R. Chant, J. Wilkin and J. Kohut (2008), Seasonal evolution of hydrographic fields in the central Middle Atlantic Bight from glider observations. Geophys. Res. Lett., 35(3).

Chen, C., G. Cowles, and R. C. Beardsley (2006a), An unstructured grid, finite-volume coastal ocean model: FVCOM user manual, 2nd ed.,SMAST/UMASSD Tech. Rep. 06-0602, 315 pp., School for Marine Science and Technology, University of Massachusetts-Dartmouth, New Bedford, MA.

Chen, C., R. C. Beardsley, and G. Cowles (2006b), An unstructured grid, finite-volume coastal ocean model (FVCOM) system: Special Issue entitled "Advances in Computational Oceanography", Oceanography, 19(1),78–89.

Chen, C., H. Huang, R. C. Beardsley, H. Liu, Q. Xu, and G. Cowles (2007), A finite-volume numerical approach for coastal ocean circulation studies: Comparisons with finite-difference models, J. Geophys. Res., 112, C03018, doi:10.1029/2006JC003485.

Chen, C., J. Qi, C. Li, R. C. Beardsley, H. Lin, R. Walker, and K. Gates (2008), Complexity of the flooding/drying process in an estuarine tidal-creek salt-marsh system: An application of FVCOM, J. Geophys. Res., 113, C07052.

Church, T.M. (1986), Biogeochemical factors influencing the residence time of microconstituents in a large tidal estuary, Delaware Bay. Mar. Chem., 18: 393-406.

Di Iorio, D., and K. R. Kang (2007), Variations of turbulent flow with river discharge in the Altamaha River Estuary, Georgia, J. Geophys. Res., 112, C05016.

Di Iorio, D., and R.M. Castelao (2013), The dynamical response of salinity to freshwater discharge and wind forcing in adjacent estuaries on the Georgia coast. Oceanography 26(3): 44–51, http://dx.doi.org/10.5670/oceanog.2013.44.

Dronkers, J. and J. T. F. Zimmerman (1982), Some principles of mixing in tidal lagoons. Oceanologica acta. Proceedings of the International Symposium on Coastal Lagoons, Bordeaux, France, 9–14 September, 1981, p. 107–117

Duarte A. A. L. S. and J. M. P. Vieira (2009), Effect of tidal regime on estuarine residence time spatial variation. In: Mastorakis N, Helmis C, Papageorgiou CD, Bulucea CA, Panago - poulos T (eds) Energy, environment, ecosystems, development and landscape architecture. WSEAS Press, p 240−245.

Egbert, G. D. and S. Y. Erofeeva (2002), Efficient Inverse Modeling of Barotropic Ocean Tides. J. Atmos. Oceanic Technol., 19, 183–204. doi: http://dx.doi.org/10.1175/1520-0426(2002)019<0183:EIMOBO>2.0.CO;2

Fanning, J. L. (2003), Water use in Georgia, 2000; and trends, 1950–2000, Proceedings of 2003 Georgia Water Resources Conference, Univ. of Georgia, Athens.

Geyer, W. R. (1997), Influence of wind on dynamics and flushing of shallow estuaries. Estuarine Coastal Shelf Sci., 44, 713–722.

Geyer, W. R., and R. Signell (1992), A reassessment of the role of tidal dispersion in estuaries and bays. Estuaries 15:97–108,http://dx.doi.org/10.2307/1352684.

Lee, T. N. and D. A. Brooks (1979), Initial observations of current, temperature and coastal sea level response to atmospheric and Gulf Stream forcing on the Georgia shelf, Geophys. Res. Lett., 6, 321–324.

Lemagie, E. P., and J. A. Lerczak (2014), A comparison of bulk estuarine turnover timescales to particle tracking timescales using a model of the Yaquina Bay Estuary, Estuaries Coasts, 1–18, doi:10.1007/s12237-014-9915-1.

Medeiros, P. M., Seidel, M., Dittmar, T., Whitman, W. B. and Moran, M. A. (2015), Drought-induced variability in dissolved organic matter compostion in a marsh-dominated estuary, Geophys. Res. Lett., 42(15), 6446-6453.

Menzel, D. W. (1993), Ocean processes: U.S. southeast continental shelf. A summary of research conducted in the South Atlantic Bight under the Auspices of the U.S. Department of Energy from 1977 to 1991, Publ. DOE/OSTl-11674, 112, Off. of Sci. and Tech. Inf., U.S. Dep. of Energy, Washington, D. C..

Moore, W. S. (1996), Large groundwater inputs to coastal waters revealed by 226Ra enrichments. Nature, 380.

Pietrafesa, L. J., J. O. Blanton, J. D. Wang, V. H. Kourafalou, T. N. Lee, and K. A. Bush (1985), The tidal regime in the South Atlantic Bights, in Oceanography of the Southeastern U.S. Continental Shelf, edited by L. P. Atkinson, D. W. Menzel, and K. A. Bush, pp. 63–76, AGU, Washington, D. C.

Ralston, D. K., W. R. Geyer, and J. A. Lerczak (2010), Structure, variability, and salt flux in a strongly forced salt wedge estuary, J. Geophys. Res., 115, C06005, doi:10.1029/2009JC005806.

Rasmussen, B. and A. Josefson (2002), Consistent estimates for the residence times of micro-tidal estuaries. Estuar. Coast. Shelf Sci. 54: 65–73.

Sheldon, J. E. and A. B. Burd (2014), Alternating effects of climate drivers on Altamaha River discharge to coastal Georgia, USA. Estuaries and Coasts, 37:772-788.

Sheldon J. E. and M. Alber (2002), A comparison of residence time calculations using simple compartment models of the Altamaha River estuary, Georgia. Estuaries and Coasts 25:1304–1317. DOI: 10.1007/bf02692226.

Sheldon J. E. and M .Alber (2005) Comparing transport times through salinity zones in the Ogeechee and Altamaha river estuaries using squeezebox. In: Hatcher KJ (ed) Proc 2005 Georgia Water Res Conf. The University of Georgia, Athens

Tebeau, P. A. and T. N. Lee (1979), Wind induced circulation on the Georgia shelf, (winter 1976/77) RSMAS Tech Rep. 79003, Univ. of Miami, Miami, Fla.

Traynum, S. and R. Styles (2008), Exchange flow between two estuaries connected by a shallow tidal channel, J. Coastal Res., 24(5), 1260-1268, doi:10.2112/07-0840r.1.

Weber, A. H., and J. O. Blanton (1980), Monthly mean wind fields for the South Atlantic Bight, J. Phys. Oceanogr., 10 (8), 1256{1263, doi:10.1175/1520-0485(1980)010<1256:MMWFFT>2.0.CO;2.

Zhao, L., C. Chen, J. Vallino,C. Hopkinson, R. C. Beardsley, H. Lin, and J. Lerczak (2010), Wetland-estuarine-shelf interactions in the Plum Island Sound and Merrimack River in the Massachusetts coast, J. Geophys. Res., 115, C10039, doi:10.1029/2009JC006085.

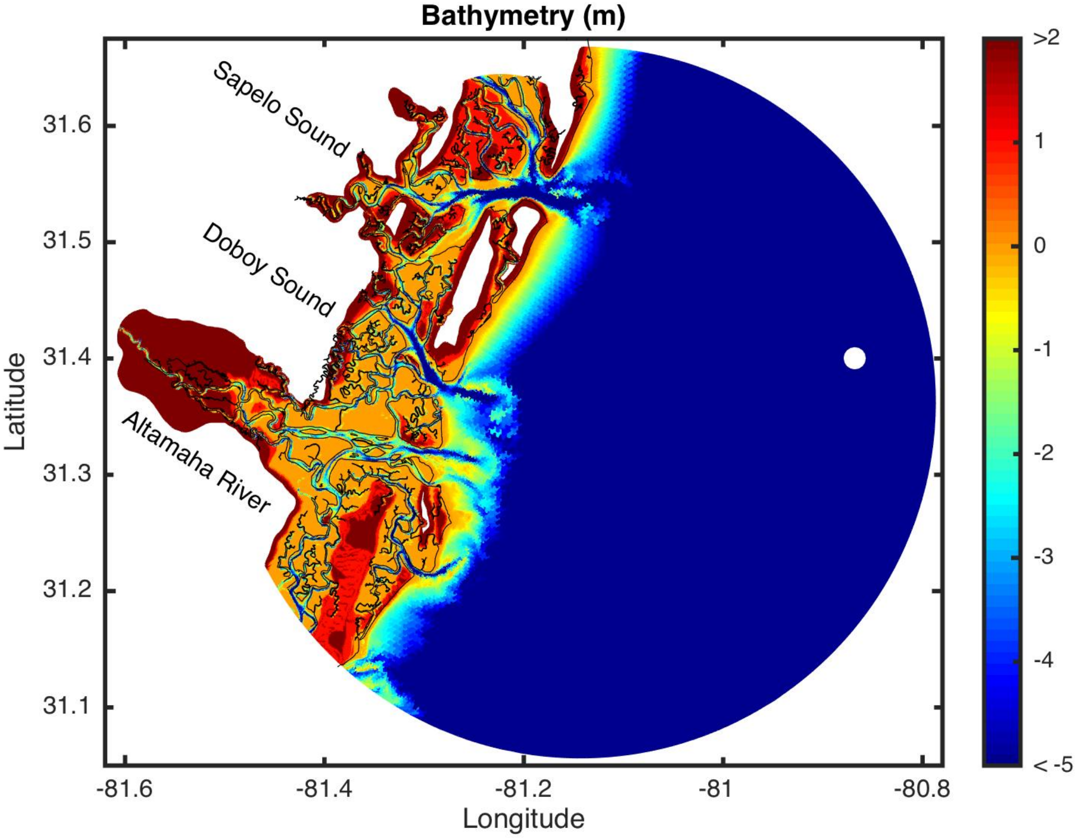

Figure 5.1 – Model domain with bottom topography (m). White circle offshore indicates the location of NOAA National Data Buoy Center buoy 41008 where wind measurements were obtained.

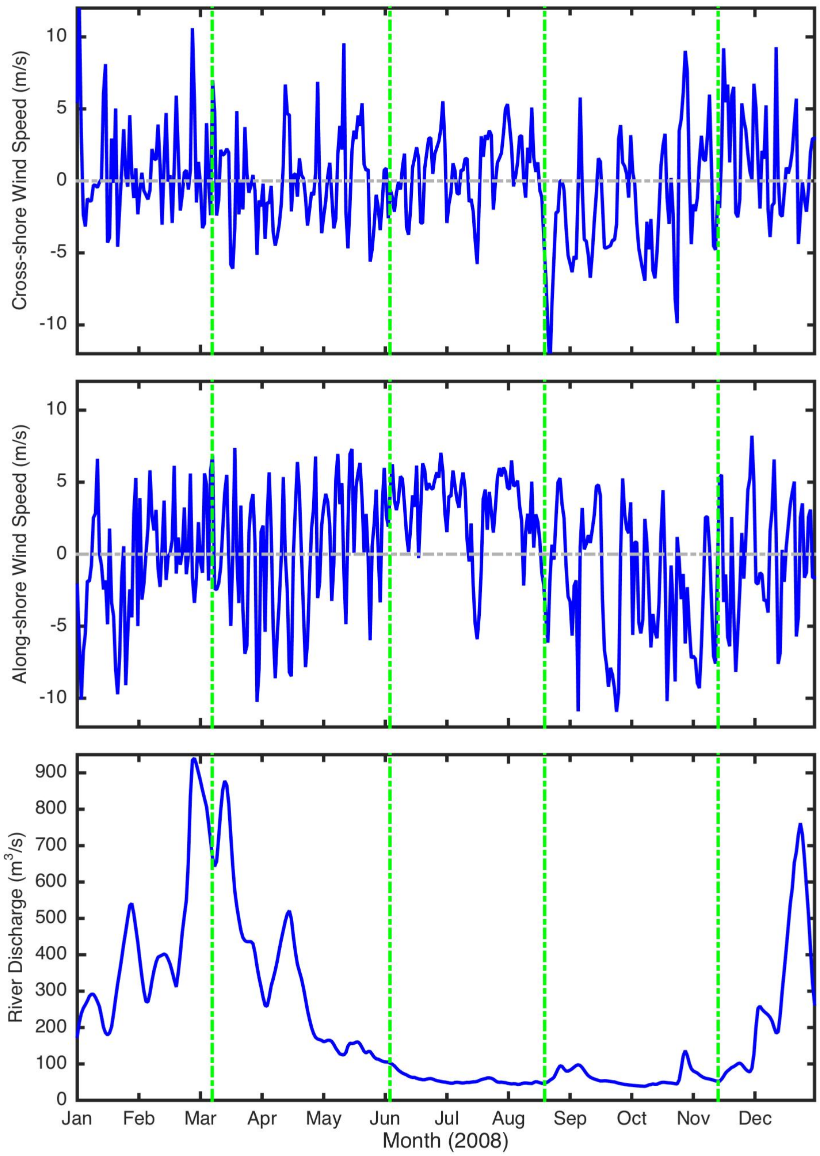

Figure 5.2 – Time series of (top) cross-shelf and (middle) alongshelf wind speed and of (bottom) river discharge during 2008. Vertical green lines indicate the timing of Lagrangian particle releases in the model.

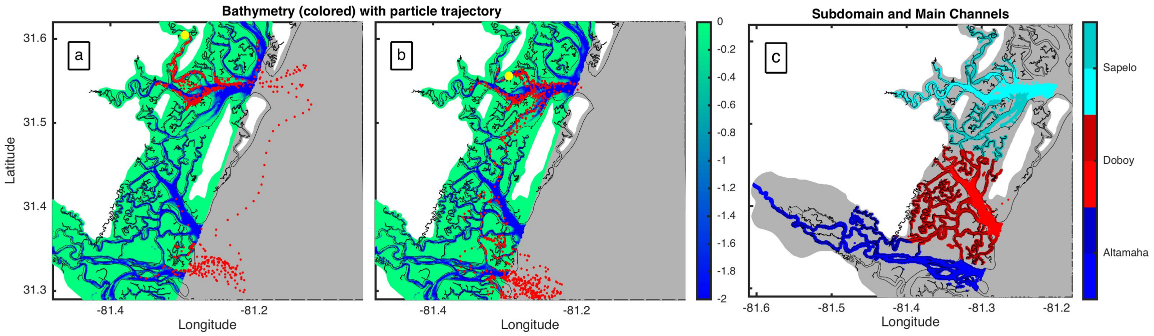

Figure 5.3 – Example of the trajectory of one particle (red dots) released at Sapelo Sound in mid-August that was connected to the other subdomains via the (a) oceanic or (b) marsh pathways. Yellow dot shows location of particle release. No particle was released in the area shown in gray. (c) Delineation of the different subdomains: Altamaha River (blue), Doboy Sound (red) and Sapelo Sound (cyan). Main channels are indicated by lighter colors.

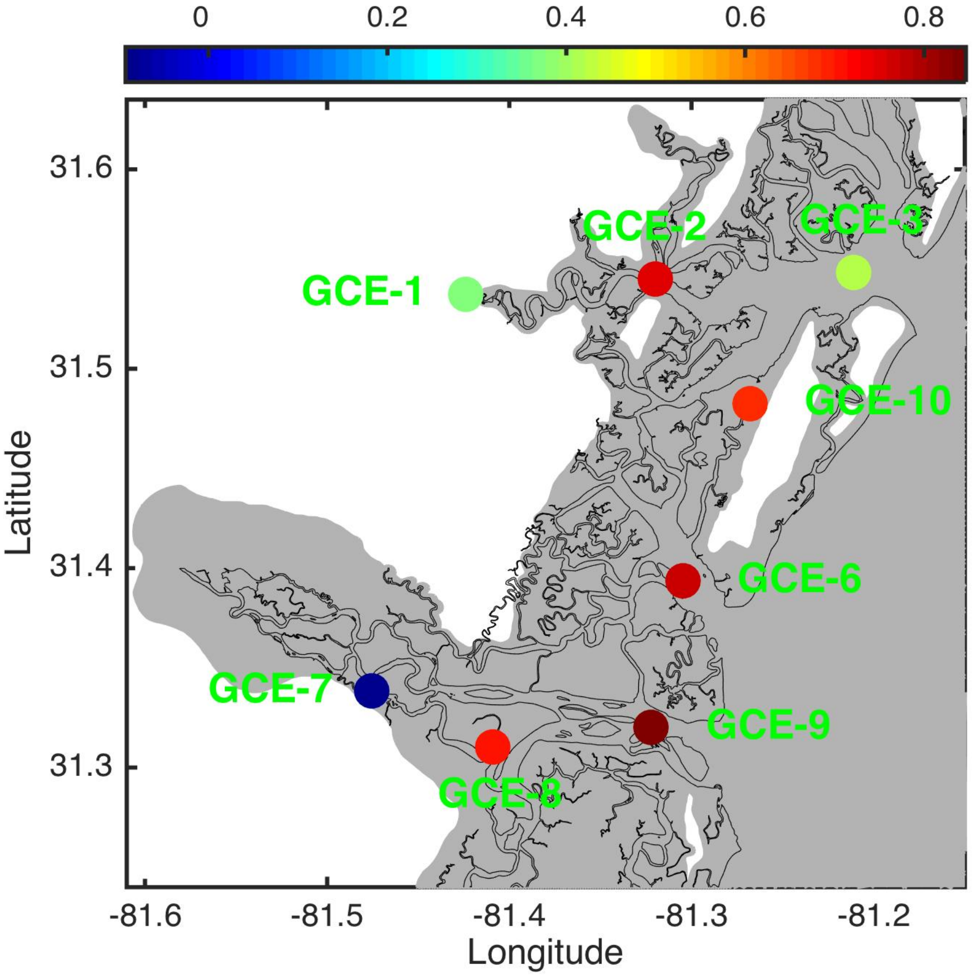

Figure 5.4 – Correlation coefficients between modeled and observed salinity at GCE-LTER stations.

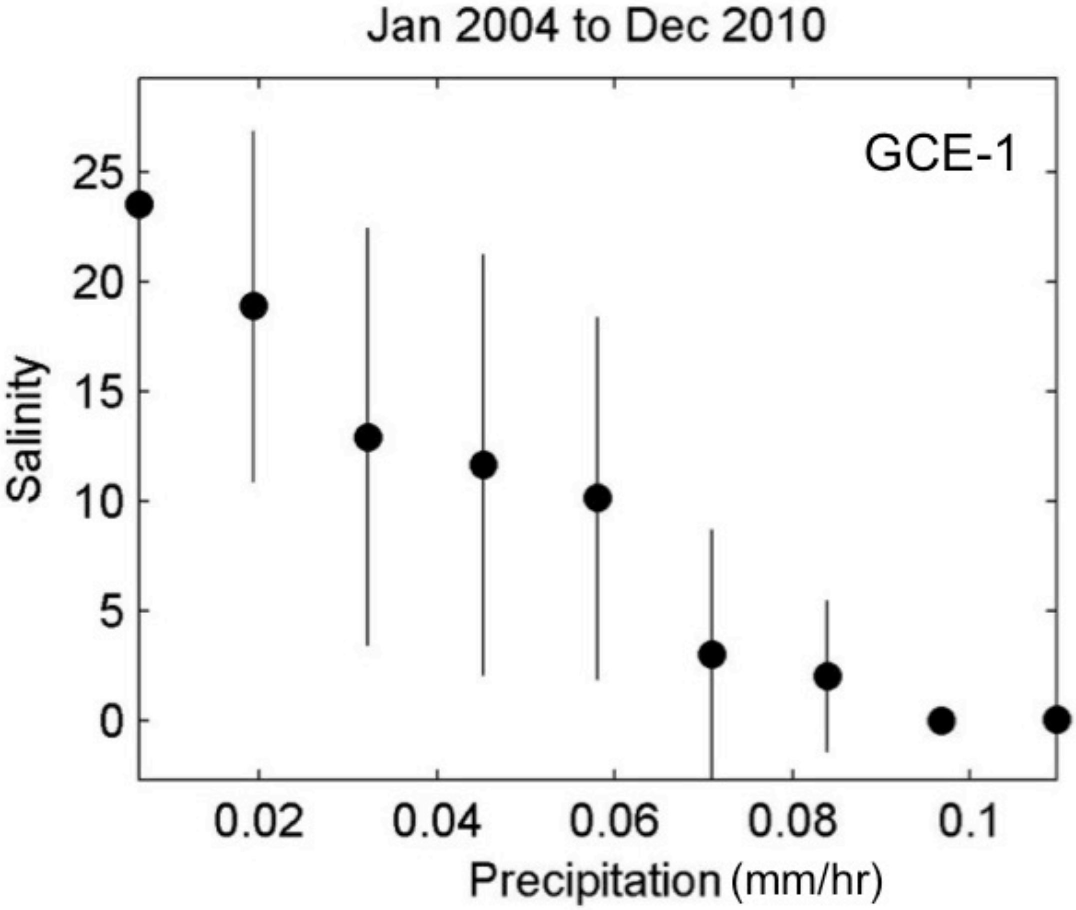

Figure 5.5 – Binned scatterplot of precipitation (measured near GCE-6, see Figure 5.4 for location) and salinity near the head of Sapelo Sound (GCE-1, see Figure 5.4 for location). Precipitation data was convoluted with a one-sided, exponentially decaying filter (*Castelao et. al*, 2008) with a decay scale of 2 months.

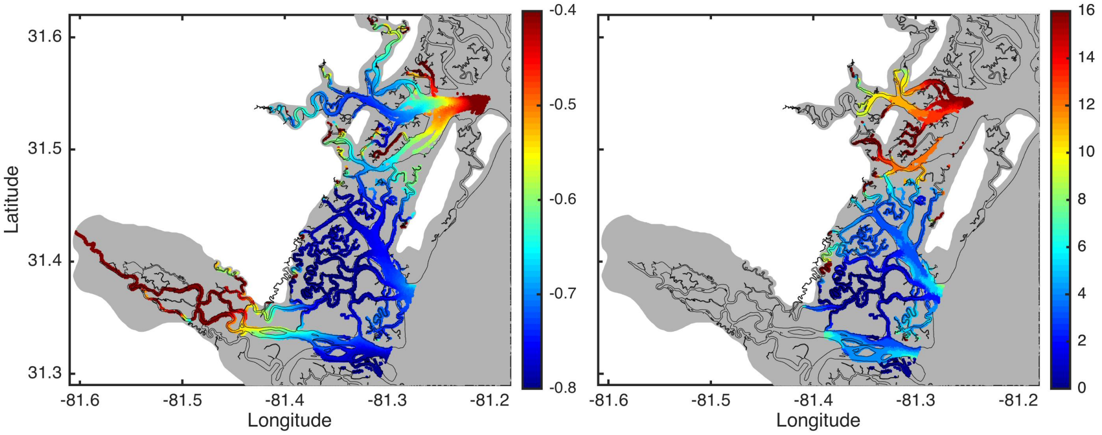

Figure 5.6 – (left) Correlation and (right) time lag between river discharge and salinity over the estuary. Time lags at locations where the correlation is not statistically significant are not shown.

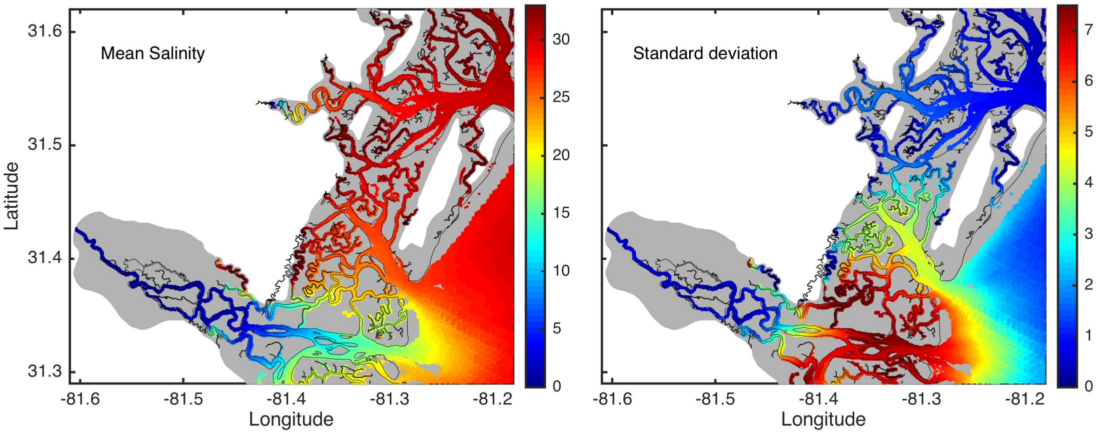

Figure 5.7 – (left) Average and (right) standard deviation of salinity over the domain.

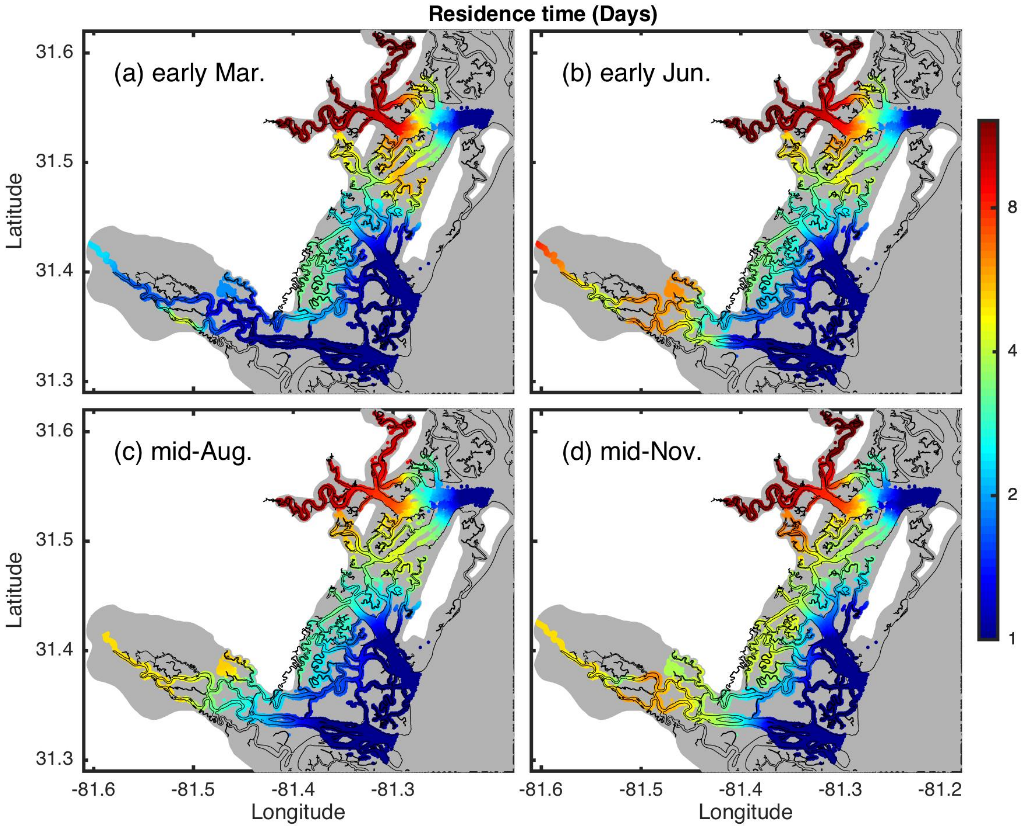

Figure 5.8 – Maps of local residence time for early March, early June, mid-August and mid-November, respectively. A logarithmic color scale is used to reveal as much as possible of the spatial structure.

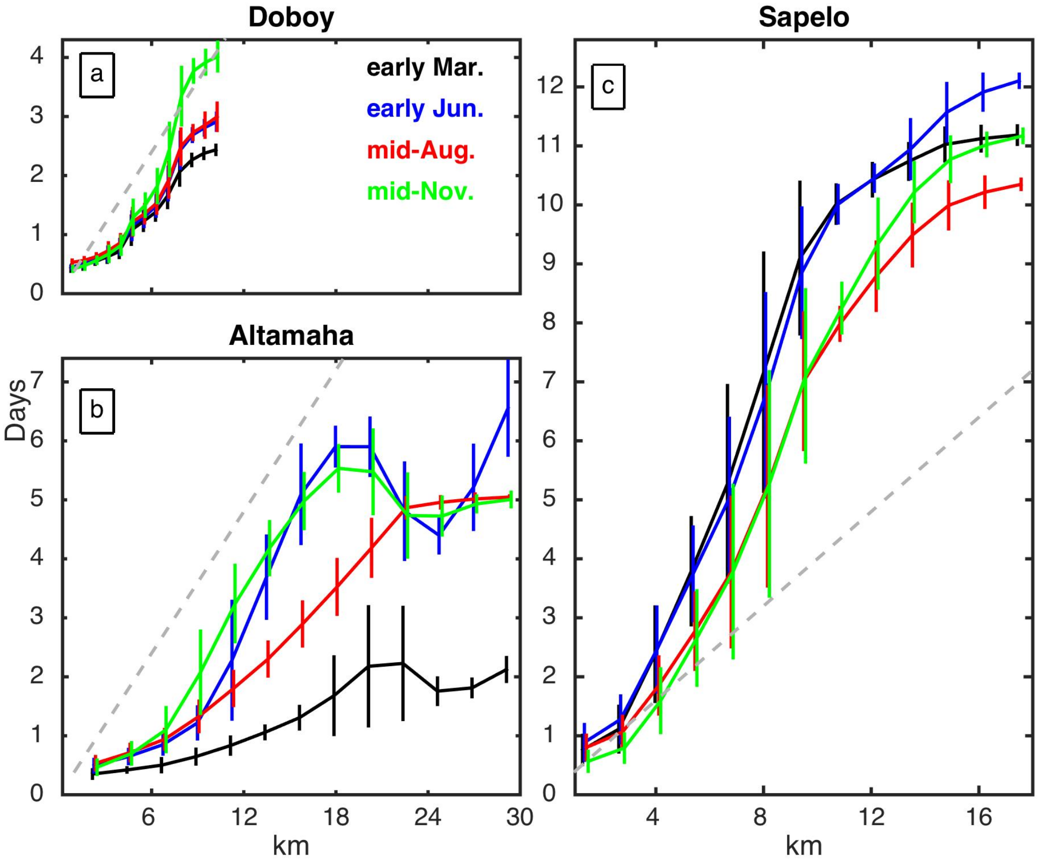

Figure 5.9 – Local residence time average along the main channels (see figure 5.3c for channel delineation) of Doboy Sound (a), Altamaha River (b) and Sapelo Sound (c) in different seasons as a function of distance from the mouth. A gray dashed line with the same slope is plotted in all panels for reference.

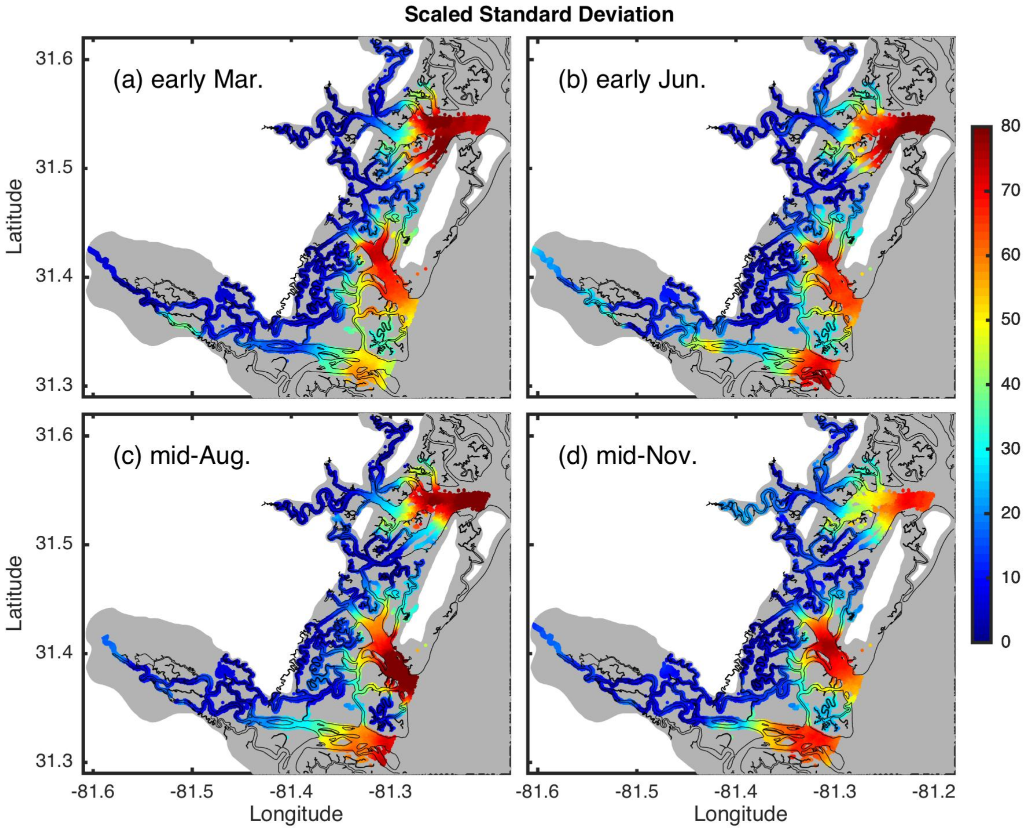

Figure 5.10 – Maps of the ratio between the standard deviation of the local residence time among the six particle release experiments at different phases of the tidal cycle and the respective average residence time in each season. Values have been multiplied by 100.

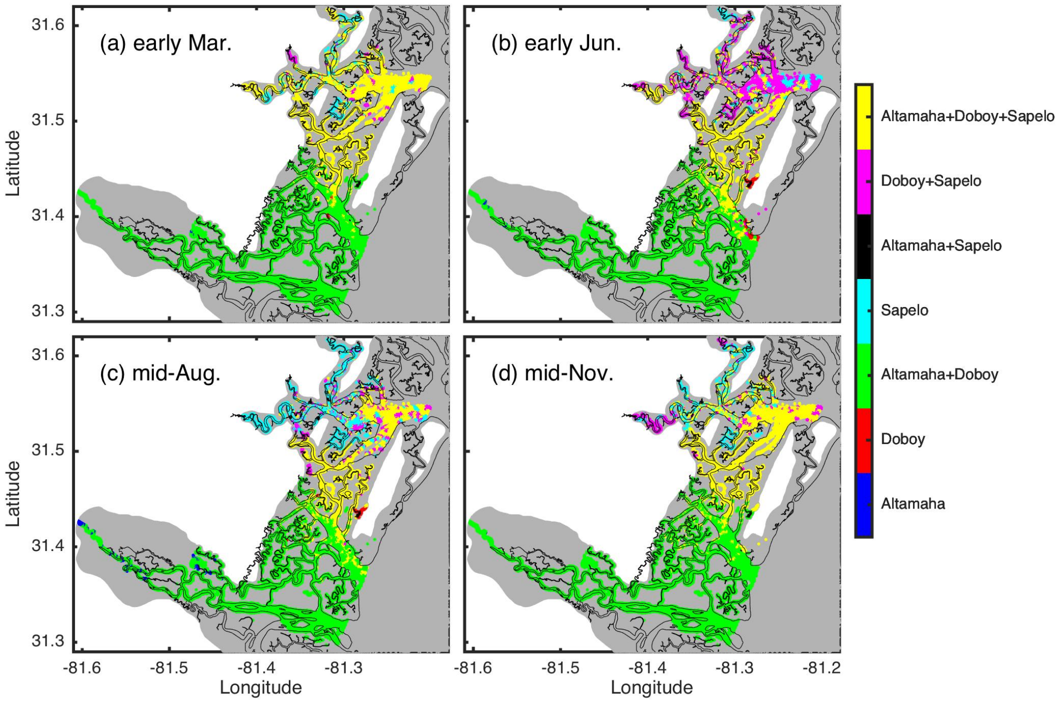

Figure 5.11 – Maps of connectivity in each season.

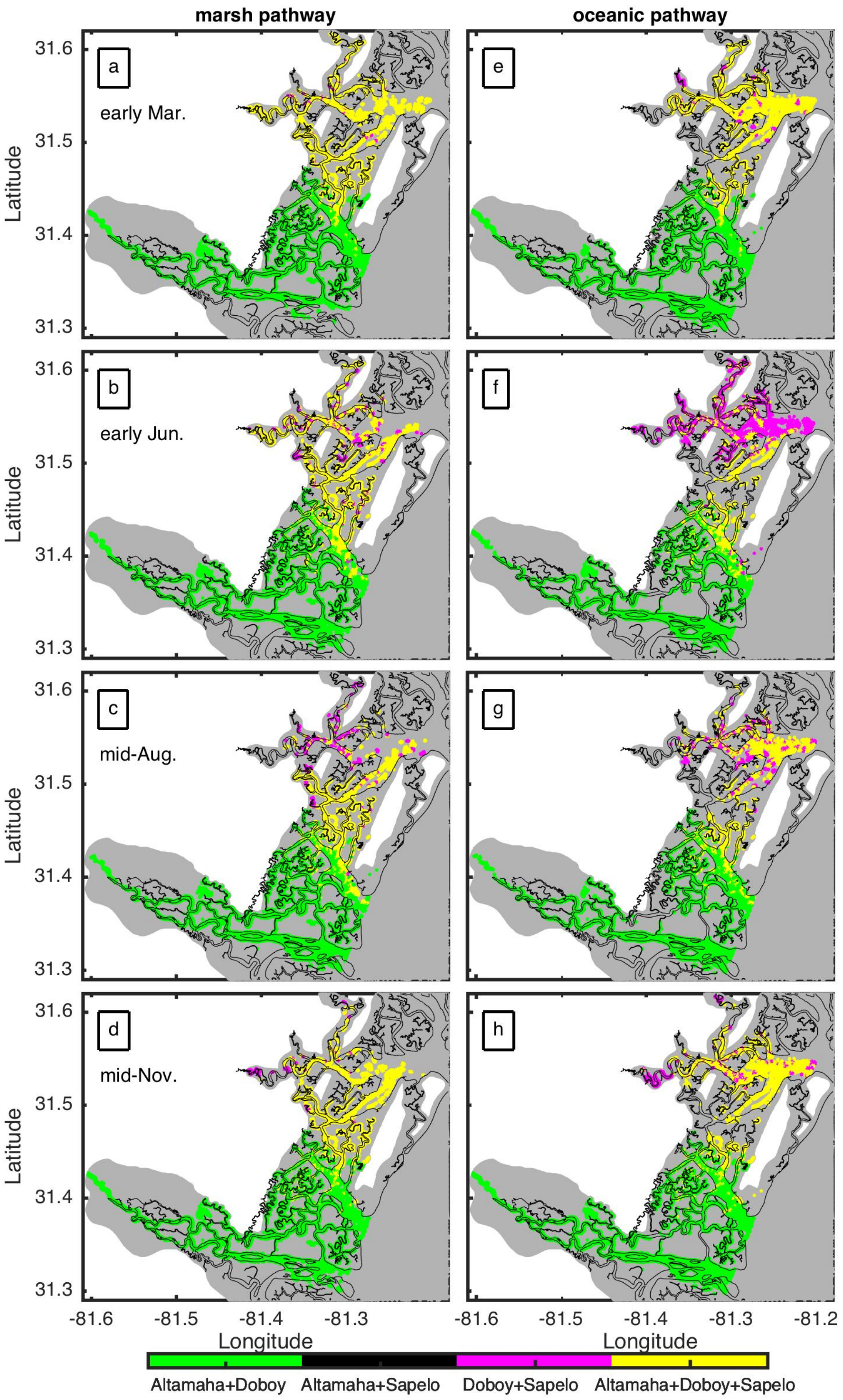

Figure 5.12 – Maps of transport pathways in the system. Marsh pathway is shown on the left, while oceanic pathway for each season is shown on the right.

CHAPTER 6

SUMMARY

Sea surface temperature fronts are important features separating water masses with different characteristics in the ocean. As a result, the distribution and dynamics of ocean fronts have received a great deal of attention from the oceanographic community. Fronts are generally associated with strong currents and high biological productivity, having a large importance for both ocean circulation and ecosystem processes. Fronts are also regions characterized by a tight coupling with the atmosphere. While upwelling favorable winds can play an important role on the formation of fronts in coastal systems (e.g., Castelao and Wang, 2014), for example, fronts can also feedback into the atmosphere, resulting in large modifications of the winds blowing over those areas (Chelton et al., 2001). As winds are modified, wind stress curl-driven upwelling or downwelling often modifies the distribution of temperature itself [Pickett and Paduan, 2003], resulting in strong coupling between the oceanic and atmospheric responses.

A general introduction to SST fronts is presented in chapter 2, including the physical processes of frontal formation and possible implications for biological processes. Although much has been learned over the last decades, especially with the advance of satellite observations, a severe limitation in our understanding of front activity is the lack of satellite observations very near the coast. As the resolution of satellite observations of SST and winds improve, so will our ability to investigate the evolution of SST fronts in these dynamic and active environments.

In chapter 3, SST fronts in Eastern Boundary Current Systems (EBCS) are investigated using seven years of satellite observations. Analyses reveal that the mean frontal probability is generally high near the coast, especially around major capes, decreasing with distance offshore. A substantial difference in the width of the band of high frontal probability near the coast is observed between the regions, being larger in the California and Benguela Current System compared to the other EBCS. Topographic perturbations, eddy activity and wind stress are all found to be important to determine the area with strong frontal activity. Empirical orthogonal function decompositions are used to capture the dominant patterns of spatial and temporal variability of frontal probability in the systems. Substantial seasonal variability in frontal probability is observed in all Eastern Boundary Current Systems, with the corresponding magnitude of the seasonal cycle being enhanced near the coast and around major capes. An offshore migration of the band characterized by high frontal activity is generally observed, as fronts are initially generated near the coast, subsequentially moving offshore. Seasonal enhancement in front activity generally occurs during summer at mid-latitudes. Comparisons with wind data reveal that variability in alongshelf wind stress and frontal probability are highly consistent to each other. Significant correlation between anomalies in front activity and in the intensity of upwelling favorable winds support the interpretation that coastal winds play a dominant role controlling the distribution of SST fronts in Eastern Boundary Current Systems.

Although a clear relationship between alongshore wind stress and SST frontal activity is revealed by the analyses, there are other factors that can contribute to variability in front activity that are not fully addressed in chapter 3. Latitudinal extent (and the associated variability in the Coriolis parameter), coastline orientation, bottom topography perturbations, eddy activity and the vertical structure of the density field are all likely to influence variability in frontal activity. Many of these processes are tightly coupled to each other. For example, strong winds can generate strong alongshore upwelling jets that can become unstable as they interact with topography perturbations, generating mesoscale eddies. Disentangling these processes may be best achieved via idealized simulations using a hydrodynamic model.

The interaction between sea surface temperature and wind stress over the global coastal ocean is discussed in chapter 4. SST gradients and wind stress fields are tightly coupled in the coastal ocean, being highly correlated to each other in regions with strong fronts. Mid-latitude regions, in particular, present strong correlations that extend farther from the coast in Western Boundary Current compared to Eastern Boundary Currents. The strength of the coupling is quantified using coupling coefficients, defined as the slope of the regression between crosswind SST gradient and wind stress curl and between downwind SST gradient and wind stress divergence. Seven years of satellite observations are used to obtain time series of coupling coefficients at monthly intervals. A clear pattern emerges of stronger coupling at mid-latitudes, which are progressively reduced toward low or high latitudes, creating an M-shape in the meridional direction. Strong mean coupling coefficients are observed in Eastern and Western Boundary Current Systems and off the Arabian Peninsula. Those regions are also associated with large amplitudes of the seasonal cycle and strong seasonal variability of coupling coefficients. Variability in coupling coefficients at the intraseasonal band tends to be more important in regions characterized by high eddy activity, especially in Western Boundary Currents. The average and the amplitude of the seasonal cycle are consistently larger for the divergence field compared to the curl field. Intraseasonal variability, on the other hand, is particularly important for the curl field. The use of consistent data sets in this study allowed for the generation of an atlas of temporal and spatial variability in the strength of the interaction in coastal regions throughout the globe. This atlas can be particularly useful to guide coastal studies, especially modeling investigations.

A general feature observed is that interannual variability in coupling coefficients is small, except for a few isolated locations. Although that may be true, the reliability of that result is possibly impacted by the relatively short time series available, since a seven-year long time series is still too short to confidently quantify variability at interannual scales. As additional data are collected and longer time series of SST and wind stress are gathered, it will be possible to further constrain the importance of interannual variability in coupling coefficients in coastal systems.

Variability in salinity was also investigated, focusing on coastal Georgia. The Altamaha River, Doboy Sound and Sapelo Sound form a complex estuarine system, interconnected by a network of creeks, channels and intertidal areas. Using a high-resolution coastal ocean model forced by tides, river discharge and winds, variability in salinity and water exchange is investigated in chapter 5. Modeled and observed salinity collected as part of the Georgia Coastal Ecosystem Long Term Ecological Research program are significantly correlated over the majority of the model domain. Spatial maps of correlation between river discharge and salinity reveals the spatial influence of river discharge on salinity variability in the estuarine complex. The relationship is strong in the Altamaha River and Doboy Sound, decreasing sharply toward Sapelo Sound farther away from the river. Tracking Lagraging particles in the model indeed reveals that although connectivity between the Altamaha River and Doboy Sound is very large in all seasons, connectivity with Sapelo Sound farther north is substantially reduced. As such, freshwater introduced into the system via the Altamaha River will have a larger impact in the river itself and at Doboy, but a reduced impact at Sapelo Sound.

Lagrangian particle tracking is also used to quantify the spatially- and seasonally-varying residence time in the system for the first time. There is a general tendency for the residence times to increase with increasing distance from the ocean during all seasons, which is modulated by variability in river discharge, especially in the Altamaha River. Quantifying the residence time for 177,796 regions along the estuary (i.e., at each node in the model grid) provides an unprecedented view of estuary-shelf exchange in the system, however. In particular, creeks and channels around Sapelo Sound are characterized by substantially larger residence time than other areas of the domain. Localized increases are also observed to the southwest of the main channel of Doboy Sound. The highly spatially variable residence time in the system suggests that nutrient and/or pollutant inputs to the system can have very different fates in the estuary, depending on the location of their input.

Model analyses presented here focused in 2008, a year in which the discharge of the Altamaha River was close to the historical average. An additional model simulation representing the period 2012-2014 was also pursued, and results are currently being analyzed. That period is especially interesting, because Altamaha River discharge in 2012 was the lowest recorded since measurements began in 1931 (Medeiros et al., 2015). Since Medeiros et al. (2015) also showed that the frequency of low discharge conditions in the Altamaha River seems to have increased over the recent decades, quantifying variability and water exchange in a year characterized by a severe drought will be particularly relevant. How will residence time change in that scenario? Will connectivity between the different Sounds be affected? These and other questions await future study.

BIBLIOGRAPHY

Aguirre, C., Ó. Pizarro, P. T. Strub, R. Garreaud, and J. A. Barth (2012), Seasonal dynamics of the near-surface alongshore flow off central Chile, *J. Geophys. Res.*, *117*, C01006, doi:10.1029/2011JC007379.

Aikman, F.A., and L. W. J. Lanerolle (2004), Report on the National Ocean Service Workshop on Residence/Flushing Times in Bays and Estuaries, NOAA Office of Coast Survey, Silver Spring, MD (http://www.nauticalcharts.noaa.gov/csdl/residencetime.html).

Alber, M., and J. E. Sheldon (1999a), Use of a data-specific method to examine variability in the flushing times of Georgia estuaries, *Estuarine Coastal Shelf Sci., 49,* 469–482.

Alber, M., and J. E. Sheldon (1999b), Trends in salinities and flushing times of Georgia estuaries. Pages 528–531 in K. J. Hatcher, editor. *Proceedings of the 1999 Georgia Water Resources Conference.* University of Georgia, Athens.

Albert, A., V. Echevin, M. Lévy, and O. Aumont (2010), Impact of nearshore wind stress curl on coastal circulation and primary productivity in the Peru upwelling system, *J. Geophys. Res.*, *115*, C12033, doi:10.1029/2010JC006569.

Allen, J. S., P. A. Newberger, and J. Federiuk (1995), Upwelling circulation on the Oregon continental shelf. Part I: Response to idealized forcing, *J. Phys. Oceanogr.*, *25*, 1843–1866, doi: http://dx.doi.org/10.1175/1520-0485(1995)025<1843:UCOTOC>2.0.CO;2

Alpine, A. E., and J. E. Cloern (1992), Trophic interactions and direct physical effects control phytoplankton biomass and production in an estuary, *Limnol. Oceanogr., 37*, doi: 10.4319/lo.1992.37.5.0946.

Arístegui, J., E. D. Barton, X. A. Álvarez-Salgado, A. M. P. Santos, F. G. Figueiras, S. Kifani, S. Hernández-León, E. Mason, E. Machú, and H. Demarcq (2009), Sub-regional ecosystem variability in the Canary Current upwelling, *Prog. Oceanogr.*, *83*, 33-48, doi:10.1016/ j.pocean.2009.07.031.

Armstrong, E., G. Wagner, J. Vazquez-Cuervo, and T. Chin (2012), Comparisons of regional satellite sea surface temperature gradients derived from MODIS and AVHRR sensors, Intern. *J. Rem. Sensing, 33*, 6639-6651.

Arthur, R. S. (1965), On the calculation of vertical motion in eastern boundary currents from determinations of horizontal motion, *J. Geophys. Res.*, *70*(12), 2799–2803, doi:10.1029/JZ070i012p02799.

Bakun, A., and C. S. Nelson (1977), Climatology of upwelling related processes off Baja California, *Calif. Coop. Oceanic Fish. Invesr. Rep. 19.*107-127.

Bakun, A., and C. S. Nelson (1991), The seasonal cycle of wind-stress curl in subtropical eastern boundary current regions, *J. Phys. Oceanogr.*, *21*, 1815–1834, doi: http://dx.doi.org/10.1175/1520-0485(1991)021<1815:TSCOWS>2.0.CO;2

Bakun, A., D. B. Field, A. N. A. Redondo-Rodriguez, and S. J. Weeks (2010), Greenhouse gas, upwelling-favorable winds, and the future of coastal ocean upwelling ecosystems, *Glob. Change Biol.*, *16*, 1213–1228. doi: 10.1111/j.1365-2486.2009.02094.x

Barth, J. A. (1989a), Stability of a coastal upwelling front: 1. Model development and a stability theorem, *J. Geophys. Res., 94*(C8), 10844–10856, doi:10.1029/JC094iC08p10844.

Barth, J. A. (1989b), Stability of a coastal upwelling front: 2. Model results and comparison with observations, *J. Geophys. Res., 94*(C8), 10857–10883, doi:10.1029/JC094iC08p10857.

Barber, R. T. and W. O. Smith (1981), The role of circulation, sinking, and vertical migration in physical sorting of phytoplankton in the upwelling center at 15°S, in *Coastal Upwelling*, edited by F. A. Richards, pp. 366-371, AGU, Washington, D. C.

Barth, J. A., and R. L. Smith (1998), Separation of a coastal upwelling jet at Cape Blanco, Oregon, USA, *S. Afr. J. Mar. Sci., 19,* 5– 14.

Barth, J., B. Menge, J. Lubchenco, F. Chan, J. Bane, A. Kirincich, M. McManus, K. Nielsen, S. Pierce, and L. Washburn (2007), Delayed upwelling alters nearshore costal ocean ecosystems in the northern California current, Proc. *Nat. Acad. Sci., 104,* 3719-3724.

Barth, J. A., S. D. Pierce, and R. L. Smith (2000), A separating coastal upwelling jet at Cape Blanco, Oregon and its connection to the California Current System, *Deep Sea Res. Part II.*, *47*(5–6), 783-810, doi: http://dx.doi.org/10.1016/S0967-0645(99)00127-

7.

Barth, J. A., S. D. Pierce, and T. J. Cowles (2005), Mesoscale structure and its seasonal evolution in the northern California Current System, *Deep Sea Res., Part II, 52,* 5–28.

Batteen, M. L. (1997), Wind-forced modeling studies of currents, meanders, and eddies in the California Current System, *J. Geophys. Res., 102*(C1), 985 – 1010.

Belkin, I. M., and J. E. O'Reilly (2009), An algorithm for oceanic front detection in chlorophyll and SST satellite imagery. *J. Marine Syst., 78*(3), 319-326.

Belkin, I. M., P. C. Cornillon, and K. Sherman (2009), Fronts in large marine ecosystems. *Prog. Oceanogr., 81*(1), 223-236.

Blanton, B. O., A. Aretxabaleta, F. E. Werner and H. E. Seim (2003), Monthly climatology of the continental shelf waters of the South Atlantic Bight. *J. Geophys. Res., Oceans, 108*(C8).

Blanton, J. O., and L. P. Atkinson (1983), Transport and fate of river discharge on the continental shelf of the southeastern United States, *J. Geophys. Res., 88,* 4730-4738.

Bograd, S. J., D. G. Foley, F. B. Schwing, C. Wilson, R. M. Laurs, J. J. Polovina, and R. E. Brainard (2004), On the seasonal and interannual migrations of the transition zone chlorophyll front, *Geophys. Res. Lett., 31*(17).

Bowen, M. M., J. L. Wilkin and W. J. Emery (2005), Variability and forcing of the East Australian Current, *J. Geophys. Res., 110*, C03019, doi:10.1029/2004JC002533.

Bowman, M. J. (1978), Oceanic fronts in coastal processes, in Oceanic Fronts in Coastal Processes, edited by M. Bowman and W. Esias, pp. 2– 5, Springer, New York.

Bowman, M. J., and R. L. Iverson (1978), Estuarine and plume fronts, in *Oceanic fronts in coastal processes*, edited by M. J. Bowman and W. E. Esaias, pp. 87-104, Springer Berlin Heidelberg

Bruce, J. G., D. R. Johnson, and J. C. Kindle (1994), Evidence for eddy formation in the eastern Arabian Sea during the northeast monsoon, *J. Geophys. Res., 99*(C4), 7651–7664, doi:10.1029/94JC00035.

Breaker, L. C., and C. N. K. Mooers (1986), Oceanic variability off the Central California coast, *Prog. Oceanogr.*, *17*(1), 61-135, doi: http://dx.doi.org/10.1016/0079-6611(86)90025-X.

Breaker, L. C., E. M. Armstrong, and C. A. Endris (2010), Establishing an objective basis for image compositing in satellite oceanography, *Rem. Sens. Env., 114,* 345-362.

Brink, K. H., R. C. Beardsley, J. Paduan, R. Limeburner, M. Caruso, and J. G. Sires (2000), A view of the 1993– 1994 California Current based on surface drifters, floats, and remotely sensed data, *J. Geophys. Res., 105*(C4), 8575– 8604.

Canny, J. (1986), A computational approach to edge detection, *IEEE Trans. Pattern Anal. Mach. Intell.*, *6*, 679–698. doi:10.1109/TPAMI.1986.4767851.

Capet, X., J. C. McWilliams, M. J. Molemaker, A. F. Shchepetkin (2008a), Mesoscale to Submesoscale Transition in the California Current System. Part I: Flow Structure, Eddy Flux, and Observational Tests, *J. Phys. Oceanogr., 38,* 29–43.

Capet, X., J. C. McWilliams, M. J. Molemaker, and A. F. Shchepetkin (2008b), Mesoscale to submesoscale transition in the California Current System. Part II:

Frontal processes, *J. Phys. Oceanogr., 38,* 44–64.

Capet, X., J. C. McWilliams, M. J. Molemaker, A. F. Shchepetkin (2008c), Mesoscale to Submesoscale Transition in the California Current System. Part III: Energy Balance and Flux, *J. Phys. Oceanogr., 38,* 2256–2269.

Carr, M.-E., and E. J. Kearns (2003), Production regimes in four eastern boundary current systems, *Deep Sea Res. Part II*, *50*(22-26), 3199-3221, doi: http://dx.doi.org/10.1016/j.dsr2.2003.07.015.

Castelao, R. (2011), Intrusions of Gulf Stream waters onto the South Atlantic Bight shelf, *J. Geophys. Res., 116,* C10011, doi:10.1029/2011JC007178.

Castelao, R. M. (2012), Sea surface temperature and wind stress curl variability near a cape, *J. Phys. Oceanogr., 42*(11), 2073-2087.

Castelao, R. M., and J. A. Barth (2005), Coastal ocean response to summer upwelling favorable winds in a region of alongshore bottom topography variations off Oregon, *J. Geophys. Res., 110,* C10S04.

Castelao, R. M., and J. A. Barth (2006), The relative importance of wind strength and alongshelf bathymetric variations on the separation of a coastal upwelling jet, *J. Phys. Oceanogr., 36*, 412-425.

Castelao, R. M., and J. A. Barth (2007), The role of wind stress curl in jet separation at a cape, *J. Phys. Oceanogr., 37,* 2652-2671.

Castelao, R. M., and Y. Wang (2014), Wind-driven variability in sea surface temperature front distribution in the California Current System, *J. Geophys. Res.: Oceans*, *119*(3), 1861–1875, doi:10.1002/2013JC009531. See Appendix A.

Castelao, R. M., J. A. Barth, and T. P. Mavor (2005), Flow-topography interactions in the northern California Current System observed from geostationary satellite data, *Geophys. Res. Lett.*, *32*, L24612, doi:10.1029/2005GL024401.

Castelao, R., S. Glenn, O. Schofield, R. Chant, J. Wilkin and J. Kohut (2008), Seasonal evolution of hydrographic fields in the central Middle Atlantic Bight from glider observations, *Geophys. Res. Lett., 35*(3), L03617.

Castelao, R. M., T. P. Mavor, J. A. Barth, and L. C. Breaker (2006), Sea surface temperature fronts in the California Current System from geostationary satellite observations, *J. Geophys. Res.*, *111*, C09026, doi:10.1029/2006JC003541.

Cayula, J. F., and P. Cornillon (1992), Edge detection algorithm for SST images. *J. Atmos. Ocean Tech., 9*(1), 67-80.

Chai, F., M. Jiang, R. T. Barber, R. C. Dugdale, and Y. Chao (2003), Interdecadal variation of the transition zone chlorophyll front, a physical-biological model simulation between 1960 and 1990, *J. Oceanogr., 59,* 461 – 475.

Chaigneau, A., G. Eldin, and B. Dewitte (2009), Eddy activity in the four major upwelling systems from satellite altimetry (1992–2007), *Prog. Oceanogr.*, *83*(1-4), 117-123, doi: http://dx.doi.org/10.1016/j.pocean.2009.07.012.

Chavez, F. P., and M. Messié (2009), A comparison of eastern boundary upwelling ecosystems, *Prog. Oceanogr.*, *83*(1-4), 80-96, doi: http://dx.doi.org/10.1016/j.pocean.2009.07.032.

Chelton, D. B. (1982), Large-scale response of the California Current to forcing by the wind stress curl, *CalCOFI Rep., 23,* 130-148.

Chelton, D. B. (2013), Ocean-atmosphere coupling: Mesoscale eddy effects, *Nat. Geosci., 6*(8), 594–595, doi:10.1038/ngeo1906.

Chelton, D. B., and M. H. Freilich (2005), Scatterometer-based assessment of 10-m wind analyses from the operational ECMWF and NCEP numerical weather prediction models, *Mon. Wea. Rev.*, *133*(2), 409–429, doi: http://dx.doi.org/10.1175/MWR-2861.1

Chelton, D. B., and R. E. Davis (1982), Monthly mean sea-level variability along the west coast of North America, *J. Phys. Oceanogr.*, *12*(8), 757–784, doi: http://dx.doi.org/10.1175/1520-0485(1982)012<0757:MMSLVA>2.0.CO;2

Chelton, D.B., and S.-P. Xie (2010), Coupled ocean-atmosphere interaction at oceanic mesoscales. *Oceanography, 23*(4):52–69, doi:10.5670/oceanog.2010.05.

Chelton, D. B., M. G. Schlax, M. H. Freilich, and R. F. Milliff (2004), Satellite measurements reveal persistent small-scale features in ocean winds, *Science*, *303*(5660), 978-983. doi:10.1126/science.1091901.

Chelton, D. B., M. G. Schlax, and R. M. Samelson (2007), Summertime coupling between sea surface temperature and wind stress in the California Current System, *J. Phys. Oceanogr.*, *37*(3), 495–517, doi: http://dx.doi.org/10.1175/JPO3025.1.

Chelton, D., M. G. Schlax, and R. M. Samelson (2011), Global observations of nonlinear mesoscale eddies, *Progr. in Oceanogr., 91*, 167-216.

Chelton, D.B., M. H. Freilich, and S. K. Esbensen (2000), Satellite observations of the wind jets off the Pacific coast of Central America. Part II: Regional relationships and Dynamical Considerations, *Mon. Wea. Rev. 128*, 2019-2043.

Chelton, D. B., R. L. Bernstein, A. Bratkovitch, and P. M. Kosro (1987), The central California coastal circulation study, *Eos Trans. AGU, 68,* 12– 13.

Chelton, D. B., S. K. Esbensen, M. G. Schlax, N. Thum, M. H. Freilich, F. J. Wentz, C. L. Gentemann, M. J. McPhaden, and P. S. Schopf (2001), Observations of coupling between surface wind stress and sea surface temperature in the eastern tropical Pacific, *J. Climate, 14*(7), 1479-1498.

Chen, C., G. Cowles, and R. C. Beardsley (2006a), An unstructured grid, finite-volume coastal ocean model: FVCOM user manual, 2nd ed.,SMAST/UMASSD Tech. Rep. 06-0602, 315 pp., School for Marine Science and Technology, University of Massachusetts-Dartmouth, New Bedford, MA.

Chen, C., R. C. Beardsley, and G. Cowles (2006b), An unstructured grid, finite-volume coastal ocean model (FVCOM) system: Special Issue entitled "Advances in Computational Oceanography", *Oceanography, 19*(1),78–89.

Chen, C., H. Huang, R. C. Beardsley, H. Liu, Q. Xu, and G. Cowles (2007), A finite-volume numerical approach for coastal ocean circulation studies: Comparisons with finite-difference models, *J. Geophys. Res., 112,* C03018, doi:10.1029/2006JC003485.

Chen, C., J. Qi, C. Li, R. C. Beardsley, H. Lin, R. Walker, and K. Gates (2008), Complexity of the flooding/drying process in an estuarine tidal-creek salt-marsh system: An application of FVCOM, *J. Geophys. Res., 113*, C07052.

Chen, Z., L. Wu, B. Qiu, S. Sun, and F. Jia (2014), Seasonal variation of the south equatorial current bifurcation off Madagascar, *J. Phys. Oceanogr., 44*, 618–631.

Church, T.M. (1986), Biogeochemical factors influencing the residence time of microconstituents in a large tidal estuary, Delaware Bay. *Mar. Chem., 18:* 393-406.

Collins, C. A. (1964), Structure and kinematics of the permanent oceanic front off the Oregon coast, M.S. thesis, Oregon State University.

Cromwell, T. and J. L. Reid (1956), A study of ocean fronts, *Tellus, 8,* 94-101.

Cropper, T. E., E. Hanna, and G. R. Bigg (2014), Spatial and temporal seasonal trends in coastal upwelling off Northwest Africa, 1981–2012, *Deep Sea Res. Part I*, *86*, 94-111, doi: http://dx.doi.org/10.1016/j.dsr.2014.01.007.

Desbiolles, F., B. Blanke, A. Bentamy, and N. Grima (2014), Origin of fine-scale wind stress curl structures in the Benguela and Canary upwelling systems, *J. Geophys. Res. Oceans, 119,* 7931–7948, doi:10.1002/2014JC010015.

Di Iorio, D., and K. R. Kang (2007), Variations of turbulent flow with river discharge in the Altamaha River Estuary, Georgia, *J. Geophys. Res., 112,* C05016.

Di Iorio, D., and R.M. Castelao (2013), The dynamical response of salinity to freshwater discharge and wind forcing in adjacent estuaries on the Georgia coast. *Oceanography 26*(3): 44–51, http://dx.doi.org/10.5670/oceanog.2013.44.

Dronkers, J. and J. T. F. Zimmerman (1982), Some principles of mixing in tidal lagoons. Oceanologica acta. Proceedings of the International Symposium on Coastal Lagoons, Bordeaux, France, 9–14 September, 1981, p. 107–117

Duarte A. A. L. S. and J. M. P. Vieira (2009), Effect of tidal regime on estuarine residence time spatial variation, In: Mastorakis N, Helmis C, Papageorgiou CD, Bulucea CA, Panago - poulos T (eds) Energy, environment, ecosystems, development and landscape architecture. WSEAS Press, p 240−245.

Echevin, V., O. Aumont, J. Ledesma, and G. Flores (2008), The seasonal cycle of surface chlorophyll in the Peruvian upwelling system: A modeling study, *Prog. Oceanogr., 79*,167–176.

Egbert, G. D. and S. Y. Erofeeva (2002), Efficient Inverse Modeling of Barotropic Ocean Tides, *J. Atmos. Oceanic Technol., 19,* 183–204. doi: http://dx.doi.org/10.1175/1520-0426(2002)019<0183:EIMOBO>2.0.CO;2

Ekman, V. W. (1905), On the influence of the Earth's rotation on ocean currents, *Arch. Math. Astron. Phys.*, *2*, 1-52.

Fanning, J. L. (2003), Water use in Georgia, 2000; and trends, 1950–2000, *Proceedings of 2003 Georgia Water Resources Conference,* Univ. of Georgia, Athens.

Fedorov, K. N. (1983), Physical nature and structure of oceanic fronts, Nauka, Leningrad.

Fedorov K.N. (1986), The Physical Nature and Structure of Oceanic Fronts, Springer-Verlag, Berlin etc., viii+333 pp.

Frenger, I., N. Gruber, R. Knutti, and M. Münnich (2013), Imprint of Southern Ocean eddies on winds, clouds and rainfall, *Nat. Geosci., 6*(8), 608–612, doi:10.1038/ngeo1863.

Gan, J., and J. S. Allen (2002), A modeling study of shelf circulation off northern California in the region of the Coastal Ocean Dynamics Experiment: Response to relaxation of upwelling winds, *J. Geophys. Res.*, *107*(C9), 3123, doi:10.1029/2000JC000768.

Garreaud, R., and R. C. Muñoz (2005), The Low-Level Jet off the West Coast of Subtropical South America: Structure and Variability, *Mon. Weather Rev., 133*(8), 2246-2261, doi:10.1175/MWR2972.1.

Garvine, R. W., and J. D. Monk (1974), Frontal structure of a river plume, *J. Geophys. Res., 79*(15), 2251-2259.

Geyer, W. R. (1997), Influence of wind on dynamics and flushing of shallow estuaries, *Estuarine Coastal Shelf Sci., 44,* 713–722.

Geyer, W. R. (2010), Estuarine salinity structure and circulation, in *Contemporary Issues in Estuarine Physics*, edit by A. Valle-Levinson, pp 12–26, Cambridge University Press.

Geyer, W. R., and P. MacCready (2014), The estuarine circulation, *Annual Review of Fluid Mechanics, 46*(1), 175.

Geyer, W. R., and R. Signell (1992), A reassessment of the role of tidal dispersion in estuaries and bays. *Estuaries 15:*97–108, http://dx.doi.org/10.2307/1352684.

Goni, G. J., S. Kamholtz, S. Garzoli, and D. B. Olson (1996), Dynamics of the Brazil–Malvinas confluence based upon inverted echo sounders and altimetry, *J. Geophys. Res., 101*(7), 16 273– 16 289.

Gruber, N., Z. Lachkar, H. Frenzel, P. Marchesiello, M. Münnich, J. C. McWilliams, T. Nagai, and G.-K. Plattner (2011), Eddy-induced reduction of biological production in eastern boundary upwelling systems, *Nature Geosci*, *4*(11), 787-792, doi: http://dx.doi.org/10.1038/ngeo1273.

Haack, T., D. Chelton, J. Pullen, J. D. Doyle, and M. Schlax (2008), Summertime Influence of SST on Surface Wind Stress off the US West Coast from the US Navy COAMPS Model, *J. Phys. Oceanogr., 38*(11), 2414-2437.

Haidvogel, D. B., A. Beckman, and K. Hedstrom (1991), Dynamical simulation of filament formation and evolution in the coastal transition zone, *J. Geophys. Res., 96,* 15,017 – 15,040.

Haney, R. L., R. A. Hale, and D. E. Dietrich (2001), Offshore propatation of eddy kinetic energy in the California Current, *J. Geophys. Res., 106*(C6), 11,709 – 11,717.

Hastenrath, S., and L. Greischar (1991), The monsoonal current regimes of the tropical Indian Ocean: Observed surface flow fields and their geostrophic and wind-driven components, *J. Geophys. Res., 96*(C7), 12619–12633, doi:10.1029/91JC00997.

Haynes, R., E. D. Barton, and I. Pilling (1993), Development, persistence, and variability of upwelling filaments off the Atlantic coast of the Iberian Peninsula, *J. Geophys. Res.*, *98*(C12), 22681–22692, doi:10.1029/93JC02016.

Hickey, B. M. (1979), The California Current System: Hypotheses and facts, *Prog. Oceanogr., 8,* 191– 279.

Hickey, B. M. (1989), Patterns and processes of circulation over the shelf and slope, in

Coastal Oceanography of Washington and Oregon, edited by M. R. Landry and B. M. Hickey, pp. 41 – 109, Elsevier, New York.

Hickey, B. M. (1998), Coastal oceanography of western North America from the tip of Baja California to Vancouver Island, in The Sea, vol. 11, The Global Coastal Ocean Regional Studies and Syntheses, edited by A. R. Robinson and K. H. Brink, pp. 345–393, John Wiley, Hoboken, N. J.

Holladay, C. G., and J. J. O'Brien (1975), Mesoscale variability of sea surface temperature, *J. Phys. Oceanogr., 5,* 761–772.

Hsu, S. A., R. Fett and P. E. La Violette (1985), Variations in atmospheric mixing height across oceanic thermal fronts, *J. Geophys. Res., 90*(C2), 3211-3224.

Hutchings, L., et al. (2009), The Benguela Current: An ecosystem of four components, *Prog. Oceanogr.*, *83*(1-4), 15-32, doi: http://dx.doi.org/10.1016/j.pocean.2009.07.046.

Huyer, A. (1983), Coastal upwelling in the California Current system, *Prog. Oceanogr.*, *12*(3), 259-284, doi: http://dx.doi.org/10.1016/0079-6611(83)90010-1.

Huyer, A., E. Sobey, and R. Smith (1979), The spring transition in currents over the Oregon continental shelf, *J. Geophys. Res., 84,* 6695-7011.

Huyer, A., J. A. Barth, P. M. Kosro, R. K. Shearman, and R. L. Smith (1998), Upper-ocean water mass characteristics of the California current, Summer 1993, *Deep Sea Res., Part II, 45,* 1411– 1442.

Huyer, A., J. H. Fleischbein, J. Keister, P. M. Kosro, N. Perlin, R. L. Smith, and P. A. Wheeler (2005), Two coastal upwelling domains in the northern California Current system, *J. Mar. Res.*, *63*(5), 901-929, doi: http://dx.doi.org/10.1357/002224005774464238.

Izumo T., C. B. Montégut, J.-J. Luo, S. K. Behera, S., Masson and T. Yamagata (2008), The Role of the Western Arabian Sea Upwelling in Indian Monsoon Rainfall Variability, *J. Climate, 21*, 5603–5623, doi: http://dx.doi.org/10.1175/2008JCLI2158.1

Jiang, L., X.-H. Yan, Y.-H. Tseng, and L. C. Breaker (2011), A numerical study on the role of wind forcing, bottom topography, and nonhydrostacy in coastal upwelling, *Est. Coast. Shelf Sci., 95*(1), 99-109, doi:http://dx.doi.org/10.1016/j.ecss.2011.08.019.

Joyce, T. M. (1984), Velocity and hydrographic structure of a Gulf Stream warm core ring, *J. Phys. Oceanogr., 14*, 936–947, doi:10.1175/1520-0485(1984)014<0936:VAHSOA>2.0.CO;2.

Jury, M. R. (1994), A thermal front within the marine atmospheric boundary layer over the Agulhas Current south of Africa: Composite aircraft observations, *J. Geophys. Res.,99*(C2), 3297-3304.

Kahru, M., E. Di Lorenzo, M. Manzano-Sarabia, and B. G. Mitchell (2012), Spatial and temporal statistics of sea surface temperature and chlorophyll fronts in the California Current, *J. Plankton Res.*, *34*(9), 749-760, doi:10.1093/plankt/fbs010.

Kang, D., and E. N. Curchitser (2013), Gulf Stream eddy characteristics in a high-resolution ocean model, *J. Geophys. Res., 118*,4474–4487, doi:10.1002/jgrc.20318.

Kelly, K. A. (1983), Swirls and plumes of application of statistical methods of satellite-derived sea surface temperature, *CODE Tech. Rep. 18, Scripps Inst. of Oceanogr., La Jolla, Calif.*

Kelly, K. A., and S. Dong (2004), The relationship of western boundary current heat transport and storage to mid-latitude ocean–atmosphere interaction, Earth's Climate: The Ocean–Atmosphere Interaction, *Geophys. Monogr., 147*, A.G.U., 347–363.

Kelly, K. A., R. C. Beardsley, R. Limeburner, K. H. Brink, J. D. Paduan, and T. K. Chereskin (1998), Variability of the near-surface eddy kinetic energy in the California Current based on altimetric, drifter, and moored current data, *J. Geophys. Res., 103*(C6), 13,067– 13,083.

Kosro, P. M., and A. Huyer (1986), CTD and velocity surveys of seaward jets off northern California, July 1981 and 1982, *J. Geophys. Res., 91*, 7680 – 7690.

Kosro, P. M., et al. (1991), The structure of the transition zone between coastal waters and the open ocean off northern California, winter and spring 1987, *J. Geophys. Res., 96,* 14,707–14,730.

Kostianoy, A. G., and J. R. E. Lutjeharms (1999), Atmospheric effects in the Angola-Benguela frontal zone, *J. Geophys. Res.*, *104*(C9), 20963–20970, doi:10.1029/1999JC900017.

Kundu, P., J. Allen, and R. Smith (1975), Modal decomposition of the velocity field near the Oregon coast, *J. Phys. Oceanogr., 5*, 683-704.

Kwon, B. H., B. Bénech, D. Lambert, P. Durand, A. Druilhet, H. Giordani and S. Planton (1998), Structure of the marine atmospheric boundary layer over an oceanic thermal front: SEMAPHORE experiment, *J. Geophys. Res., 103*(C11), 25159-25180.

Large, W. G., J. C. McWilliams, and S. C. Doney (1994), Oceanic vertical mixing: A review and a model with a nonlocal boundary layer parameterization, *Rev. Geophys., 32*, 363–403.

Lathuilière, C., V. Echevin, and M. Lévy (2008), Seasonal and intraseasonal surface chlorophyll-a variability along the northwest African coast, *J. Geophys. Res.*, *113*, C05007, doi:10.1029/2007JC004433.

Lee, T. N. and D. A. Brooks (1979), Initial observations of current, temperature and coastal sea level response to atmospheric and Gulf Stream forcing on the Georgia shelf, *Geophys. Res. Lett., 6,* 321–324.

Legeckis, R. (1978), A survey of worldwide sea surface temperature fronts detected by environmental satellites, *J. Geophys. Res.*, *83*(C9), 4501–4522, doi:10.1029/JC083iC09p04501.

Legaard, K. L., and A. C. Thomas (2006), Spatial patterns in seasonal and interannual variability of chlorophyll and sea surface temperature in the California Current, *J. Geophys. Res., 111,* C06032, doi:10.1029/ 2005JC003282.

Legaard, K. R., and A. C. Thomas (2007), Spatial patterns of intraseasonal variability of chlorophyll and sea surface temperature in the California Current, *J. Geophys. Res., 112,* C09006, doi:10.1029/2007JC004097.

Lemagie, E. P., and J. A. Lerczak (2014), A comparison of bulk estuarine turnover timescales to particle tracking timescales using a model of the Yaquina Bay Estuary, *Estuaries Coasts, 38*(5), 1797-1814, doi:10.1007/s12237-014-9915-1.

Lentz, S. (2003), A climatology of salty intrusions over the continental shelf from Georges Bank to Cape Hatteras, *J. Geophys. Res., 108* (C10), 3326, doi:10.1029/2003JC001859.

Liang, J.-H., J. C. McWilliams, and N. Gruber (2009), High-frequency response of the ocean to mountain gap winds in the northeastern tropical Pacific, *J. Geophys. Res., 114,* C12005, doi:10.1029/2009JC005370.

Maloney, E. D., and D. B. Chelton (2006), An Assessment of the Sea Surface Temperature Influence on Surface Wind Stress in Numerical Weather Prediction and Climate Models, *J. Climate, 19,* 2743–2762. doi: http://dx.doi.org/10.1175/JCLI3728.1

Marchesiello, P., and P. Estrade (2009), Eddy activity and mixing in upwelling systems: a comparative study of Northwest Africa and California regions, *Int. J. Earth Sci.*, *98*(2), 299-308, doi: http://dx.doi.org/10.1007/s00531-007-0235-6.

Mavor, T. P., and J. J. Bisagni (2001), Seasonal variability of sea-surface temperature fronts on Georges Bank, *Deep Sea Research Part II*, *48*(1), 215-243, doi: http://dx.doi.org/10.1016/S0967-0645(00)00120-X.

McCreary, J.P. (1981), A linear stratified ocean model of the Coastal Undercurrent*, Phil. Trans. Roy. Soc. Lond., 302A*, 385-413.

McGregor, H. V., M. Dima, H. W. Fischer, and S. Mulitza (2007), Rapid 20th-century increase in coastal upwelling off northwest Africa, *Science*, *315*(5812), 637-639, doi:10.1126/science.1134839.

Medeiros, P. M., M. Seidel, T. Dittmar, W. B. Whitman, and M. A. Moran (2015), Drought-induced variability in dissolved organic matter compostion in a marsh-dominated estuary, *Geophys. Res. Lett., 42*(15), 6446-6453.

Menzel, D. W. (1993), Ocean processes: U.S. southeast continental shelf. A summary of research conducted in the South Atlantic Bight under the Auspices of the U.S. Department of Energy from 1977 to 1991, Publ. DOE/OSTl-11674, 112, Off. of Sci. and Tech. Inf., U.S. Dep. of Energy, Washington, D. C..

Mesias, J. M., R. P. Matano, and P. T. Strub (2001), A numerical study of the upwelling circulation off central Chile, *J. Geophys. Res., 106,* 19611–19623.

Mesias, J. M., R. P. Matano, and P. T. Strub (2003), Dynamical analysis of the upwelling circulation off central Chile*, J. Geophys. Res., 108,* 3085, doi:10.1029/2001JC001135.

Meunier, T., E. D. Barton, B. Barreiro, and R. Torres (2012), Upwelling filaments off Cap Blanc: Interaction of the NW African upwelling current and the Cape Verde frontal zone eddy field?, *J. Geophys. Res*., *117*, C08031, doi:10.1029/2012JC007905.

Mittelstaedt, E. (1991), The ocean boundary along the northwest African coast: Circulation and oceanographic properties at the sea surface, *Prog. Oceanogr.*, *26*(4), 307-355, doi: http://dx.doi.org/10.1016/0079-6611(91)90011-A.

Mizuno, K., and W. B. White (1983), Annual and Interannual Variability in the Kuroshio Current System, *J. Phys. Oceanogr., 13,* 1847–1867. doi: http://dx.doi.org/10.1175/1520-0485(1983)013<1847:AAIVIT>2.0.CO;2

Montecino, V., T. Strub, F. Chavez, A. Thomas, J. Tarazona, and T. Baumgartner (2006), Bio-physical interactions off western South America, in *The Sea*, *14*, edited by A. R. Robinson and K. H. Brink, chap. 10, pp. 329–390, Harvard Univ. Press, Cambridge, Mass.

Moore, W. S. (1996), Large groundwater inputs to coastal waters revealed by 226Ra enrichments, *Nature*, 380.

Morgan C.A., A. De Robertis, and R.W. Zabel (2005), Columbia River plume fronts. I. Hydrography, zooplankton distribution, and community composition, *Mar Ecol Prog Ser, 299*:19–31.

Naderi, F. M., M. H. Freilich, and D. G. Long (1991), Spaceborne radar measurement of wind velocity over the ocean: An overview of the NSCAT scatterometer system, *Proc. IEEE, 79,* 850– 866.

Narimousa, S., and T. Maxworthy (1989), Application of a laboratory model to the interpretation of satellite and field observations of coastal upwelling, *Dyn. Atmos. Oceans, 13,* 1 – 46.

Nieto, K., H. Demarcq, and S. McClatchie (2012), Mesoscale frontal structures in the Canary Upwelling System: New front and filament detection algorithms applied to spatial and temporal patterns, *Remote Sens. Environ.*, *123*, 339-346, doi: http://dx.doi.org/10.1016/j.rse.2012.03.028.

Nykjær, L., and L. Van Camp (1994), Seasonal and interannual variability of coastal upwelling along northwest Africa and Portugal from 1981 to 1991, *J. Geophys. Res.*, *99*(C7), 14197–14207, doi:10.1029/94JC00814.

O'Neill, L. W., D. B. Chelton and S. K. Esbensen (2003), Observations of SST-Induced Perturbations of the Wind Stress Field over the Southern Ocean on Seasonal Timescales, *J. Climate, 16,* 2340–2354. doi: http://dx.doi.org/10.1175/2780.1.

O'Neill, L. W., D. B. Chelton and S. K. Esbensen (2012), Covariability of Surface Wind and Stress Responses to Sea Surface Temperature Fronts*, J. Climate, 25*, 5916–5942.

O'Neill, L. W., D. B. Chelton, S. K. Esbensen and F. J. Wentz (2005), High-Resolution Satellite Measurements of the Atmospheric Boundary Layer Response to SST Variations along the Agulhas Return Current, *J. Climate, 18*, 2706–2723. doi: http://dx.doi.org/10.1175/JCLI3415.1

O'Neill, L. W., D. B. Chelton, and S. K. Esbensen (2010), The effects of SST-induced surface wind speed and direction gradients on midlatitude surface vorticity and divergence, *J. Climate.*, *23*, 255–281, doi: http://dx.doi.org/10.1175/2009JCLI2613.1

Overland, J. E., and R. W. Preisendorfer (1982), A significance test for principal components applied to a cyclone climatology, *Mon. Wea. Rev.*, *110*(1), 1–4, doi: http://dx.doi.org/10.1175/1520-0493(1982)110<0001:ASTFPC>2.0.CO;2

Owen, R. W. (1981), Fronts and eddies in the sea: mechanisms, interactions and biological effects. *Analysis of marine ecosystems*, 197-233.

Pattullo, J., and W. McAlister (1962), Evidence for oceanic frontogenesis off Oregon, *Science, 135,* 106-107.

Peffley, M. B., and J. J. O'Brien (1976), A three-dimensional simulation of coastal upwelling off Oregon, *J. Phys. Oceanogr.*, *6*(2), 164–180, doi: http://dx.doi.org/10.1175/1520-0485(1976)006<0164:ATDSOC>2.0.CO;2

Peña-Izquierdo, J., J. Pelegrí, M. Pastor, P. Castellanos, M. Emelianov, M. Gasser, J. Salvador, and E. Vázquez-Domınguez (2012), The continental slope current system between Cape Verde and the Canary Islands, Sci. Mar., 76, 65–78, doi:10.3989/scimar.03607.18C.

Penven, P., C. Roy, A. Colin de Verdière, and J. Largier (2000), Simulation of a coastal jet retention process using a barotropic model, *Oceanol. Acta, 23*, 615–634.

Perlin, N., R. M. Samelson, and D. B. Chelton (2004), Scatterometer and model wind and wind stress in the Oregon–Northern California coastal zone, *Mon. Weather Rev.*, *132*(8), 2110–2129, doi: http://dx.doi.org/10.1175/1520-0493(2004)132<2110:SAMWAW>2.0.CO;2

Pietrafesa, L. J., J. O. Blanton, J. D. Wang, V. H. Kourafalou, T. N. Lee, and K. A. Bush (1985), The tidal regime in the South Atlantic Bights, in Oceanography of the Southeastern U.S. Continental Shelf, edited by L. P. Atkinson, D. W. Menzel, and K. A. Bush, pp. 63–76, AGU, Washington, D. C.

Pickett, M. H., and J. D. Paduan (2003), Ekman transport and pumping in the California Current based on the U.S. Navy's high-resolution atmospheric model (COAMPS), *J. Geophys. Res.*, *108*, 3327, doi:10.1029/2003JC001902, C10.

Polovina, J. J., D. R. Kobayashi, D. M. Parker, M. P. Seki, and G. H. Balazs (2000), Turtles on the edge: Movement of loggerhead turtles (Caretta caretta) along oceanic fronts spanning longline fishing grounds in the central North Pacific, 1997 – 1998, *Fish. Oceanogr., 9*, 1 – 13.

Polovina, J. J., E. Howell, D. R. Kobayashi, and M. P. Seki (2001), The transition zone chlorophyll front, a dynamic global feature defining migration and forage habitat for marine resources, *Prog. Oceanogr., 49,* 469 – 483.

Ralston, D. K., W. R. Geyer, and J. A. Lerczak (2010), Structure, variability, and salt flux in a strongly forced salt wedge estuary, *J. Geophys. Res., 115,* C06005, doi:10.1029/2009JC005806.

Rasmussen, B. and A. Josefson (2002), Consistent estimates for the residence times of micro-tidal estuaries, *Estuar. Coast. Shelf Sci., 54*: 65–73.

Risien, C. M., and D. B. Chelton (2008), A global climatology of wind and wind stress fields from eight years of QuikSCAT scatterometer data, *J. Phys. Oceanogr., 38,*2379–2413, doi:10.1175/2008JPO3881.1

Roden, G. I., and D. F. Paskausky (1978), Estimation of rates of frontgenesis and frontolysis in the North Pacific Ocean using satellite and surface meteorological data from January 1977, *J. Geophys. Res., 83,* 4545–4550.

Rouault, M., Lee-Thorp, A. M. and Lutjeharms, J. R. E. (2000). The atmospheric boundary layer above the Agulhas Current during alongcurrent winds. Journal of physical oceanography, 30(1), 40-50.

Rouault, M., S. Illig, C. Bartholomae, C.J.C. Reason, and A. Bentamy (2007), Propagation and origin of warm anomalies in the Angola Benguela upwelling system in 2001. *J. Mar. Syst. 68*, 473–488, doi: http://dx.doi.org/10.1016/j.jmarsys.2006.11.010.

Ryan, J. P., J. A. Yoder, J. A. Barth, and P. C. Cornillon (1999), Chlorophyll enhancement and mixing associated with meanders of the shelf break front in the Mid-Atlantic Bight. *J. Geophy. Res., 104*(C10), 23479-23493.

Ryther, J. H. (1969), Photosynthesis and fish production in the sea, *Science*, *166*(3901), 72-76, doi: 10.1126/science.166.3901.72

Samelson, R. M., E. D. Skyllingstad, D. B. Chelton, S. K. Esbensen, L. W. O'Neill, and N. Thum (2006), On the coupling of wind stress and sea surface temperature, *J. Climate, 19,* 1557-1566.

Samelson, R., P. Barbour, J. Barth, S. Bielli, T. Boyd, D. Chelton, P. Kosro, M. Levine, E. Skyllingstad, and J. Wilczak (2002), Wind stress forcing of the Oregon coastal ocean during the 1999 upwelling season, *J. Geophys. Res.*, *107*(C5), doi:10.1029/2001JC000900.

Santos, F., M. Gomez-Gesteira, M. deCastro, and I. Alvarez (2012), Differences in coastal and oceanic SST trends due to the strengthening of coastal upwelling along the Benguela current system, *Cont. Shelf Res.*, *34*, 79-86, doi: http://dx.doi.org/10.1016/j.csr.2011.12.004.

Savidge, G. (1976), A preliminary study of the distribution of chlorophyll a in the vicinity of fronts in the Celtic and western Irish Seas, *Estuarine and Coastal Marine Science, 4*(6), 617-625.

Schott, F. A., and J. P. McCreary (2001), The monsoon circulation of the Indian Ocean, *Prog. Oceanogr., 51*, 1–123.

Seo, H., A. J. Miller, and J. O. Roads (2007), The Scripps Coupled Ocean–Atmosphere Regional (SCOAR) Model, with Applications in the Eastern Pacific Sector, *J. Climate, 20*(3), 381-402.

Sheldon, J.E. and A.B. Burd (2014), Alternating effects of climate drivers on Altamaha River discharge to coastal Georgia, USA, *Estuaries and Coasts, 37*:772-788.

Sheldon, J. E., and M. Alber (2002), A comparison of residence time calculations using simple compartment models of the Altamaha River estuary, Georgia, *Estuaries and Coasts, 25,* 1304–1317. DOI: 10.1007/bf02692226.

Sheldon, J. E., and M. Alber (2005), Comparing transport times through salinity zones in the Ogeechee and Altamaha river estuaries using squeezebox, In: Hatcher KJ (ed) *Proc 2005 Georgia Water Res Conf.,* The University of Georgia, Athens

Smith, R. L. (1968), Upwelling*, Oceanogr. Mar. Biol. Annu. Rev.*, *6*, 11–46.

Smith, R. L. (1981), A Comparison of the Structure and Variability of the Flow Field in three Coastal Upwelling Regions: Oregon, Northwest Africa, and Peru, in *Coastal Upwelling*, edited by F. A. Richards, AGU, Washington, D. C.. doi: 10.1029/CO001p0107

Song, Q., P. Cornillon, and T. Hara (2006), Surface wind response to oceanic fronts, *J. Geophys. Res., 111*(C12), C12006.

Spall, M. A. (2007), Midlatitude Wind Stress–Sea Surface Temperature Coupling in the

Vicinity of Oceanic Fronts, *J. Climate*, *20*(15), 3785–3801, doi: http://dx.doi.org/10.1175/JCLI4234.1

Stramma, L., S. Hüttl, and J. Schafstall (2005), Water masses and currents in the upper tropical northeast Atlantic off northwest Africa, *J. Geophys. Res.*, *110*, C12006, doi:10.1029/2005JC002939.

Strub, P. T., and C. James (1995), The large-scale summer circulation of the California current, *Geophys. Res. Lett., 22*, 207– 210.

Strub, P. T., and C. James (2000), Altimeter-derived variability of surface velocities in the California Current System: 2. Seasonal circulation and eddy statistics, *Deep Sea Res., Part II, 47,* 831 – 870.

Strub, P. T., et al. (1991), The nature of the cold filaments in the California Current System, *J. Geophys. Res., 96,* 14,743– 14,768.

Strub, P. T., J. S. Allen, A. Huyer, R. L. Smith, and R. C. Beardsley (1987), Seasonal cycles of currents, temperatures, winds, and sea level over the northeast Pacific continental shelf: 35°N to 48°N, *J. Geophys. Res.*, *92*(C2), 1507–1526, doi:10.1029/JC092iC02p01507.

Strub, P. T., V. Combes, F. A. Shillington, and O. Pizarro (2013), Chapter 14 - Currents and Processes along the Eastern Boundaries, in *Ocean Circulation and Climate A 21st Century Perspective*, *103*, 339-384, Elsevier Science.

Sverdrup H. U., and W. E. Allen (1939), Distribution of diatoms in relation to the character of water masses and currents off southern California in 1938, *J. Mar. Res.,* *2,* 131-144.

Sverdrup, H. U., M. W. Johnson, and R. H. Fleming (1942), *The Oceans: Their physics, chemistry, and general biology*, pp. 1087, Prentice Hall, Upper Saddle River, N. J.

Sweet, W., R. Fett, J. Kerling, and P. La Violette (1981), Air-sea interaction effects in the lower troposphere across the north wall of the Gulf Stream, *Mon. Weather Rev., 109*(5), 1042-1052.

Swenson, M. S., P. P. Niller, K. H. Brink, and M. R. Abbott (1992), Drifter observations of a cold filament off Point Arena, California, in July 1988, *J. Geophys. Res., 97*(C3), 3593 – 3610.

Tebeau, P. A., and T. N. Lee (1979), Wind induced circulation on the Georgia shelf, (winter 1976/77) *RSMAS Tech Rep. 79003*, Univ. of Miami, Miami, Fla.

Thomas, A. C., P. Brickley, and R. Weatherbee (2009), Interannual variability in chlorophyll concentrations in the Humboldt and California Current Systems, *Prog. Oceanogr.*, *83*(1), 386-392, doi: http://dx.doi.org/10.1016/j.pocean.2009.07.020.

Traynum, S., and R. Styles (2008), Exchange flow between two estuaries connected by a shallow tidal channel, *J. Coastal Res., 24*(5), 1260-1268, doi:10.2112/07-0840r.1.

Uda, M. (1938), Researches on 'Some" or Current Rip in the Seas and Oceans, *Geophys. Magazine, 11*(4). pp. 307-372.

Uda, M. (1953), On the Convergence and Divergence in the NW Pacific in Relation to the Fishing Grounds and Productivity, *Bulletin of the Japanese Society of Scientific Fisheries. 19*(4). pp. 435-438.

Ullman, D. S., and P. C. Cornillon (1999), Satellite-derived sea surface temperature fronts on the continental shelf off the northeast U.S. coast, *J. Geophys. Res.*, *104*(C10), 23459–23478, doi:10.1029/1999JC900133.

Ullman, D. S., and P. C. Cornillon (2000), Evaluation of front detection methods for satellite-derived SST data using in situ observations. *J. Atmos. Ocean. Tech., 17*(12), 1667-1675.

Vazquez-Cuervo, J., B. Dewitte, T. M. Chin, E. M. Armstrong, S. Purca, and E. Alburqueque (2013), An analysis of SST gradients off the Peruvian Coast: The impact of going to higher resolution, *Remote Sens. Environ.*, *131*, 76-84, doi: http://dx.doi.org/10.1016/j.rse.2012.12.010.

Vecchi, G. A., S.-P. Xie, and A. S. Fischer (2004), Ocean-atmosphere co-variability in the western Arabian Sea, *J. Climate., 17,* 1213–1224.

Veitch, J. A., P. Florenchie, and F. A. Shillington (2006), Seasonal and interannual fluctuations of the Angola–Benguela Frontal Zone (ABFZ) using 4.5 km resolution satellite imagery from 1982 to 1999, *Int. J. Remote Sens., 27*(5), 987-998, doi:10.1080/01431160500127914.

Veitch, J., P. Penven, and F. Shillington (2009), The Benguela: A laboratory for comparative modeling studies, *Prog. Oceanogr.*, *83*(1), 296-302, doi: http://dx.doi.org/10.1016/j.pocean.2009.07.008.

Venegas, R. M., P. T. Strub, E. Beier, R. Letelier, A. C. Thomas, T. Cowles, C. James, L. Soto-Mardones, and C. Cabrera (2008), Satellite-derived variability in chlorophyll, wind stress, sea surface height, and temperature in the northern California Current system, *J. Geophys. Res., 113*, C03015, doi:10.1029/2007JC004481.

Vihma, T., J. Uotila and J. Launiainen (1998), Air‑sea interaction over a thermal marine front in the Denmark Strait, *J. Geophys. Res., 103*(C12), 27665-27678.

Walsh, J. J. (1977), A biological sketchbook for an eastern boundary current, in The Sea, vol. 6, edited by E. D. Goldbert, I. N. McCave, J. J. O'Brien, and J. H. Steele, pp. 923 – 968, Wiley-Interscience, Hoboken, N. J.

Walsh, J.J., T.E. Whitledge, J.C. Kelley, S.A. Hunstman and R.D. Pillsbury (1977), Further transition states of the Baja California upwelling ecosystem, *Limnol. Oceanogr., 22,* 264-280.

Wang, Y., R. M. Castelao, and Y. Yuan (2015), Seasonal variability of alongshore winds and sea surface temperature fronts in Eastern Boundary Current Systems, *J. Geophys. Res., 120,* 2385–2400, doi:10.1002/2014JC010379.

Warner, T. T., M. N. Lakhtakia, J. D. Doyle and R. A. Pearson (1990), Marine atmospheric boundary layer circulations forced by Gulf Stream sea surface temperature gradients, *Mon. Weather Rev., 118*(2), 309-323.

Weber, A. H., and J. O. Blanton (1980), Monthly mean wind fields for the South Atlantic Bight, *J. Phys. Oceanogr., 10* (8), 1256-1263, doi:10.1175/1520-0485(1980)010<1256:MMWFFT>2.0.CO;2.

Xie, S.-P. (2004), The shape of continents, air-sea interaction, and the rising branch of the Hadley circulation, in The Hadley Circulation: Past, Present and Future, edited by H.

F. Diaz and R. S. Bradley, pp. 121 – 152, Kluwer Acad., Dordrecht, Netherlands

Yang, G., F. Wang, Y. Li, and P. Lin (2013), Mesoscale eddies in the northwestern subtropical Pacific Ocean: Statistical characteristics and three-dimensional structures, *J. Geophys. Res., 118,* 1906–1925, doi:10.1002/jgrc.20164.

Yoder, J. A., S. E. Schollaert, and J. E. O'Reilly (2002), Climatological phytoplankton chlorophyll and sea surface temperature patterns in continental shelf and slope waters off the northeast US coast. *Limnol. Oceanogr., 47*(3), 672-682.

Zhao, L., C. Chen, J. Vallino, C. Hopkinson, R. C. Beardsley, H. Lin, and J. Lerczak (2010), Wetland-estuarine-shelf interactions in the Plum Island Sound and Merrimack River in the Massachusetts coast, *J. Geophys. Res., 115*, C10039, doi:10.1029/2009JC006085.

APPENDIX A

WIND-DRIVEN VARIABILITY IN SEA SURFACE TEMPERATURE FRONT DISTRIBUTION IN THE CALIFORNIA CURRENT SYSTEM

Castelao, R. M and Y. Wang. 2014. *J. Geophys. Res., 119*(3), 1861-1875
Reprinted here with permission of the publiser

7.1 Abstract

Simultaneous satellite-derived observations from 2002-2009 are used to quantify the relation between sea surface temperature (SST) fronts and ocean winds in the California Current System (CCS). An edge-detection algorithm is applied to SST observations to generate monthly maps of frontal probabilities. Empirical orthogonal decompositions reveal that the seasonal evolution of fronts in the CCS is strongly related to the seasonal evolution of coastal alongshore wind stress. The seasonal development of SST fronts is remarkably different to the north and to the south of Cape Mendocino, however. While fronts to the north of the cape extend for hundreds of kilometers from the coast peaking during summer and fall, when upwelling winds are stronger off northern California and Oregon, the region to the south of Cape Mendocino is characterized by high frontal activity during spring in a much narrower band close to the coast. Throughout the region, anomalies in the intensity of upwelling favorable wind stress are followed by anomalies in frontal activity. The width and speed of the widening of the region of high frontal activity are also related to coastal alongshore wind stress. Interannual variability in the timing of the widening of the region of high frontal activity in the lee of Cape Blanco compared to the timing of the spring transition to upwelling favorable winds may be related to the wind stress curl distribution in the lee of the cape. Stronger upwelling favorable wind stress curl anomalies lead to early widening of the region of high frontal activity.

7.2 Introduction

Continental shelves located at the eastern boundaries of the oceans are often characterized by the occurrence of upwelling, especially at locations where the predominant winds are equatorward. Prevailing equatorward winds at eastern boundaries of the oceans result in net offshore transport in the surface Ekman layer, and upwelling of cold, saline water near the coast. The rising water brings nutrients to the euphotic zone (Sverdrup et al., 1942), which influences the distribution of phytoplankton (Sverdrup and Allen, 1939) and help sustain a highly productive food web (Walsh, 1977). A sea surface temperature (SST) front is often established separating the cold, upwelled water near the coast from warm, offshore waters (e.g., Kostianoy and Lutjeharms, 1999), and a strong alongshore coastal upwelling jet is formed in geostrophic balance with the upwelled isopycnals (Huyer, 1983). Thus, the locations of the SST fronts are generally good proxies for the location of flow intensifications in upwelling regions within Eastern Boundary Currents (Strub and James, 2000). Additionally, most fronts are characterized by convergent flow at the surface (Bowman, 1978). Free floating biota are drawn into frontal zones due to the prevailing convergent flow, a process that in time can lead to a fully developed food chain as fish at higher trophic levels are likewise attracted to these regions in search of food.

SST fronts in Eastern Boundary Currents have received a great deal of attention over the last few years (e.g., Meunier et al., 2012; Nieto et al., 2012; Santos et al., 2012; Vazquez-Cuervo et al., 2013). Field data indicate that jets often flow along sharp gradients in SST in those areas (Kelly, 1983; Swenson et al., 1992; Huyer et al., 1998; Strub and James, 2000). Fronts and frontogenesis (Pattullo and McAlister, 1962) have been shown to play an important role on regional dynamics in Eastern Boundary Currents, being associated with the development of submesoscale features, strong vertical velocities, and high Rossby numbers (e.g., Capet et al., 2008a,b,c). SST fronts have also been shown to have a profound influence on wind stress variability, leading to large anomalies in wind stress curl and wind stress divergence (O'Neill et al., 2003; Chelton et al, 2004; 2007; O'Neil et al., 2005; 2010; Chelton and Xie, 2010; Castelao, 2012; among others).

In the California Current System (CCS) off the West Coast of North America, many previous studies have revealed complex circulation patterns (Hickey, 1979; 1998; Huyer, 1983), with intense jets and fronts (e.g., Kosro and Huyer, 1986; Chelton et al., 1987; Kosro et al., 1991; Strub et al., 1991; Huyer et al., 1998; Barth et al., 2005) embedded in a rich eddy field (Strub and James, 1995; Kelly et al., 1998; Brink et al., 2000). Recent analysis reveals increasing trends in the frequency of occurrence of SST fronts in the CCS at decadal scales (Kahru et al., 2012). Using 4 years of geostationary satellite observations, Castelao et al. (2006) described the seasonal evolution of SST fronts in the region. The relatively short time series used didn't allow them to identify the processes driving the seasonal evolution of SST fronts in the CCS. Identifying those processes is important, however, since it has been hypothesized that the ultimate source of energy in the jets in the CCS is the formation of the density (or temperature) front near the coast (Strub and James, 2000). Strub and James (2000) further suggested that dynamical instabilities of the jet are the immediate source of eddy kinetic energy around the core of the seasonal jet. Therefore, the formation and evolution of fronts seem to be intrinsically related to the development of seasonal circulation, to the evolution of eddy kinetic energy, and to ecosystem processes in the CCS and likely in the other Eastern Boundary Currents. Here, we focus on quantifying the role played by surface wind stress on the observed spatial and temporal variability in sea surface temperature fronts in the CCS.

7.3 Methods

Infrared sea surface temperature (SST) measurements from 2002 to 2009 were obtained from the Moderate Resolution Imaging Spectroradiometer (MODIS) onboard the polar orbiting satellite Aqua. Maps of ocean SST fronts were produced using an edge-detection algorithm (Canny, 1986), as in Castelao et al. (2005; 2006). Briefly, we first compute the SST gradient vector. The algorithm then tracks in the direction of the gradient, suppressing any pixel that is not a local maximum (nonmaximum suppression). The thresholding in the edge-detection algorithm is done with hysteresis. The algorithm first looks for pixels with gradient magnitude larger than a threshold T1. These pixels are flagged as frontal pixels. Then, the algorithm tracks along a front crest (i.e., perpendicular to the SST gradient), flagging individual pixels as fronts until the gradient magnitude falls below a smaller threshold T2. This helps to ensure that noisy edges are not broken up into multiple edge fragments. Thresholds employed are 0.028 and 0.014°C km-1. It is important to emphasize that gradient magnitudes in the CCS can vary between satellite sensors because of instrument and algorithm differences (Armstrong et al., 2012), so different thresholds may need to be applied depending on the SST product used. Comparisons of fronts detected with gradient magnitude maps show that the chosen threshold values allow for capturing most of the main fronts in the CCS. To account for spatial and temporal variability in cloud cover, for each frontal image we take the number of times a particular pixel qualifies as a front and divide this value by the number of times that the pixel was clear during that time period, yielding a frontal probability (e.g., Ullman and Cornillon, 1999; Mavor and Bisagni, 2001). Here, frontal probabilities were produced at monthly intervals.

Previous studies have shown that the mean position of the upwelling front in the CCS moves offshore during spring and summer (e.g., Breaker and Mooers, 1986), leading to a progressive widening of the coastal region characterized by high frontal activity (Castelao et al., 2006). In order to obtain estimates of the speed of the widening of the region of high frontal activity, we compare the width of the region of high frontal probabilities close to the coast between consecutive months. Individual frontal probability maps are generally noisy, however. Therefore, we first apply a running mean to obtain a smooth representation of the frontal probabilities for each 1-degree-wide latitudinal band. The width of the region with high frontal activity for each 1-degree-wide latitudinal band is defined as the distance from the coast to the location where the smoothed probabilities decreases to 37% of the maximum value at that particular latitude. Visual inspections reveal that the method works well to identify the offshore boundary of the region of high frontal activity. By differencing the width of the region with high frontal activity between consecutive months, the speed of the widening of the high frontal activity region during that period can be quantified. Note that this is a different metric than the speed of offshore migration of individual fronts.

Surface wind speed and direction from 2002 to 2009 were obtained from the SeaWinds scatterometer onboard NASA's Quick Scatterometer (QuikSCAT) satellite. A detailed description of QuikSCAT is given by Chelton and Freilich (2005). The SeaWinds scatterometer is a scanning microwave radar that infers the surface wind stress from measurements of radar backscatter from the roughness of the sea surface at multiple antenna look angles (Naderi et al., 1991). Surface stresses are obtained from the equivalent neutral stability 10-m winds using the modified Large-Pond drag coefficient for neutrally stable conditions (Large et al., 1994). In the standard processing of QuikSCAT data used here, the spatial resolution is about 25 km and measurements closer than about 30 km to land are contaminated by radar backscatter from land in the antenna side lobes. The wind stress curl was computed within each measurement swath using centered differences. The alongshore component of the wind stress was determined as the dot product between wind measurements within 150 km from the coast and a unit vector tangent to the local coastline (obtained by fitting a straight line through a 100 km section of a coastline centered at the coastal point). Cumulative alongshore wind stress time series for each year are used to determine the timing of the spring transition (Huyer et al., 1979) for each latitudinal band following Barth et al. (2007).

Comparisons between wind stress variables and SST or SST frontal probabilities are restricted to the period from 2002 to 2009, when SST observations from MODIS and wind measurements from QuikSCAT are available simultaneously. For empirical orthogonal function (EOF) analyses, monthly averages of the alongshore component of the wind stress averaged within 150 km from the coast were first computed to facilitate comparisons with the monthly frontal probability data. The temporal mean at each location was determined and then removed from the corresponding time series before the decompositions were computed.

Temperature and salinity profiles from the National Oceanographic Data Center (NODC) were used to compute buoyancy frequency profiles in the CCS. Observations are available since the 1910's, although the majority of the data are from 1950 to 2010. The observations were processed as in Lentz (2003) and Castelao (2011) to eliminate unreliable measurements. Once processed, they were used to compute the internal Rossby radius of deformation as a function of latitude in the CCS by solving the vertical mode problem (Kundu et al., 1975). Only observations collected from May to September were used in the computation of the internal Rossby radius of deformation, since that is the period of strong frontal activity in the region (Castelao et al., 2006).

7.4 Results

7.4.1 Variability in frontal activity and wind forcing in the CCS

The long term average distribution of frontal probabilities and SST gradient magnitudes in the CCS, together with the dominant modes of variability extracted by decomposing the frontal probabilities and SST gradient magnitudes into empirical orthogonal functions (EOFs), are shown in Figure A.1. Consistent with previous studies, averaged frontal probabilities and SST gradient magnitudes are high close to the coast, decreasing offshore. For both variables, the first two EOFs are related to the seasonal evolution of fronts (Figure A.2). The first EOF of frontal probabilities captures the seasonal enhancement of frontal activity between the Oregon coast, just south of the Columbia River mouth, and Cape Mendocino, although relatively large (although somewhat smaller) values for EOF 1 extend farther south to the region off Point Reyes (Figure A.1). In this northern section of the CCS, the seasonal enhancement of fronts occurs from late spring to fall (i.e., from June to October), peaking in September (Figure A.2). During that period, high frontal activity in the northern CCS extends for several hundreds of kilometers from the coast. A similar picture is captured by the first EOF of SST gradient magnitude, although the enhancements upstream of Heceta Bank off Oregon and around Cape Blanco are more pronounced. The second EOF of frontal probabilities is also related to the seasonal evolution of fronts in the CCS. In that case, however, high values are observed near the coast to the south of Cape Mendocino all the way to Point Conception (Figure A.1). In that area, the seasonal increase in frontal probabilities occurs earlier than farther north during the spring, peaking in June (Figure A.2). The same is true for the second EOF of SST gradient magnitude, which reveals that gradients increase near the coast to the south of Cape Mendocino (but also in the lee of Cape Blanco) during spring. Note, however, that the seasonal increase in frontal activity and SST gradient magnitude near the coast to the south of Cape Mendocino during spring (captured by EOF 2) is considerably smaller than the seasonal increase observed farther north (captured by EOF 1). The largest seasonal variability for both variables occurs off the Oregon and northern California coastlines. Off Cape Blanco, the negative values of EOF 2 far from the coast (Figure A.1; ~126°W, 42-44°N) reveals that SST gradient magnitudes offshore increase during fall, when the amplitude time series for EOF 2 is negative (Figure A.2). In both cases, the EOFs explain a relatively small percentage of the total variance (12.8% and 3.8% for frontal probabilities, 36% and 6.4% for SST gradient magnitudes). In the regions where the EOFs are high (yellow to red colors in Figure A.1), however, they explain 15-30% (EOF 1) and ~10% (EOF 2) of the local fraction of the variance of frontal probabilities (computed as in Chelton and Davis, 1982). For SST gradient magnitude, EOFs 1 and 2 explain 40-70% and ~20% of the local fraction of the variance, respectively. In the offshore regions where the absolute values of the EOFs are small, EOFs 1 and 2 explain a negligible fraction of the local variance. As a result, the EOFs, although capturing a significant fraction of the variance in the areas within a few hundred kilometers from the coast, explain a relatively small fraction of the total variance.

Analysis of the EOFs amplitude time series for the different years, instead of the monthly average time series, reveals substantial interannual variability in the seasonal evolution of the fronts (Figure A.3). Off Oregon and northern California (i.e., in areas where EOF 1 is large), for example, frontal activity in late summer and fall was enhanced in 2002, consistent with previous results obtained using a much shorter time series (Castelao et al., 2006). Interannual variability seems to be more pronounced to the south of Cape Mendocino near the coast (i.e., where EOF 2 is large), however, where frontal activity (both probabilities and SST gradient magnitudes) were substantially weaker in fall 2002 and fall 2006 than in other years. At least some of the observed variability may be related to the moderate El Niño event that took place along the U.S. west coast during 2005 and 2006.

An EOF decomposition of the alongshore component of the coastal wind stress was also pursued to extract variability as a function of latitude in the CCS (Figure A.4). Average wind stress to the north of Cape Blanco is weak, approaching zero off Heceta Bank. To the south of Cape Blanco, alongshore wind stress is on average negative (upwelling favorable), increasing in intensity toward the south. Strongest averaged alongshore wind stress is observed between Cape Mendocino and Point Arena. It is important to point out, however, that observations within about 30 km from the coast are discarded in the QuikSCAT observations to avoid land contamination, so the average alongshore wind stress may not be representative of winds within that band. In contrast to the average fields, the absolute value of the first EOF of the alongshore wind stress (78%

of total variance) is largest to the north of Cape Mendocino, peaking off Cape Blanco. To the south of Point Arena, the magnitudes of EOF 1 values are substantially reduced. The amplitude time series (Figure A.2) reveals that the EOF is related to the seasonal evolution of upwelling wind stress in the northern part of the CCS. Values are positive from May to October, and the peak in the intensification of upwelling favorable wind stress off Oregon and northern California occurs from June to September. During that period, upwelling favorable wind stress (i.e., average plus EOF 1) between Cape Blanco and Cape Mendocino is about as strong as to the south of Point Arena. The second EOF (17% of total variance), on the other hand, is characterized by a zero crossing off Cape Mendocino (Figure A.4). The amplitude time series is positive from March to June, indicating that upwelling favorable wind stress to the south of Cape Mendocino is intensified during that period (Figure A.2).

As was the case for the frontal probability EOFs, the amplitude time series of the alongshore wind stress EOFs reveals multiple events of large interannual variability (Figure A.3). The winter of 2005-2006 was characterized by anomalously strong downwelling favorable wind stress off Oregon and northern California, for example. The duration of the upwelling season, as defined by the timing of upwelling favorable wind stress, also varies largely from year to year. In 2002, for example, the amplitude time series for EOF 1 was positive for 8 months. In 2005, on the other hand, positive values were only observed during 4 months, indicating a much shorter upwelling season. The onset of upwelling favorable wind stress is also delayed compared to other years (see also

Barth et al., 2007). Large variations in the duration of the intensification of upwelling favorable wind stress to the south of Cape Mendocino can also be observed (compare amplitude time series for EOF 2 during spring 2007 and spring 2009, for example).

The spatial averages of the frontal probability EOFs (from Figure A.1) within 400 km from the coast are also shown in Figure A.4 as a function of latitude, revealing a remarkable agreement with the EOFs of the alongshore wind stress. As was the case for the wind stress data, the cross-shelf average of the first EOF of frontal probabilities is enhanced off Cape Blanco – Cape Mendocino, decreasing to the south of that (although the decrease is not as strong as it was for the first EOF of wind stress observations). The cross-shelf average of the second EOF of frontal probabilities also presents a zero crossing around Cape Mendocino, again agreeing with the second EOF of the alongshore wind stress observations. Amplitude time series of the EOFs of alongshore wind stress and frontal observations are also in agreement (Figure A.3), with the peak in the amplitude time series for EOF 1 of the wind stress observations occurring about one month earlier than the peak in frontal occurrence and SST gradient magnitudes in the northern sector of the CCS. The amplitude time series for the second EOF of alongshore wind stress observations and frontal probabilities also agree well. As it is evident by visual inspection (Figure A.3), however, the amplitude time series are dominated by the seasonal cycle, which substantially decreases the effective number of degrees of freedom. In order to improve statistical reliability, we follow Chelton (1982) and pre-whiten the time series by removing the monthly averages (shown in Figure A.2) from the alongshore wind stress and frontal probability amplitude time series. Those anomalies in the amplitude time series are then compared to each other to investigate if a dynamical connection between alongshore wind stress and frontal activity exists in the CCS. As discussed in Chelton (1982), this does not remove any true physical relationship between the two time series, since the seasonal variation of a quantity is never a pure-tone harmonic. If the seasonal alongshore wind stress is stronger than average or peaks earlier than usual during a certain year, for example, then frontal activity should also be stronger than average or peak earlier than usual if a connection between the two variables exist. We note that, at locations where an EOF of the alongshore wind stress is negative (Figure A.4), a positive anomaly in the amplitude time series can represent either anomalously strong upwelling favorable wind stress or anomalously weak downwelling favorable wind stress. Comparisons between the time series of the amplitude anomalies for EOF 1 (with wind stress observations leading frontal probability observations by 1 month) reveal that anomalously weak upwelling or strong downwelling wind stress is generally associated with anomalously low frontal activity, while anomalously strong upwelling or weak downwelling wind stress is generally accompanied by anomalously high frontal activity in the following month (Figure A.5). Comparison between the anomalies of the amplitude time series for the second EOFs of alongshore wind stress and frontal probabilities are also correlated, such that anomalously weak upwelling wind stress south of Cape Mendocino is generally accompanied by anomalously low frontal activity in that area.

7.4.2 Widening of the region of high SST frontal activity in the CCS

Previous studies have shown that the area near the coast characterized by high frontal activity widens from spring to fall (e.g., Castelao et al., 2006). The average speed of the widening of the region with high frontal activity as a function of latitude from June to September is shown in Figure A.6. Relative large speeds are observed from just north of Cape Blanco to Point Reyes, peaking around Cape Mendocino. To the north of Cape Blanco or to the south of Point Reyes, speeds are small, which is consistent with the seasonal evolution of SST fronts in those regions (see Figure A.1, for example).

It has been suggested that the mean position of the upwelling front in the CCS moves offshore in response to Ekman transport and/or Rossby wave dynamics (e.g., Breaker and Mooers, 1986). The average speed (directed offshore) associated with the surface Ekman transport due to alongshore wind stress during the same period is also shown in Figure A.6. Since the thickness of the surface layer in which the Ekman transport is distributed in unknown, we consider two values (20 m and 30 m) to obtain a measure of uncertainty in the estimate. Consistently with the widening of the region of high frontal activity, the seasonally-averaged speed due to surface Ekman transport is maximum around Cape Mendocino, decreasing to the north of Cape Blanco and to the south of Point Reyes/Point Arena. The speeds driven by the alongshore wind stress are 2 to 3 times larger than the speed of offshore movement of the boundary of the region of high frontal activity, depending on the thickness used for the surface Ekman layer. Two estimates of the westward phase speed of long baroclinic Rossby waves are also shown in

Figure A.6. For one of the estimates, all temperature and salinity observations from the NODC archives that were collected around the 2000 m isobath between May and September are used to estimate the first baroclinic Rossby radius by solving the vertical mode problem (Kundu et al., 1975), which is then used to compute the phase speed of long baroclinic Rossby waves. We note that, although the latitudinal dependence of the phase speeds is quite small for the region of interest, the dependence does present the characteristic exponential increase with decreasing latitude to the south of 32°N (not shown). A second estimate is obtained from Chelton et al. (2011). Regardless of the estimate used, the latitudinal dependence of the phase speed of long baroclinic Rossby waves is different than the latitudinal variation of the seasonally-averaged speed of the widening of the region of high frontal activity. Rossby wave speeds are also somewhat lower, especially between Point Arena and Cape Blanco.

Additional support for the potential role of alongshelf wind stress on the widening of the region of high frontal activity is obtained by comparing the average wind stress during the upwelling season (May to September) between Cape Blanco and Cape Mendocino for the different years with the maximum width of the region of high frontal activity at the end of the upwelling season (September; Figure A.7). In years when the seasonally-averaged upwelling favorable wind stress is stronger, the region of high frontal activity in the CCS extends farther from the coast compared to years characterized by relatively weak upwelling-favorable wind stress. Qualitatively similar results are obtained if the average wind stress is computed from June to September.

In addition to the latitudinal variations shown in Figure A.6, the speed of the widening of the region of high frontal activity also varies temporally (Figure A.8). To the south of Cape Mendocino, the widening of the region of high frontal activity occurs relatively early in the year, with maximum speeds occurring in July. The speed of the widening of the region of high frontal activity decreases rapidly after that, being approximately zero in September and October. To the north of Cape Mendocino, in contrast, the widening of the region of high frontal activity occurs later in the year. Fast widening of the region of high frontal activity is observed from July to September, before the widening abruptly slows down by October.

The time series of the speed of the widening of the region of high frontal activity (Si; see Figure A.8 for an example) for different 1 degree latitudinal bands during the upwelling season can be used as weights to obtain the average time of the widening of the region of high frontal activity (T*)

$$T^* = \frac{\sum SiTi}{\sum Si} \tag{1}$$

where Ti is time in months (J=1, F=2, M=3, and so on). This is analogous to previous estimations of the weighted-average position or depth of the fronts using frontal probabilities or SST gradient magnitudes as weights (Mavor and Bisagni, 2001; Castelao et al., 2005). T* is smaller when fast widening occurs earlier in the year (e.g., in Figure A.8, T* is July 3rd for the southern region, and August 1st for the northern region). As such, it provides a straightforward way to identify differences in the timing of the widening of the region of high frontal activity. Only observations from 2003 to 2009 are used in the analyses, since SST data from MODIS are only available from July 2002 on, after the onset of the upwelling season in 2002. Consistent with Figure A.8, the average time of the widening of the region of high frontal activity occurs much earlier in the south of the domain, occurring progressively later toward the northern California and Oregon coasts (Figure A.9). The average time of the offshore movement of the boundary of the region of high frontal activity occurs about 100 days later off northern Oregon compared to the region off Point Conception. The timing of the spring transition, defined as in Barth et al. (2007) using cumulative alongshore wind stress time series for each year, presents a somewhat similar latitudinal dependence. The spring transition occurs approximately two and a half months earlier off Point Conception than off northern Oregon. Over the entire latitudinal range, the average time of the widening of the region of high frontal activity occurs 97±13 days after the spring transition.

The timing of the widening of the region of high frontal activity in relation to the spring transition in the lee of Cape Blanco (where the upwelling jet typically separates from the coast; Barth et al., 2000) varies between the years, however. The year-to-year variability may be related to the time integral of the wind stress curl anomaly between 40°-43°N within 150 km from the coast,

$$Z = \int \hat{k} \cdot \left(\nabla \times \frac{\vec{\tau}_s}{\rho f} \right) dt \qquad (2)$$

where $\hat{k}$ is a unit vector in the local vertical direction, $\vec{\tau}_s$ is the wind stress vector, ρ is the water density, f is the Coriolis parameter, and t is time. The wind stress curl anomaly is defined as the difference between the instantaneous wind stress curl and the long-term summer average. For each year, we first determine the average time of the widening of the region of high frontal activity (T*) between 40º-43ºN. The time integral in Eq. (2) spans the 3 months prior to T*. Once again, only observations from 2003 to 2009 are used in the analyses, since SST observations are not available for the entire upwelling season in 2002. Upwelling favorable wind stress curl anomalies (i.e., positive Z) are generally associated with early widening of the region of high frontal activity, while negative anomalies are generally accompanied by a delay in the offshore movement of the boundary of the region of high frontal activity (Figure A.10).

7.5 Discussion

Multi-year satellite observations of sea surface temperature (SST) are used to investigate the seasonal evolution of SST fronts in the California Current System and their relation to wind forcing. SST fronts and SST gradients are distinctly different to the north and to the south of Cape Mendocino. Off northern California and Oregon, high frontal activity extends for several hundred kilometers from the coast, peaking in early fall. Increased frontal activity between Cape Mendocino and Point Conception is generally observed in a region closer to the coast, peaking in late spring (Figures A.1 and A.2). The latitudinal variations in the spatial EOFs of SST frontal probabilities and alongshore wind stress obtained from independent observations are remarkably similar (Figure A.4). For both variables, the first EOF is larger off Cape Blanco, indicating that the strongest increase in frontal activity occurs at the same location where the strongest increase in the magnitude of southward wind stress during the upwelling season occurs. Moreover, comparing the amplitude time series of the first EOFs, after the respective monthly averages are removed, indicates that anomalies in the intensity of upwelling favorable wind stress are accompanied by anomalies in frontal activity (Figure A.5). The same is true for comparisons based on the second EOFs of SST frontal probability and wind forcing, which indicates that anomalies in the strength of upwelling wind stress to the south of Cape Mendocino are accompanied by anomalies in the frequency of occurrence of SST fronts. Since the anomaly time series contain information at seasonal time scales (Chelton, 1982), these results suggest that the seasonal evolution of SST fronts is directly related to the seasonal development of coastal upwelling favorable wind stress in the CCS. Using SST front distributions from AVHRR observations from an area to the south of Cape Mendocino and monthly Coastal Upwelling Index values from the NOAA Pacific Fisheries Environmental Laboratory at 30°N, Kahru et al. (2012) showed that frontal activity and wind variability at 30°N are correlated at monthly time scales. The present results are consistent with their observations (i.e., EOF 2 of wind stress and fronts are correlated, Figures A.4 and A.5), but reveal that the evolution of frontal activity to the north of Cape Mendocino is different than in the area studied by Kahru et al. (2012), and that alongshore variability in upwelling intensity in the CCS, in particular the differences in the seasonal evolution of wind stress to the north and to the south of Cape Mendocino, play a large role in explaining the phase difference in frontal activity in the CCS revealed by the EOF analysis (Figures A.1 and A.2). Recent analyses suggest that the seasonality of frontal activity is also in phase with upwelling winds in the Canary Upwelling System (Nieto et al., 2012).

The analyses also reveal that, consistent with previous studies, there is a general tendency for the region of high frontal activity near the coast to widen from spring to fall. There is large alongshore variability in the speed in which the area of high frontal activity widens, however. The speed is maximum off Cape Mendocino, decreasing progressively to the north and to the south of the cape (Figure A.6). The alongshore variation in how fast the widening occurs is similar to the alongshore variation in the intensity of the alongshore wind stress, again suggesting a relation between coastal alongshore winds and frontal activity. Indeed, average wind stress between Cape Blanco and Cape Mendocino during the upwelling season seems to be a good predictor of the width of the area of high frontal activity at the same region at the end of the upwelling season (Figure A.7). It is not clear based on the analysis, however, how the winds influence the widening of the region of high frontal activity. It is possible, for example, that increased winds lead to strong offshore Ekman transport (Figure A.6), which has been shown to be associated with the offshore movement of the mean position of upwelling fronts over periods of days-to-weeks (Breaker and Mooers, 1986; Castelao and Barth, 2005). It is also possible, however, that stronger wind stress leads to a stronger upwelling jet characterized by high

Rossby numbers, which favors jet separation at topography perturbations (Castelao and Barth, 2006). The upwelling jet off Oregon has been shown to often separate at Cape Blanco (Barth and Smith, 1998; Barth et al., 2000) or farther north at Heceta Bank (Castelao et al., 2005), which can lead to offshore deflection and movement of fronts for hundreds of kilometers (Figure A.11). Therefore, stronger wind stress could lead to a wider region of frontal activity near the coast because it would increase the offshore deflection of the upwelling jet at Cape Blanco due to its increased inertia. We note that the offshore migration of individual fronts (as in Figure A.11) can occur much faster than the widening of the region of high frontal activity. A third possible explanation is that stronger wind stress and the resulting stronger upwelling jet interacting with coastal promontories in the CCS could lead to increased eddy activity and filament formation. Using 15 years of satellite altimetry measurements, Chaigneau et al. (2009) showed that long-lived cyclonic and anticyclonic eddies to the north of 35°N in eastern boundary upwelling systems propagate westward at speeds that agree with the theoretical value for long baroclinic Rossby waves. At these relatively high latitudes, Rossby wave speed estimates based on historical data, which agrees with the estimates presented by Breaker and Mooers (1986) and Chaigneau et al. (2009), are smaller than the speed of the widening of the region of high frontal activity, especially between Point Arena and Cape Blanco (Figure A.6). As recently shown by Meunier et al. (2012), however, the interaction of eddies (including topographic eddies) can lead to rapid offshore advection of upwelled water, resulting in increased frequency of front occurrence away from the coast (Kahru et al., 2012). This can lead to a relatively faster widening of the region of high frontal activity compared to the western propagation speed of individual eddies, since rotational speed of eddies in the CCS are generally substantially higher than their translation speeds (see Figure 17 in Chelton et al., 2011). Indeed, many previous studies have shown that sea surface height anomalies and eddy kinetic energy around Cape Mendocino migrate offshore (e.g., Kelly et al., 1998; Strub and James, 2000) at speeds that are consistent with the widening of the band of high frontal activity near the coast shown in Figure A.6. In other eastern boundary currents, SST gradients also seem to migrate offshore at times of high eddy kinetic energy (Vazquez-Cuervo et al., 2013). In this scenario, therefore, stronger wind stress would lead to a stronger upwelling jet and increased eddy generation and filament formation (e.g., due to flow topography interactions, dynamical instabilities of the jet; Haidvogel et al., 1991; Bateen, 1997). This could then lead to increased advection of cold, recently upwelled water offshore, resulting in a wider region of high frontal activity. Fast widening off Cape Mendocino in that case would be consistent with higher eddy kinetic energy observed in that region (Strub and James, 2000).

Regardless of which mechanism described above is more important, it seems clear that alongshore wind stress plays a dominant role controlling the widening of the region of high frontal activity near the coast. Larger speeds are observed earlier in the year to the south of Cape Mendocino, but later in the year to the north of the Cape (Figure A.8). This seems to be related to the timing of the spring transition to upwelling-favorable wind stress (Figure A.9), which is known to present a large latitudinal variation in the CCS (Strub et al., 1987). The average time of the widening of the region of high frontal activity, as defined in (1), occurs about 3 months into the upwelling season. Another factor that can influence the width of the region of high frontal activity is topographic features, which can either arrest the offshore movement of fronts (e.g., northern sector of Heceta Bank off Oregon; Castelao et al., 2005) leading to a narrow region of high frontal activity even if wind forcing is strong, or deflect fronts offshore leading to a broader region of high frontal activity around topography perturbations even if wind forcing is spatially uniform.

We also compared the spatial and temporal distribution of frontal probabilities to wind stress curl observations from QuikSCAT, but found no clear relationship. This is surprising, since convergences associated with the negative wind stress curl characteristic of the CCS away from the coast (Bakun and Nelson, 1991) implies favorable conditions for formation of fronts and convergent patches of recently upwelled water (Bakun and Nelson, 1977). It is possible, however, that any variability associated with the relatively weak negative wind stress curl away from the coast is small compared to variability introduced by other forcing (e.g., instabilities of the upwelling jet), overshadowing any possible effect. It is also possible that wind stress curl and SST front variability are related to each other over short time scales, and that the relationship is not captured here because of the use of monthly averaged observations. We note that the correlation time scale for SST off the central California coast has recently been estimated at 6.5 days (Breaker et al., 2010).

In the lee of Cape Blanco, however, positive wind stress curl is strongly intensified during the upwelling season (e.g., Perlin et al., 2004). Upwelling is intensified in the region (e.g., Huyer et al., 2005), partially because of variations in vorticity resulting from curvature of the trajectory as the flow passes the cape (Arthur, 1965). The widening of the region of high frontal activity in the lee of Cape Blanco, where the upwelling jet typically separates from the coast in the CCS (Barth et al., 2000), may be linked to variations in the wind stress curl intensification in the lee of the cape (Figure A.10). If we assume that the widening of the region of high frontal activity in the lee of Cape Blanco is related to jet separation at the cape (Figure A.11; see also Barth et al., 2000), this is consistent with idealized numerical simulations by Castelao and Barth (2007). They showed that positive wind stress curl anomalies in the lee of a cape similar to Cape Blanco create a cross-shelf pressure gradient that sustains an intensification of the southward velocities offshore via the thermal wind balance. This aids jet separation via continuity and by creating potential vorticity contours that track far offshore of the cape. In their idealized simulations, the timing of jet separation was dependent on the intensity of the wind stress curl (averaged over a period of 2.5-3 months) in the lee of the cape, such that stronger positive curl leads to earlier separation. This is consistent with the widening of the region of high frontal activity south of Cape Blanco occurring a few days earlier (with respect to the timing of the spring transition) in years when the positive wind stress curl intensification is anomalously strong compared to years when the intensification is anomalously weak (Figure A.10). It would be interesting to compare variability in the intensity of the wind stress curl and the timing of the widening of the region of high frontal activity in the lee of capes in other Eastern Boundary Currents where the upwelling jet first separates from the coast (e.g., Punta Lavapie off Chile, Mesias et al., 2001, 2003; Cape Columbine in the Benguela Upwelling System, Penven et al. 2000). Those variables being related in other Eastern Boundary Currents would be consistent with Castelao and Barth (2007) results.

The relationships observed here between the timing of the widening of the region of high frontal activity and wind stress curl anomalies in the lee of capes (Figure A.10), or between averaged upwelling-favorable wind stress and the width of the band of high frontal activity (Figure A.7) are based on only a few years of observations. As longer time series of observations are gathered (e.g., from the Advanced Scatterometer – ASCAT – on board the Meteorological Operational MetOp-A satellite), it will be interesting to investigate if the relationships observed here (e.g., Figures A.7 and A.10) remain true. Longer high-resolution wind stress and wind stress curl time series are also needed to investigate low frequency variability in the coupling between winds and fronts in the CCS. Trends in SST gradients in the Benguela Current System have been linked to strengthening of upwelling favorable winds in the region (Santos et al., 2012). This will be particularly interesting in the CCS, since a statistically significant increasing temporal trend in frontal probabilities over the last 30 years has been recently reported (Kahru et al., 2012).

Lastly, we note that fronts can form, evolve, migrate and dissipate on time scales shorter than one month. That variability, therefore, cannot be fully represented with the frontal probabilities produced here at monthly intervals. Analysis of frontal activity over shorter periods can provide new insights on frontal variability in the CCS. The tradeoff is that fewer cloud-free images will be available for analyses.

7.6 Summary

Satellite observations were used to quantify the relation between wind forcing and SST frontal activity in the California Current System. The seasonal evolution of SST fronts is remarkably different to the north and to the south of Cape Mendocino. To the south of the Cape, where upwelling favorable wind stress peaks in spring, frontal activity is largest in June in a band close to the coast that extends all the way to Point Conception. To the north of Cape Mendocino, where the spring transition to upwelling-favorable winds occur later in the year, the area of high frontal activity is much broader, peaking in September. Over the entire area, anomalously strong (weak) upwelling wind stress is followed by anomalously strong (weak) frontal activity, suggesting that the seasonal cycle of frontal activity is strongly influenced by the seasonal cycle of coastal alongshore wind stress. The width and speed of the widening of the region of high frontal activity are also related to coastal alongshore wind stress. The timing of the widening of the region of high frontal activity in the lee of Cape Blanco, on the other hand, may be related to the strength of the positive wind stress curl intensification in the lee of the cape.

7.7 Acknowledgments

We thank three anonymous reviewers for their thorough and constructive reviews of this paper. The authors gratefully acknowledge support by NASA through grant NNX10AE92G. All observations used here are available at http://podaac.jpl.nasa.gov and www.nodc.noaa.gov.

References

Armstrong, E., G. Wagner, J. Vazquez-Cuervo, and T. Chin (2012), Comparisons of regional satellite sea surface temperature gradients derived from MODIS and AVHRR sensors, Intern. *J. Rem. Sensing, 33*, 6639-6651.

Arthur, R. S. (1965), On the calculation of vertical motion in eastern boundary currents from determinations of horizontal motion, *J. Geophys. Res., 70*, 2799–2803.

Bakun, A., and C. S. Nelson (1977), Climatology of upwelling related processes off Baja California, *Calif. Coop. Fish. Invest., Rep. XIX*, 107– 127.

Bakun, A., and C. S. Nelson (1991), The seasonal cycle of wind-stress curl in Subtropical Eastern Boundary Current regions, *J. Phys. Oceanogr., 21,* 1815– 1834.

Barth, J. A., and R. L. Smith (1998), Separation of a coastal upwelling jet at Cape Blanco, Oregon, USA, *S. Afr. J. Mar. Sci., 19,* 5– 14.

Barth, J. A., S. D. Pierce, and R. L. Smith (2000), A separating coastal upwelling jet at Cape Blanco, Oregon and its connection to the California Current System, *Deep Sea Res., Part II, 47,* 783– 810.

Barth, J., B. Menge, J. Lubchenco, F. Chan, J. Bane, A. Kirincich, M. McManus, K. Nielsen, S. Pierce, and L. Washburn (2007), Delayed upwelling alters nearshore costal ocean ecosystems in the northern California current, Proc. *Nat. Acad. Sci., 104,* 3719-3724.

Barth, J. A., S. D. Pierce, and T. J. Cowles (2005), Mesoscale structure and its seasonal evolution in the northern California Current System, *Deep Sea Res., Part II, 52,* 5–28.

Batteen, M. L. (1997),Wind-forced modeling studies of currents, meanders, and eddies in the California Current System, *J. Geophys. Res., 102*(C1), 985–1010.

Bowman, M. J. (1978), Oceanic fronts in coastal processes, in Oceanic Fronts in Coastal Processes, edited by M. Bowman and W. Esias, pp. 2– 5, Springer, New York.

Breaker, L. C., E. M. Armstrong, and C. A. Endris (2010), Establishing an objective basis for image compositing in satellite oceanography, *Rem. Sens. Env., 114,* 345-362.

Breaker, L. C., and C. N. K. Mooers (1986), Oceanic variability off the Central California coast, *Prog. Oceanogr., 17,* 61–135.

Brink, K. H., R. C. Beardsley, J. Paduan, R. Limeburner, M. Caruso, and J. G. Sires (2000), A view of the 1993– 1994 California Current based on surface drifters, floats, and remotely sensed data, *J. Geophys. Res., 105*(C4), 8575– 8604.

Canny, J. (1986), A computational approach to edge-detection, *IEEE Trans. Patt. Anal. Mach. Intell., 6*, 679– 698.

Capet, X., J. C. McWilliams, M. J. Molemaker, A. F. Shchepetkin (2008a), Mesoscale to Submesoscale Transition in the California Current System. Part I: Flow Structure, Eddy Flux, and Observational Tests, *J. Phys. Oceanogr., 38,* 29–43.

Capet, X., J. C. McWilliams, M. J. Molemaker, A. F. Shchepetkin (2008b), Mesoscale to Submesoscale Transition in the California Current System. Part II: Frontal Processes, *J. Phys. Oceanogr., 38,* 44–64.

Capet, X., J. C. McWilliams, M. J. Molemaker, A. F. Shchepetkin (2008c), Mesoscale to Submesoscale Transition in the California Current System. Part III: Energy Balance and Flux, *J. Phys. Oceanogr., 38,* 2256–2269.

Castelao, R. (2011), Intrusions of Gulf Stream waters onto the South Atlantic Bight shelf, *J. Geophys. Res., 116,* C10011, doi:10.1029/2011JC007178.

Castelao, R. M. (2012), Sea surface temperature and wind stress curl variability near a cape, *J. Phys. Oceanogr., 42,* 2073-2087.

Castelao, R. M., and J. A. Barth (2005), Coastal ocean response to summer upwelling favorable winds in a region of alongshore bottom topography variations off Oregon, *J. Geophys. Res., 110,* C10S04.

Castelao, R. M., and J. A. Barth (2006), The relative importance of wind strength and alongshelf bathymetric variations on the separation of a coastal upwelling jet, *J. Phys. Oceanogr., 36*, 412-425.

Castelao, R. M., and J. A. Barth (2007), The role of wind stress curl in jet separation at a cape, *J. Phys. Oceanogr., 37,* 2652-2671.

Castelao, R. M., J. A. Barth, and T. P. Mavor (2005), Flow-topography interactions in the northern California Current System observed from geostationary satellite data, *Geophys. Res. Lett., 32,* L24612, doi:10.1029/2005GL024401.

Castelao, R. M., T. P. Mavor, J. A. Barth, and L. C. Breaker (2006), Sea surface temperature fronts in the California Current System from geostationary satellite observations, *J. Geophys. Res., 111,* C09026, doi:10.1029/2006JC003541.

Chaigneau, A., G. Eldin, and B. Dewitte (2009), Eddy activity in the four major upwelling systems from satellite altimetry, *Progr. Oceanogr., 83,* 117-123.

Chelton, D. (1982), Large-scale response of the California current to forcing by the wind stress curl, *CalCOFI Rep., Vol. XXIII,* 130-148.

Chelton, D. B., R. L. Bernstein, A. Bratkovitch, and P. M. Kosro (1987), The central California coastal circulation study, *Eos Trans. AGU, 68,* 12– 13.

Chelton, D. B., and R. Davis (1982), Monthly mean sea-level variability along the west coast of North America, *J. Phys. Oceanogr., 12,* 757-784.

Chelton, D. B., and M. H. Freilich (2005), Scatterometer-based assessment of 10-m wind analyses from the operational ECMWF and NCEP numerical weather prediction models, *Mon. Wea. Rev., 133*, 409–429.

Chelton, D. B., M. G. Schlax, M. H. Freilich, and R. F. Milliff (2004), Satellite measurements reveal persistent small-scale features in ocean winds, *Science, 303,* 978– 983.

Chelton, D., M. G. Schlax, and R. M. Samelson (2011), Global observations of nonlinear mesoscale eddies, *Progr. in Oceanogr., 91*, 167-216.

Chelton, D., and S.-P. Xie (2010), Coupled ocean-atmosphere interactions at oceanic mesoscales, *Oceanography, 23,* 52-69.

Haidvogel, D. B., A. Beckman, and K. Hedstrom (1991), Dynamical simulation of filament formation and evolution in the coastal transition zone, *J. Geophys. Res., 96,* 15,017–15,040.

Hickey, B. M. (1979), The California Current System: Hypotheses and facts, *Prog. Oceanogr., 8,* 191– 279.

Hickey, B. M. (1998), Coastal oceanography of western North America from the tip of Baja California to Vancouver Island, in The Sea, vol. 11, The Global Coastal Ocean Regional Studies and Syntheses, edited by A. R. Robinson and K. H. Brink, pp. 345–393, John Wiley, Hoboken, N. J.

Huyer, A. (1983), Coastal upwelling in the California Current System, *Prog. Oceanogr., 12,* 259– 284.

Huyer, A., J. A. Barth, P. M. Kosro, R. K. Shearman, and R. L. Smith (1998), Upper-ocean water mass characteristics of the California current, Summer 1993, *Deep Sea Res., Part II, 45,* 1411– 1442.

Huyer, A., J. H. Fleischbein, J. Keister, P. M. Kosro, N. Perlin, R. L. Smith, and P. A. Wheeler (2005), Two coastal upwelling domains in the northern California Current System, *J. Mar. Res., 63,* 901–929.

Huyer, A., E. Sobey, and R. Smith (1979), The spring transition in currents over the Oregon continental shelf, *J. Geophys. Res., 84,* 6695-7011.

Kahru, M., E. Di Lorenzo, M. Manzano-Sarabia, and B. Mitchell (2012), Spatial and temporal statistics of sea surface temperature and chlorophyll fronts in the California Current, *J. Plankton Res., 34,* 749-760.

Kelly, K. A. (1983), Swirls and plumes of application of statistical methods of satellite-derived sea surface temperature, *CODE Tech. Rep. 18, Scripps Inst. of Oceanogr., La Jolla, Calif.*

Kelly, K. A., R. C. Beardsley, R. Limeburner, K. H. Brink, J. D. Paduan, and T. K.

Chereskin (1998), Variability of the near-surface eddy kinetic energy in the California Current based on altimetric, drifter, and moored current data, *J. Geophys. Res., 103*(C6), 13,067– 13,083.

Kosro, P. M., and A. Huyer (1986), CTD and velocity surveys of seaward jets off northern California, July 1981 and 1982, *J. Geophys. Res., 91,* 7680– 7690.

Kosro, P. M., et al. (1991), The structure of the transition zone between coastal waters and the open ocean off northern California, winter and spring 1987, *J. Geophys. Res., 96,* 14,707–14,730.

Kostianoy, A. G. and J. R. E. Lutjeharms (1999), Atmospheric effects in the Angola-Benguela frontal zone, *J. Geophys. Res., 104,* 20963-20970.

Kundu, P., J. Allen, and R. Smith (1975), Modal decomposition of the velocity field near the Oregon coast, *J. Phys. Oceanogr., 5*, 683-704.

Large, W. G., J. C. McWilliams, and S. C. Doney (1994), Oceanic vertical mixing: A review and a model with a nonlocal boundary layer parameterization, *Rev. Geophys., 32*, 363–403.

Lentz, S. (2003), A climatology of salty intrusions over the continental shelf from Georges Bank to Cape Hatteras, *J. Geophys. Res., 108* (C10), 3326, doi:10.1029/2003JC001859.

Mavor, T. P., and J. J. Bisagni (2001), Seasonal variability of sea-surface temperature fronts on Georges Bank, *Deep Sea Res., Part II, 48,* 72– 86.

Mesias, J. M., R. P. Matano, and P. T. Strub (2001), A numerical study of the upwelling circulation off central Chile, *J. Geophys. Res., 106,* 19611–19623.

Mesias, J. M., R. P. Matano, and P. T. Strub (2003), Dynamical analysis of the upwelling circulation off central Chile*, J. Geophys. Res., 108,* 3085, doi:10.1029/2001JC001135.

Meunier, T., E. Barton, B. Barreiro, and R. Torres (2012), Upwelling filaments off Cap Blanc: Interaction of the NW African upwelling current and the Cape Verde frontal zone eddy field?, *J. Geophys. Res., 117*, C08031.

Naderi, F. M., M. H. Freilich, and D. G. Long (1991), Spaceborne radar measurement of wind velocity over the ocean: An overview of the NSCAT scatterometer system, *Proc. IEEE, 79,* 850– 866.

Nieto, K., H. Demarcq, and S. McClatchie (2012), Mesoscale frontal structures in the Canary Upwelling System: New front and filament detection algorithms applied to spatial and temporal patters, *Remote Sens. Environ., 123*, 339-346.

O'Neill, L. W., D. B. Chelton, and S. K. Esbensen (2003), Observations of SST-induced perturbations of the wind stress field over the Southern Ocean on seasonal time scales, *J. Climate, 16,* 2340–2354.

O'Neill, L. W., D. B. Chelton, and S. K. Esbensen (2010), The effects of SST-induced horizontal surface wind speed and direction gradients on midlatitude vorticity and divergence*, J. Climate, 18,* 2706-2723.

O'Neill, L. W., D. B. Chelton, S. K. Esbensen, and F. J. Wentz (2005), High-resolution satellite observations of SST modification of the marine atmospheric boundary layer over the Agulhas Return Current, *J. Climate, 18,* 2706–2723.

Pattullo, J., and W. McAlister (1962), Evidence for oceanic frontogenesis off Oregon, *Science, 135,* 106-107.

Penven, P., C. Roy, A. Colin de Verdière, and J. Largier (2000), Simulation of a coastal jet retention process using a barotropic model, *Oceanol. Acta, 23*, 615–634.

Perlin, N., R. Samelson, and D. Chelton (2004), Scatterometer and model wind and wind stress in the Oregon-northern California coastal zone, *Mon. Wea. Rev., 132,* 2110-2129.

Santos, F., M. Gomez-Gesteira, M. deCastro, and I. Alvarez (2012), Differences in coastal and oceanic SST trends due to the strengthening of coastal upwelling along the Benguela current system, *Cont. Shelf Res., 34,* 79-86.

Strub, P. T., and C. James (1995), The large-scale summer circulation of the California current, *Geophys. Res. Lett., 22*, 207– 210.

Strub, P. T., and C. James (2000), Altimeter-derived variability of surface velocities in the California Current System: 2. Seasonal circulation and eddy statistics, *Deep Sea Res., Part II, 47,* 831–870.

Strub, P. T., J. S. Allen, A. Huyer, R. L. Smith, and R. C. Beardsley (1987), Seasonal cycles of currents, temperatures, winds, and sea level over the Northeast Pacific continental shelf: 35 N to 48 N, *J. Geophys. Res., 92,* 1507– 1526.

Strub, P. T., et al. (1991), The nature of the cold filaments in the California Current System, *J. Geophys. Res., 96,* 14,743– 14,768.

Sverdrup, H. U., and W. E. Allen (1939), Distribution of diatoms in relation to the character of water masses and currents off southern California, *J. Mar. Res., 2,* 131–144.

Sverdrup, H. U., M. W. Johnson, and R. H. Fleming (1942), The Oceans, Their Physics, Chemistry and General Biology, 1087 pp., Prentice-Hall, Upper Saddle River, N. J.

Swenson, M. S., P. P. Niller, K. H. Brink, and M. R. Abbott (1992), Drifter observations of a cold filament off Point Arena, California, in July 1988, *J. Geophys. Res., 97*(C3), 3593– 3610.

Ullman, D. S., and P. C. Cornillon (1999), Satellite-derived sea surface temperature fronts on the continental shelf off the northeast U.S. coast, *J. Geophys. Res., 104*(C10), 23,459– 23,478.

Vazquez-Cuervo, J., B. Dewitte, T. Chin, E. Armstrong, S. Purca, and E. Alburqueque (2013), An analysis of SST gradients off the Peruvian Coast: The impact of going to higher resolution, *Remote Sens. Environ., 131*, 76-84.

Walsh, J. J. (1977), A biological sketchbook for an eastern boundary current, in The Sea, vol. 6, edited by E. D. Goldbert, I. N. McCave, J. J. O'Brien, and J. H. Steele, pp. 923 – 968, Wiley-Interscience, Hoboken, N. J.

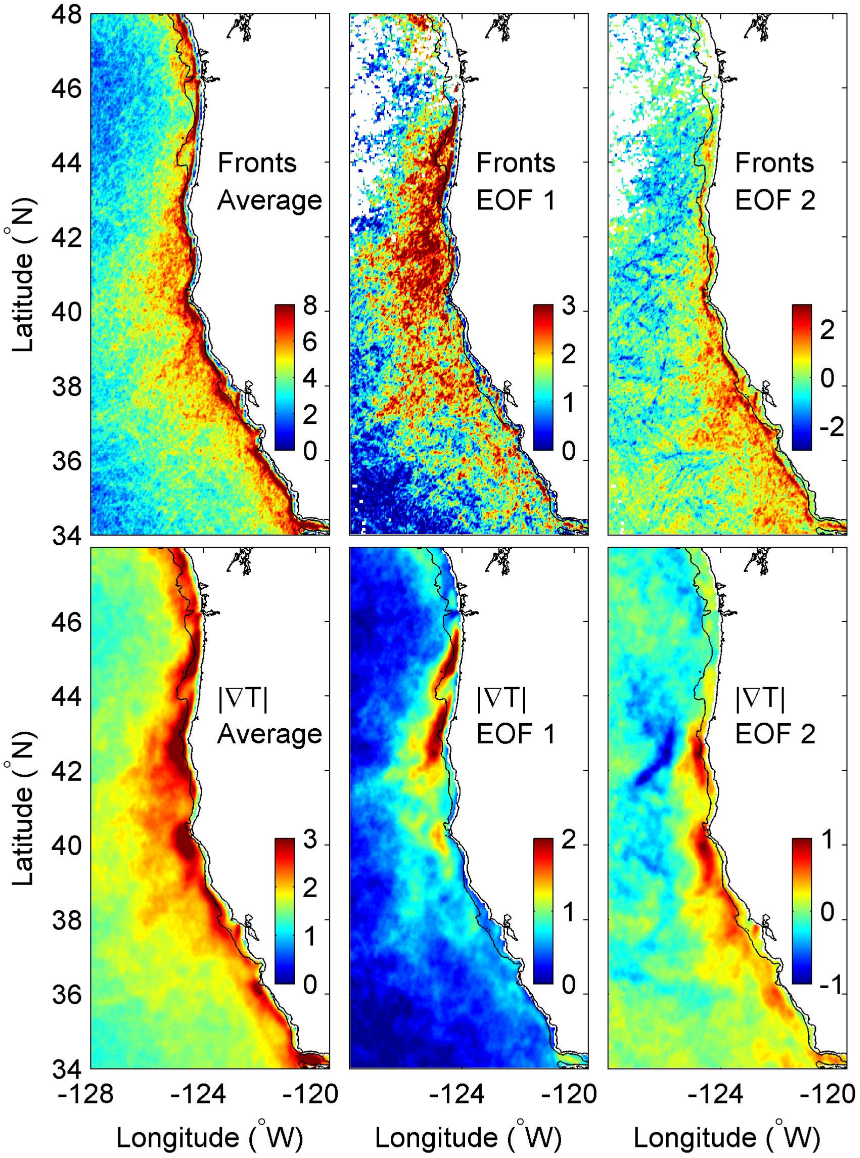

Figure A.1 – Average and first 2 EOFs of (top) SST frontal probabilities (%) and (bottom) SST gradient magnitudes (°C per 100 km). Only pixels where observations are available for at least 20% of the time in every single month are used in the frontal probability EOF decomposition. The 200 m isobath is shown in black. Names of capes and submarine banks are shown in Figure A.4.

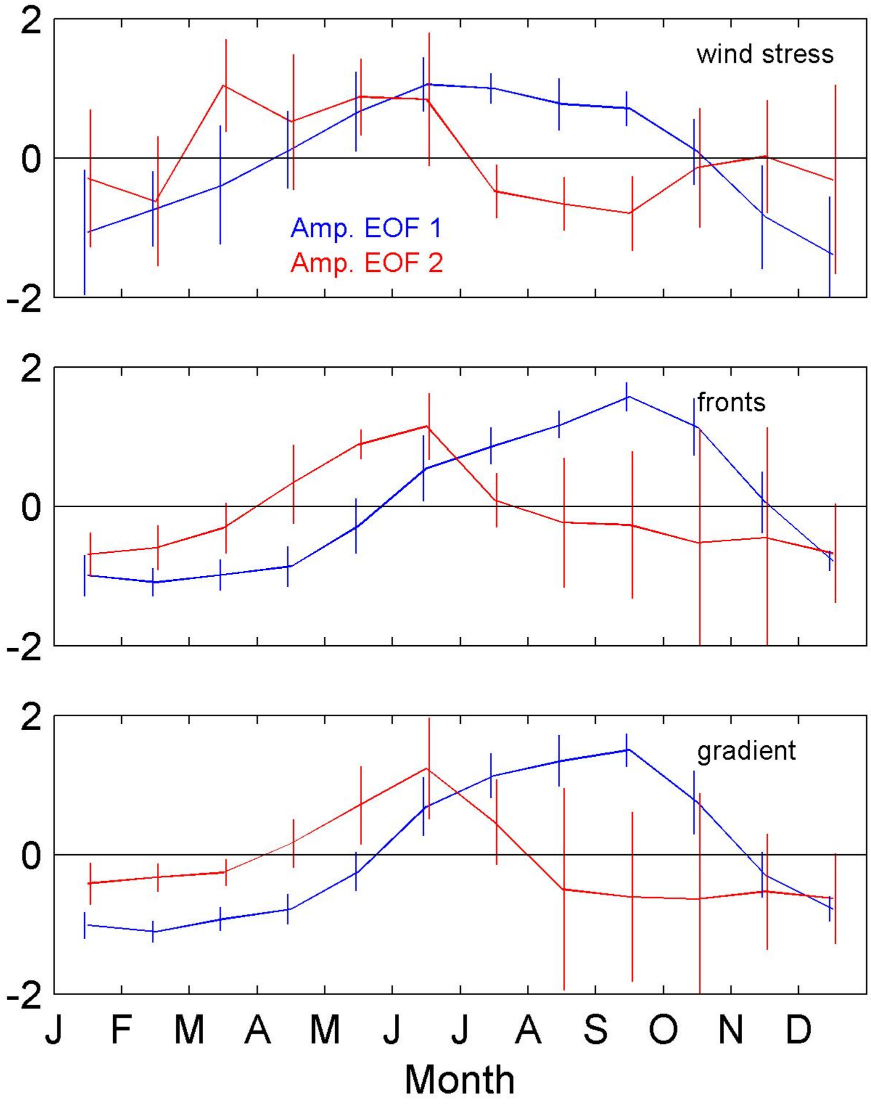

Figure A.2 – Monthly averages ± 1 standard deviation of amplitude time series for EOF 1 (blue) and EOF 2 (red) of (top) coastal alongshore wind stress, (middle) frontal probabilities, and (bottom) SST gradient magnitudes.

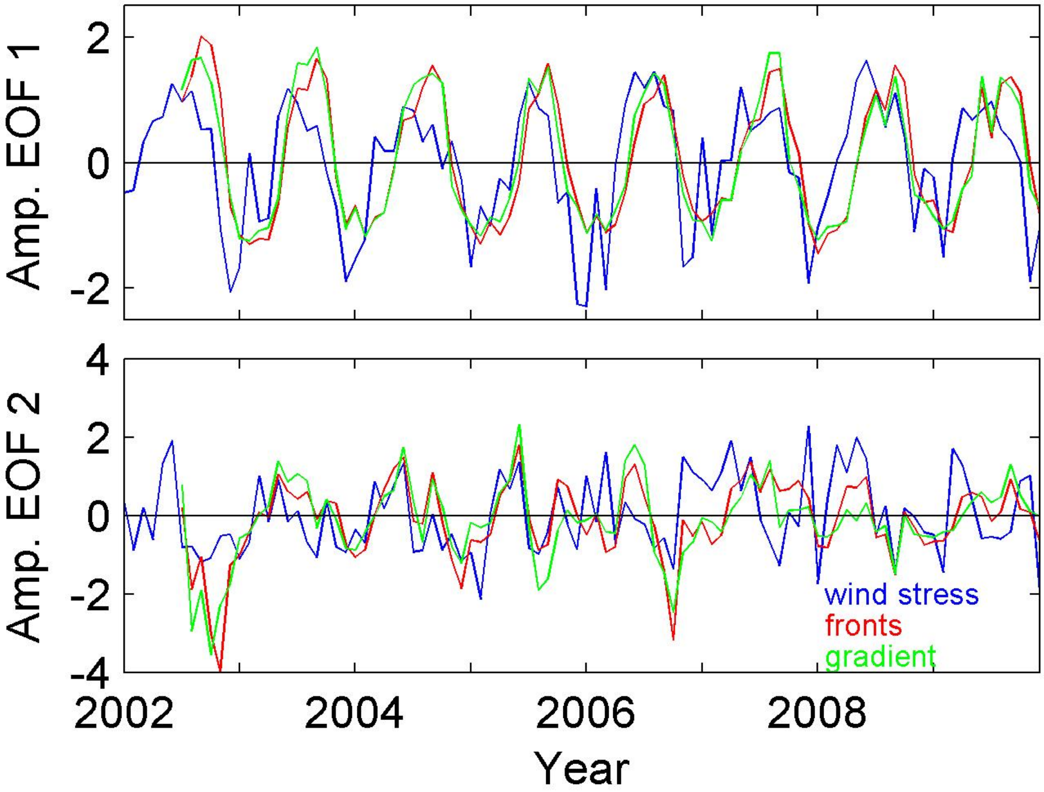

Figure A.3 – Amplitude time series for (top) EOF 1 and (bottom) EOF 2 of coastal alongshore wind stress (blue), frontal probabilities (red), and SST gradient magnitudes (green).

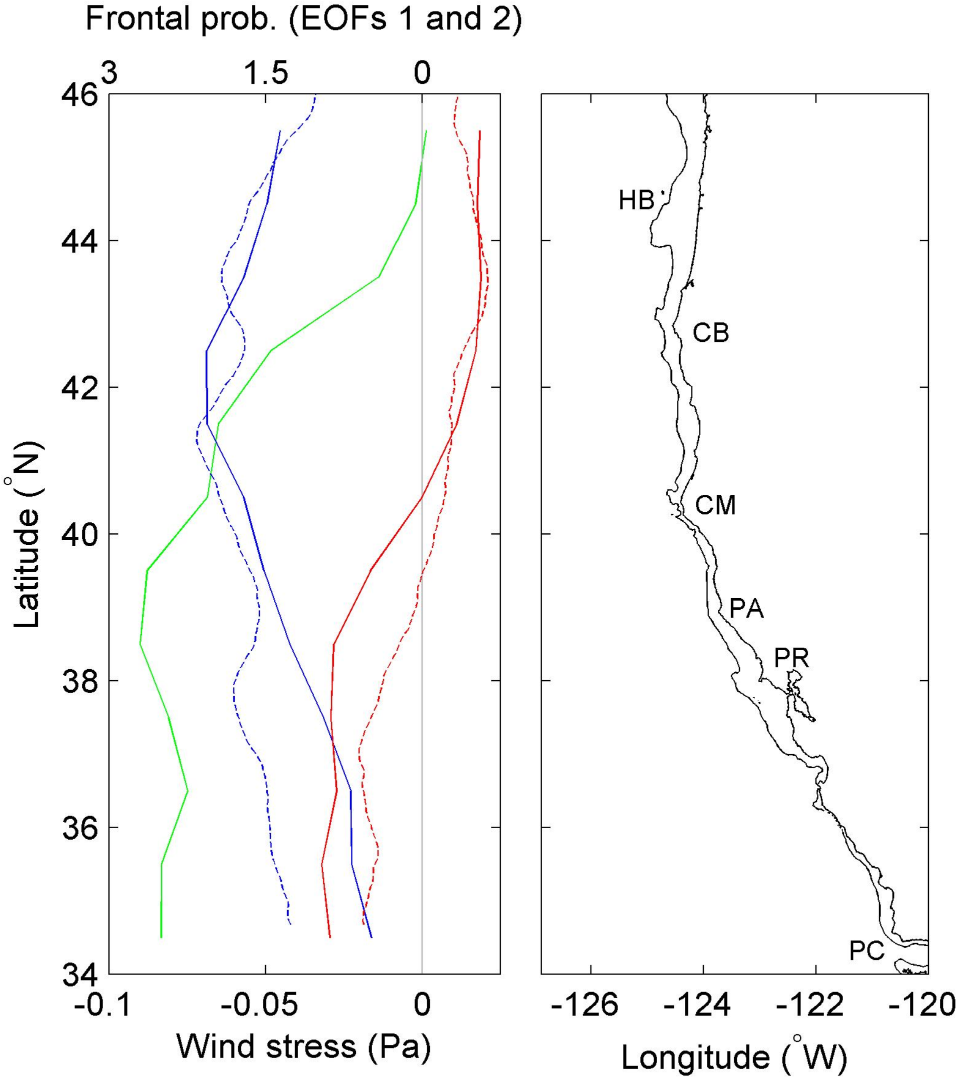

Figure A.4 – Average (green) and first (solid blue) and second (solid red) EOFs of (left) coastal alongshore wind stress as a function of latitude in the California Current System. Dashed lines are cross-shelf averages of the first (blue) and second (red) EOFs of SST frontal probabilities (from Figure A.1) within 400 km from the coast. Coastline and 200 m isobath are shown on the right panel. HB: Heceta Bank; CB: Cape Blanco; CM: Cape Mendocino; PA: Point Arena; PR: Point Reyes; PC: Point Conception.

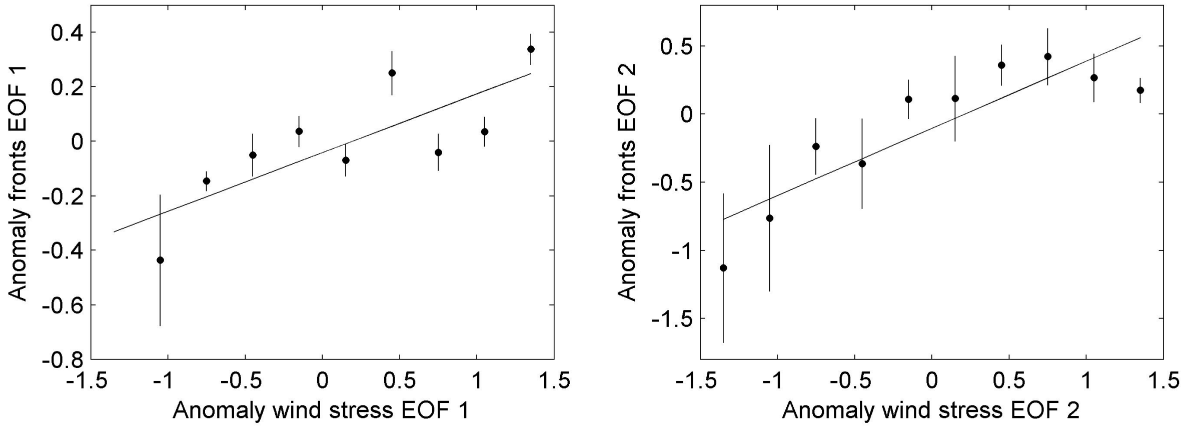

Figure A.5 – Binned scatterplots of anomalies in the amplitude time series of the (left) first and (right) second EOFs of coastal alongshore wind stress and frontal probabilities. Anomalies are defined as the deviations of the amplitude time series (seen in Figure A.3) from their respective monthly averages (seen in Figure A.2). The points in each panel are the means within each bin, while error bars represent the ± 1 standard error of the mean within each bin. Black lines are linear fit to observations.

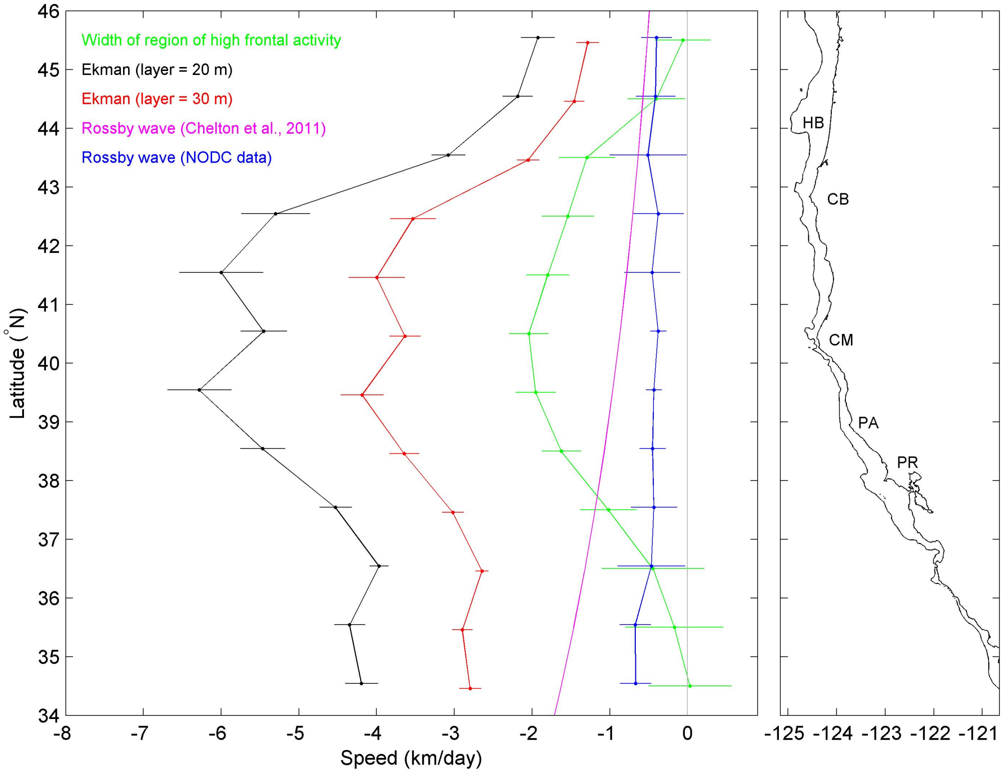

Figure A.6 – Average speed of the widening of the region of high frontal activity from June to September as a function of latitude (green). The average speeds associated with surface Ekman transport during the same period distributed uniformly in a surface layer 20 m (black) or 30 m (red) thick are also shown. Magenta and blue curves are phase speeds of long baroclinic Rossby waves based on Chelton et al. (2011) and computed using historic temperature and salinity observations from the NODC archives that were collected around the 2000 m isobath, respectively. Error bars are ± 1 standard error of the mean. Coastline and 200 m isobath are shown on the right panel. HB: Heceta Bank; CB: Cape Blanco; CM: Cape Mendocino; PA: Point Arena; PR: Point Reyes.

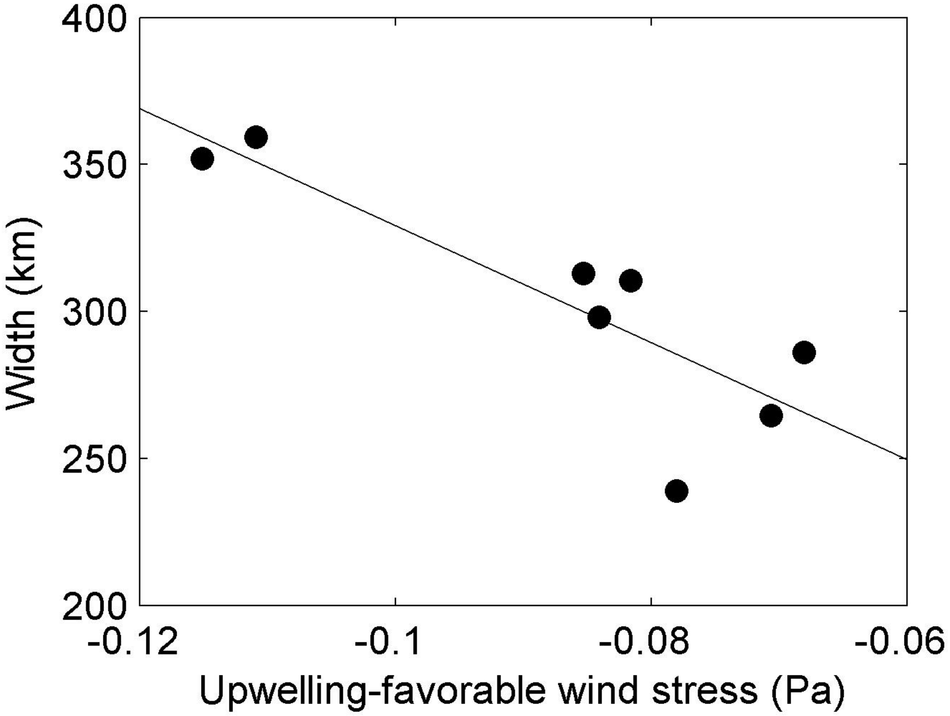

Figure A.7 – Average wind stress during the upwelling season (May to September) for different years (2002 to 2009) versus the maximum width of the region of high frontal activity at the end of the upwelling season (September) between Cape Blanco and Cape Mendocino. Black line is linear fit to observations.

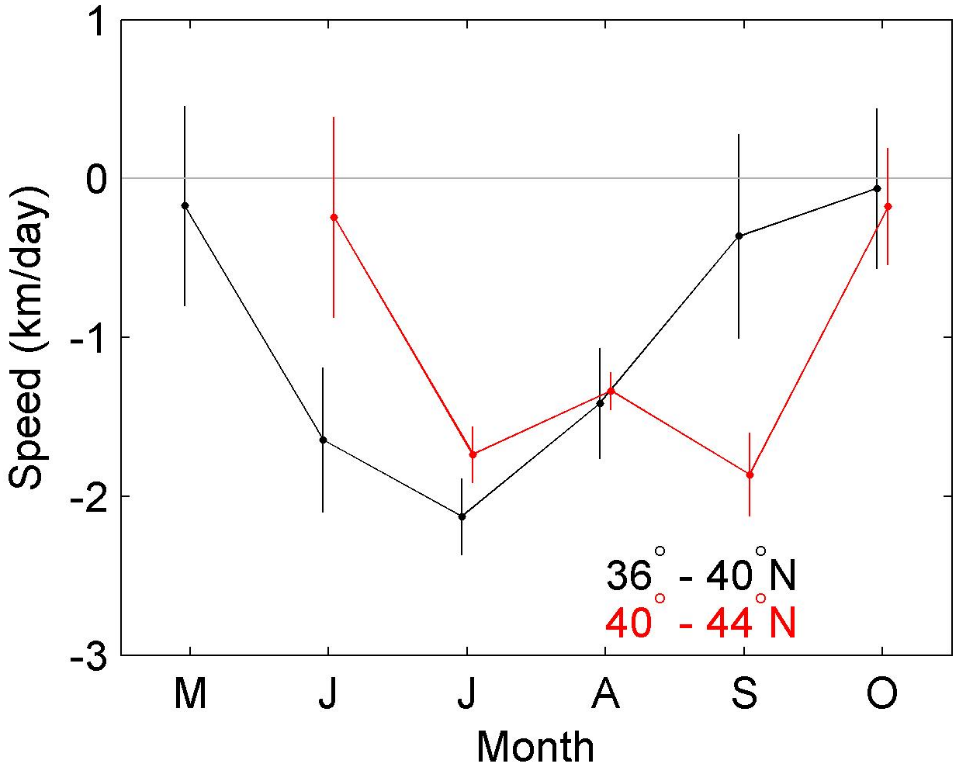

Figure A.8 – Time series of the average speed of the widening of the region of high frontal activity for the region to the south (black) and to the north (red) of Cape Mendocino. Error bars are ± 1 standard error of the mean for each month. Speed on July 1st, for example, is computed using frontal probabilities from June and July.

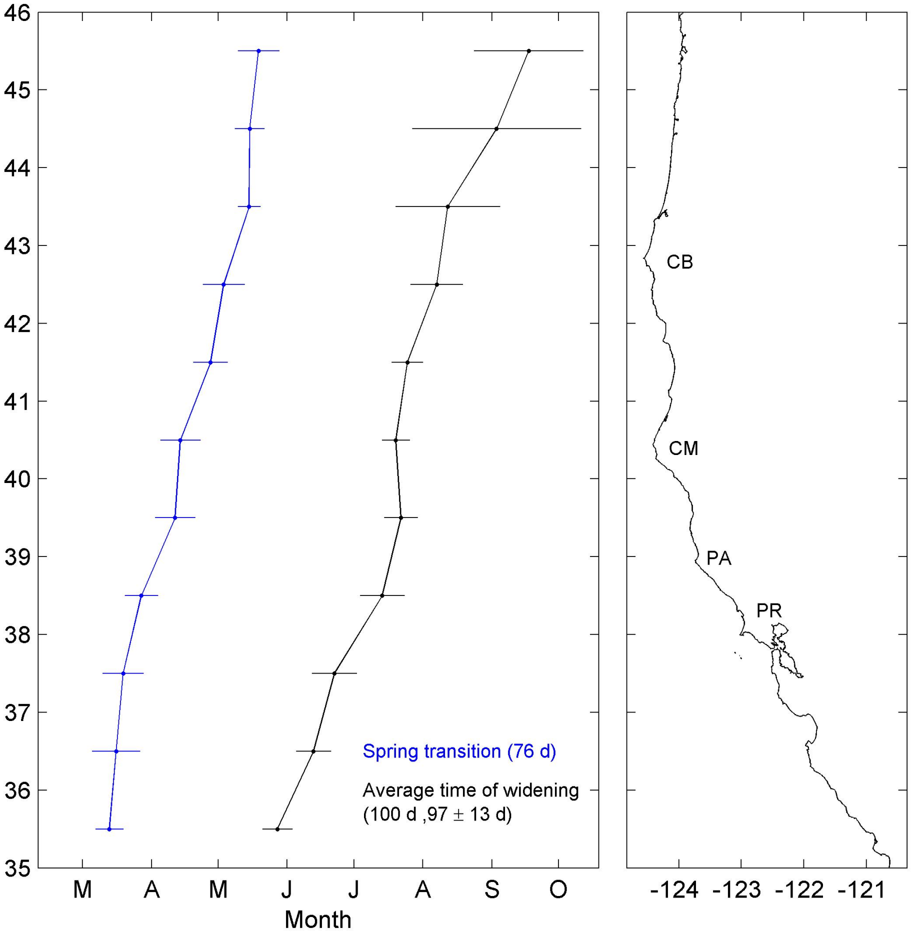

Figure A.9 – Average time of the widening of the region of high frontal activity (see Eq. (1) for definition) in the CCS as a function of latitude (black). The timing of the spring transition is shown in blue. Error bars are ± 1 standard error of the mean. The first number in parentheses shows the difference for each curve between the northernmost and the southernmost values in days. The second and third number in parentheses show the average ± 1 standard deviation of the difference between the average time of the widening of the region of high frontal activity and the timing of the spring transition in days (i.e., difference between black and blue curves). Coastline is shown on the right panel. CB: Cape Blanco; CM: Cape Mendocino; PA: Point Arena; PR: Point Reyes.

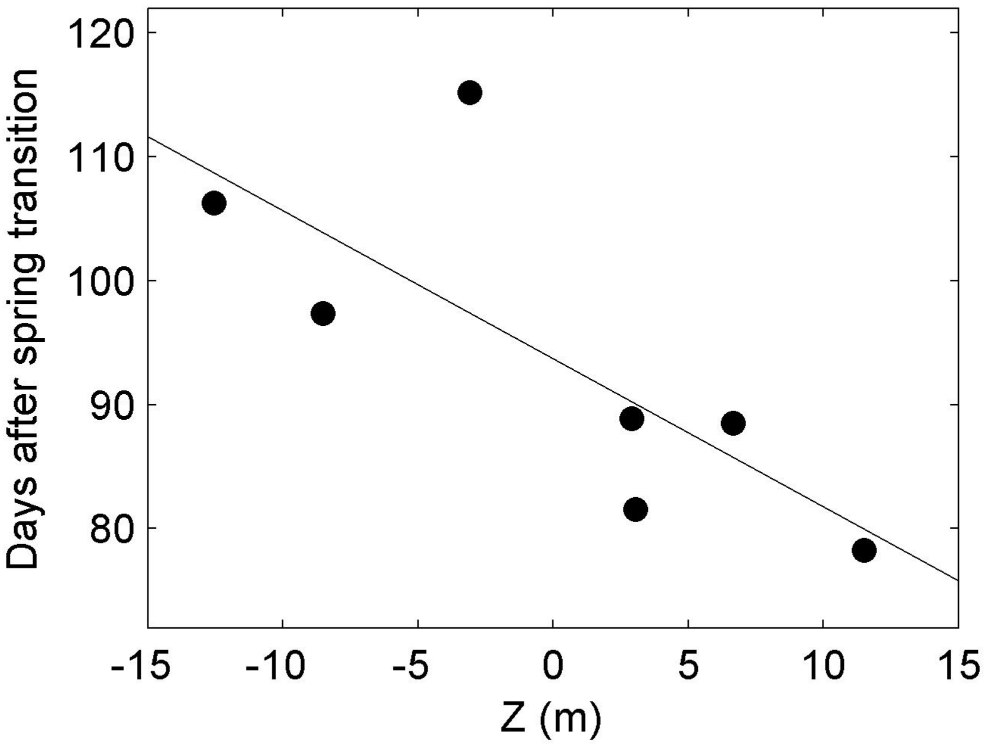

Figure A.10 – Timing of the widening of the region of high frontal activity south of Cape Blanco (in days after spring transition) as a function of vertical displacement Z (m) driven by time integral of wind stress curl anomaly (see Eq. (2) for definition). Black line is linear fit to observations.

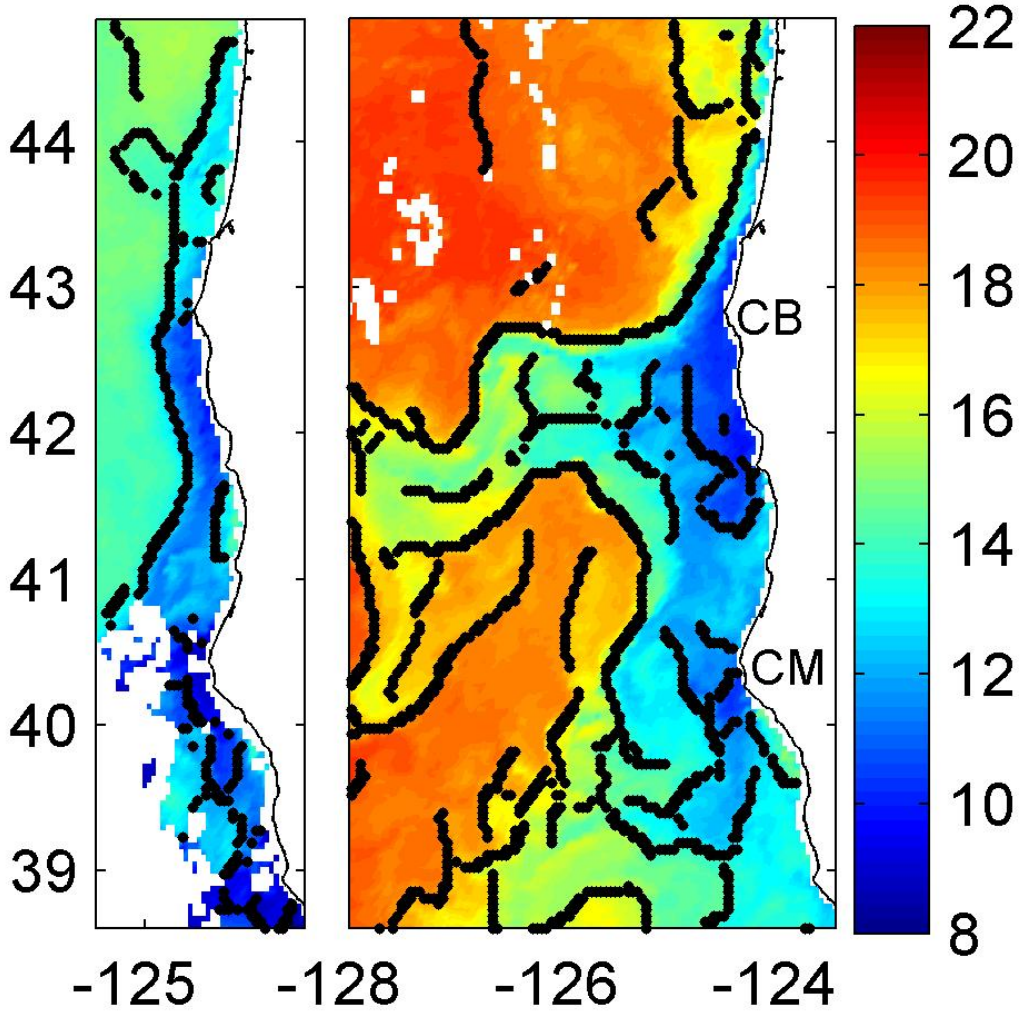

Figure A.11 – SST (°C) on (left) 24 May 2004 and (right) 5 September 2004. Black dots mark the location of fronts found by the edge-detection algorithm. Clouds and land are shown in white. CB: Cape Blanco; CM: Cape Mendocino.